Modeling and Stability Analysis of Power Systems with Discontinuous Right Hand Side Differential, Algebraic Equations

Mohammed Ahsan Adib Murad

16203295

A thesis submitted to University College Dublin
in fulfillment of the degree of

Doctor of Philosophy

College of Engineering and Architecture
School of Electrical and Electronic Engineering

Supervisor: Prof. Federico Milano
Head of School: Prof. Peter Kennedy

September 2020

I hereby certify that the submitted work is my own work, was completed while registered as a candidate for the degree stated on the Title Page, and I have not obtained a degree elsewhere on the basis of the research presented in this submitted work.

Acknowledgments

I am grateful to my brilliant supervisor Prof. Federico Milano for giving me this opportunity. He has been a great support during the past four years. My special gratitude and thanks to him for his valuable suggestions, motivation and training to solve challenging engineering problems.

I thank all of my colleagues at UCD for their kind support and help. Special thank to L. Vanfretti, I. Dassios, Á. Ortega, B. Hayes, G. M. Jónsdóttir, M. Liu, F. M. Mele, G. Tzounas, T. Kërçi, F. Bruzzone, W. Zhong, M. Adeen, J. Chen and M. Moschella for their critical comments, suggestions related to various aspects of this work and of course for their cooperation. My sincere thank to R. Thomas, J. Rueß and M. Zhao from DIgSILENT GmbH for all of their support during my internship at DIgSILENT.

I would like to thank my beloved parents and family for their never-ending support and encouragement throughout my entire life, without which I could not reach this far. Specially my father, whose inspiration has been my guide and I dedicate this thesis to him. I thank my beloved wife, Dr. Jakia Najnin, for all of her sacrifices throughout this work.

Finally, I thank Science Foundation Ireland for making this research possible by funding me under project Advanced Modelling for Power System Analysis and Simulation (AMPSAS), Grant No. SFI/15/IA/3074.

Contents

List of Figures

List of Tables

List of Abbreviations and Acronyms

AVR	Automatic Voltage Regulator
AW	Anti-Windup
DSAR	Differential Switched Algebraic and State-Reset
DAE	Differential and Algebraic Equation
DASSL	Differential Algebraic System Solver
DFIG	Doubly Fed Induction Generators
DRHS	Discontinuous Right Hand Side
FRT	Fault Ride Through
FOPID	Fractional Order Proportional, Integral and Differential
HDAE	Hybrid Differential and Algebraic Equation
HVDC	High-Voltage Direct Current
OEL	Over-Excitation Limiter
PID	Proportional, Integral and Differential
PSS	Power System Stabilizer
SMIB	Single-Machine Infinite-Bus
STATCOM	Static Synchronous Compensator
TG	Turbine Governor
ULTC	Under-Load Tap Changer
VSC	Voltage-Sourced Converter
WSCC	Western System Coordinating Council

Abstract

Power systems are one of the most complex dynamic systems due to their multi-time scale and non-linear nature. This work focuses in particular on the electromechanical dynamics of power systems which are hybrid (discrete-continuous) and are therefore studied using a set of Hybrid Differential-Algebraic Equations (HDAEs) or Discontinuous Right-Hand Side DAEs (DRHS DAEs). Traditional HDAEs possess several challenges during modeling, implementation, and numerical simulation stages, depending on the nature of the discontinuities arising from different applications.

This thesis studies the impact of discontinuities on power system physical stability as well as on the numerical stability of a solver considering two specific discontinuous models. The first model is an under load tap changing transformer, which introduces a discrete variable in the DRHS DAEs due to the physical operation of the transformer. The second model is a proportional-integral controller used in different components of power systems, e.g. voltage source converter and automatic voltage regulators which introduces a discontinuity in the state and algebraic variables of DRHS DAEs. In particular, a thorough discussion of the deadlock and chattering issues during time-domain simulation arise from the latter model is provided. This discussion is based on two time domain simulation techniques widely used in power system tools, namely, time-stepping and event-driven method. To solve the deadlock and chattering issues in both of these simulation techniques, a theoretical approach given by Filippov is proposed.

Case studies with small to large sizes, e.g., single machine infinite bus, WSCC 9-bus, IEEE 14-bus, 74-bus Nordic system and all-island Irish system with 1479-buses connected to a simplified 63-bus Great Britain system through a high-voltage direct

current link are considered and tested in the thesis. Simulation results indicate the importance of accurate modeling and implementation of discontinuous models for dynamic analysis.

1 Introduction

Reliable electric energy supply, i.e. electric power systems are the main drive force of modern society. Therefore the secure and stable operation of power systems is of utmost importance. However, the security assessment of power systems is not a trivial task due to their complexity, non-linearity and multi-time scales, as illustrated in Figure 1.1 [56]. This thesis focuses on dynamics ranging from milliseconds to minutes range, typically known as electro-mechanical dynamics.

Electro-mechanical dynamic processes are studied through a dynamic phasor model consisting of nonlinear Differential Algebraic Equations (DAEs) [69, 76], as follows,

$$\dot{\boldsymbol{x}} = \boldsymbol{f}(\boldsymbol{x}, \boldsymbol{y}) \ , \tag{1.1}$$

$$\boldsymbol{0} = \boldsymbol{g}(\boldsymbol{x}, \boldsymbol{y}) \ , \tag{1.2}$$

where $\boldsymbol{f}$ and $\boldsymbol{g}$ are the differential and algebraic equations respectively; $\boldsymbol{x}$ and $\boldsymbol{y}$ are the vector of state and algebraic variables respectively. This set of DAEs possesses a continuous (or smooth) manifold near the operating point or system equilibrium. However, the large disturbance analysis of power systems is characterized by complex interactions between continuous dynamics and discrete events due to transformer tap position, controller saturation, generator over-excitation limit, etc. These kinds of discontinuities can significantly influence the system behavior [57]. Therefore, power system models should properly take into account all the non-linearities related to

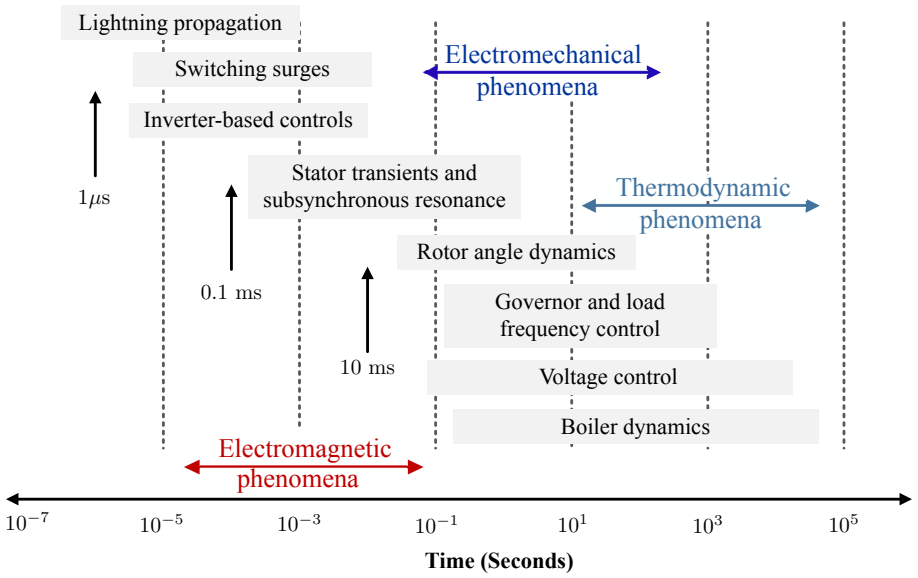

Figure 1.1: Illustration of power system time scales.

the discontinuous behavior, and analysis tools should provide accurate predictions of the system behavior under severe conditions. When these discontinuities are included in a set of continuous DAEs, the resulting model is called a set of Hybrid Differential-Algebraic Equations (HDAEs) [76]. As the "Hybrid" term is often referred to as mixed analog and digital modeling, in this work, to avoid confusion the DAE formulation is called as Discontinuous Right-Hand Side DAEs (DRHS DAEs). Power system tools use different approaches to describe such discontinuities of the models in time domain simulation to capture complete dynamic behavior, and the development of a systematic model using DAEs has received little attention [63]. A comprehensive literature review on this topic is given in Chapter 2. The objective of this work is to model the power system as a set of DRHS DAEs using a systematic approach suitable for computer language implementation.

An important aspect of discontinuities is that, depending on their nature, they significantly impact the power system's physical stability and numerical stability.

For instance, the tap changing mechanism of a regulating transformer introduces a discrete variable on the DAEs given by (1.1-1.2) [58]. Whereas controller saturation, e.g., lag, lead-lag, and Proportional-Integral (PI) controllers, introduce discrete quantities in state and algebraic variables [8]. The discrete variables related to tap changers severely impact the slow or long-term voltage stability [43, 64, 112], which is related to physical stability. And the discrete variables coupled into the algebraic and the state variables impact both physical and numerical stability. For example, limits on a integer-order PI controller or a fractional-order PI controller can cause a numerical instability in different applications, namely, voltage sourced converters [59, 60] and automatic voltage regulators [48]. References [48, 59, 60] propose heuristic methods to ensure numerical stability during simulation of these models. However, heuristic techniques introduce artificial oscillations in the solution and severely impact numerical solver performance [48]. The second objective of this work is to thoroughly study the non-smooth behavior of power system components that includes discrete variables in their models. Finally, to address numerical instability, this work proposes a theoretical approach given by Filippov [49].

1.1 Thesis Overview and Contributions

This thesis first studies the mathematical model of power systems represented by DRHS DAEs. Then it discusses the impact of two discontinuous models (tap changer transformer and PI limiters) on dynamic response and numerical simulation. To this aim, the following research topics are addressed.

i. *Modeling:* Available mathematical representations of power systems modeled as DRHS DAEs are reviewed and relevant examples are presented. A compre-

hensive discussion of the modeling framework used in this work is given using an illustrative example.

ii. *Under Load Tap Changers:* The working principle of tap changer transformer or Under Load Tap Changers (ULTCs) are discussed. The mathematical models of possible ULTC control techniques are presented. The impact of these ULTC control methods on long-term voltage stability is studied. Finally, impact of the stochastic variations from renewable energy integration on the transformer operation is discussed.

iii. *PI Control Limiters:* Limiting methods on PI controllers commonly adopted in Voltage-Sourced Converter (VSC) based applications are presented. The numerical issues that arise due to implementation based on the IEEE Standard 421.5-2016 are studied. To alleviate these issues, a solution based on the mathematical theory developed by Filippov is proposed. The proposed design is validated and compared with available heuristic solutions, considering both constant and variable limits. Finally, limiters of fractional-order PI controllers are discussed.

The remainder of the thesis is organized as follows.

Chapter 2 provides an overview of the hybrid modeling of power systems. Among several methods, this work considers hybrid modeling based on Hybrid Automata (HA). Section 2.1 provides a literature review on hybrid modeling. In Section 2.2, a brief description of HA and a modeling structure based on HA with an illustrative example is given. Next, the modeling approach and event handling of the simulation tool DOME, which is mainly used in this thesis, is described with an illustrative example in Section 2.3. Finally, Section 2.4 draws conclusions on the matter discussed

in Chapter 2.

Chapter 3 considers under load tap changing transformers as an example of a model where the physical operation is discrete. This chapter aims to show how this kind of discrete behavior impacts the physical stability of power systems. Section 3.1 outlines the motivation of Chapter 3. Section 3.2 briefly introduces tap changer transformers and Section 3.3 presents the discrete and continuous models of ULTCs and their controllers for dynamic studies. Section 3.5 discusses the dynamic response of these devices considering deterministic scenarios. These deterministic case studies show that ULTCs can both improve the transient behavior of the system, and in occasions, cause instability. Section 3.6 includes load and wind speed models formulated as stochastic differential equations that properly capture the probability distribution and auto-correlation of the stochastic processes. Section 3.7 presents a stochastic case study. This considers a small Irish distribution network and shows how the stochastic variations impact the occurrence of tap position change. Section 3.8 draws conclusions.

PI control limiters are considered in Chapter 4. Section 4.1 presents a literature review on the applications of PI controllers. Section 4.2 introduces different limiting methods of PI controllers and Section 4.3 discusses the implementation and numerical issues associated with PI controllers with anti-windup limiters. Using an illustrative example Section 4.3 explains how one of the anti-windup, namely, IEEE Std. 421.5-2016 model method introduce a deadlock of a numerical solver. Section 4.4 presents the model of the VSC, its controllers along with tuning method and shows how the limiting methods are applied to the controllers of the VSC-based devices. Section 4.5 to Section 4.7 illustrate the dynamic behavior of the PI limiters of VSCs through the WSCC 9-bus network and two real-world case studies: (i) a

1,479-bus dynamic model of the all-island Irish system connected to a simplified 63-bus dynamic model of the Great Britain system through an High-Voltage Direct Current (HVDC) link that represents the East-West Interconnector (EWIC); and (ii) a 74-bus dynamic model of the Nordic system with the inclusion of a Static Synchronous Compensator (STATCOM) device. A discussion on simulation results and conclusions are given in Section 4.8 and Section 4.9, respectively.

Chapter 5 revisits the deadlock phenomenon that was briefly introduced in Chapter 4 and proposes a mathematical theory given by Filippov to prevent such deadlock. To this aim, Section 5.1 presents a literature review on application of Filippov Theory (FT). Section 5.2 studies the deadlock of numerical integration techniques related to the IEEE Std. AW model. Section 5.3 briefly discusses FT and Section 5.4 shows how this theory effectively removes the deadlock by smoothing the trajectories. Two examples are discussed: an illustrative example and a simple single-machine power system network. In order to implement an input-output based IEEE Std. 421.5-2016 PI controller, Section 5.5 presents a generalized FT based hybrid model for software implementation of Filippov system models. Numerical validations of the generalized design are presented in Section 5.6 and Section 5.7 using two applications, namely, a relay feedback model and the IEEE Std. 421.5-2016 AW PI model, respectively using the Modelica language as well as the power system software tool DOME. Section 5.8 draws relevant conclusions.

The FT based IEEE Std. PI model is extended to consider variable limits for the VSC-based applications in Chapter 6. In Section 6.1 a literature review on the current limiter of VSCs is given. Section 6.2 discusses the current limiter and fault ride-through functionalities of VSCs. Section 6.3 discusses the FT based IEEE Std. 421.5-2016 PI model to impose variable limits. Section 6.3 also validates this

model through an illustrative example. The impact of variable limits of VSCs along with the PI controller implementations on power system dynamics is presented in Section 6.4 through two case studies: (i) a VSC-HVDC link in the WSCC 9-bus network; (ii) the Nordic system with a VSC-based STATCOM. Section 6.5 provides conclusions relevant to this Chapter.

Fractional Order PI (FOPI) controllers are proposed in different power system applications because of their robust performance for a wide range of operating conditions. Chapter 7 considers limiters on FOPI controllers. Section 7.1 presents a literature review on the fractional calculus and its application. The models of windup and AW limiters of FOPI controllers is given in Section 7.3 following a background on the theory of fractional calculus for control applications given in Section 7.2. Section 7.3 also provides an in depth explanation of a numerical convergence issue during the time domain simulation with inclusion of the FOPI configuration of conditional integrator AW method. A comparison of the impact of FOPI limiter models on the AC voltage regulation of power systems is given in Section 7.4 through VSC-based STATCOM. Conclusions are drawn in Section 7.5.

Finally, Chapter 8 draws relevant conclusions of the overall thesis and suggests future work directions.

1.2 Publications

- **Papers related to the thesis:**
  - **Journal Papers:**
    1. **M. A. A. Murad**, M. Liu and F. Milano, "Modeling and Simulation of

variable limits on conditional anti-windup PI-Controller for VSC-Based Devices," submitted in IEEE Transactions on Circuits and Systems I.

2. **M. A. A. Murad**, F. Milano, "Chattering-Free Modelling and Simulation of Power Systems with Inclusion of Filippov Theory," *Electric Power Systems Research,* Volume 189, 106727, 2020.
3. **M. A. A. Murad** and F. Milano, "Modeling and Simulation of PI-Controllers Limiters for the Dynamic Analysis of VSC-Based Devices," *in IEEE Transactions on Power Systems,* vol. 34, no. 5, pp. 3921-3930, Sept. 2019.

– **Conference Papers:**

4. **M. A. A. Murad**, L. Vanfretti and F. Milano, "Modeling and Simulation of Filippov System Models with Sliding Motions using Modelica," *2020 American Modelica Conference*, On-line event, 22-24 September 2020.
5. **M. A. A. Murad**, G. Tzounas, F. Milano, "Modeling and Simulation of Fractional Order PI Control Limiters for Power Systems", *21st IFAC World Congress (IFAC 2020)*, Berlin, Germany, on-line event, 12-17 July 2020.
6. **M. A. A. Murad**, B. Hayes and F. Milano, "Application of Filippov Theory to the IEEE Standard 421.5-2016 Anti-windup PI Controller," *2019 IEEE Milan PowerTech,* Milan, Italy, 2019, pp. 1-6.
7. **M. A. A. Murad**, F. M. Mele and F. Milano, "On the Impact of Stochastic Loads and Wind Generation on Under Load Tap Changers," *2018 IEEE Power & Energy Society General Meeting (PESGM),* Portland, OR, 2018.
8. **M. A. A. Murad**, Á. Ortega and F. Milano, "Impact on Power System Dynamics of PI Control Limiters of VSC-Based Devices," *2018 Power*

Systems Computation Conference (PSCC), Dublin, 2018, pp. 1-7.

– **Book Chapter:**

9. **M. A. A. Murad**, M. Chiandone, G. Sulligoi, F. Milano, "Long term Voltage Control, in Converter-Based Dynamics and Control of Modern Power Systems," editors: A. Monti, F. Milano, E. Bompard and X. Guillaud, Academic Press, November 2020.

2 Hybrid Modeling of Power System

2.1 Introduction

Systems that describe evolution of states over time are known as dynamical systems. If the states show mixed continuous and discrete behavior, then these systems are often called "hybrid dynamical systems" [114] or simply "hybrid systems". The terminology "hybrid systems" was used in this context for the first time by Witsenhausen in 1966 [118]. Few examples of such systems are: automated highway systems, computer-controlled systems, gear shift control. Specific mathematical models have to be developed to capture and study this hybrid behavior. These models have two main parts: one with differential or difference equations for the continuous states and another with discrete description or automata to model discrete changes. The mathematical models proposed to deal with the hybrid systems that arise in engineering as well as in other disciplines, e.g. economics and sociology, show a variety of structures. An overview of possible modeling methods is discussed in [71]. The techniques mentioned here are, hybrid automata [72, 73], timed automata or hybrid Petri Nets [37,80,92], differential automata [106], discrete event systems [32,122]. Note that these methods are used to describe a hybrid model of a particular application.

Power systems fall into the category of hybrid dynamical systems. Therefore, different modeling structures mentioned above are applied to power systems. How-

ever until now, methods to develop power system models based on hybrid nature or DRHS DAEs have not been fully investigated. In [61] and [63] a hybrid system representation of the power system by Hiskens is proposed based on Hybrid Automata (HA) [26]. This method allows solving power system inverse problems [58], trajectory sensitivity analysis [62] and time domain simulation [63]. Using Hiskens's formulation, a simulation framework is built in [39]. HA is also used in [46,101,102] for power system stability analysis, in [103] for the analysis of cascading failure, in [104] for control of a micro-grid. Another framework based on Hybrid Input/Output Automata (HIOA) is proposed in [50] to analyze power systems with relay control. Hybrid modeling of power systems using Petri Nets is described in [90] and Discrete EVent System (DEVS) is proposed in [109]. Among these different hybrid modeling frameworks, HA is one of the best approaches to capture discontinuous dynamics because it is based on the theory of numerical approximations [107]. That is why in this work HA formulation is adopted.

In this chapter, a brief description of HA and a modeling structure based on HA with an illustrative example is given in Section 2.2. Next, the modeling approach and event handling of the simulation tool DOME, which is used in this thesis, is described with an illustrative example in Section 2.3. Finally, Section 2.4 draws conclusions on the matter discussed in this chapter.

2.2 Hybrid Automata

The modeling formalism of HA is an extension of finite-state machines where each discrete state is associated with a continuous state model. This method is conveniently applied to a vast range of engineering applications. It is a transition

system with inclusion of continuous dynamics and consists of locations, transitions, invariants, guards, n-dimensional continuous functions, jump functions, and synchronization labels [68].

- **Definition (Hybrid Automaton) [72]:** A hybrid automation $\boldsymbol{H}$ is a collection $\boldsymbol{H} = (\boldsymbol{Q}, \boldsymbol{X}, \boldsymbol{f}, \textbf{Init}, \textbf{Dom}, \boldsymbol{E}, \boldsymbol{G}, \boldsymbol{R})$, where
  - $\boldsymbol{Q} = \{q1, q2, \cdots\}$ is a set of discrete states;
  - $\boldsymbol{X} = \mathbb{R}^n$ is a set of continuous states;
  - $\boldsymbol{f}(\cdot, \cdot) : \boldsymbol{Q} \times \boldsymbol{X} \to \mathbb{R}^n$ is a collection vector fields that describe the continuous dynamics, each set of vector fields is assumed to be Lipschitz continuous on the location domain for Q in order to ensure that the solution exists and is unique;
  - $\textbf{Init} \subseteq \boldsymbol{Q} \times \boldsymbol{X}$ is a set of initial states;
  - $\textbf{Dom}(\cdot) : \boldsymbol{Q} \to 2^{\boldsymbol{X}}$ is a domain, describe conditions that continuous state has to satisfy in given mode;
  - $\boldsymbol{E} \subseteq \boldsymbol{Q} \times \boldsymbol{Q}$ is a set of edges;
  - $\boldsymbol{G}(\cdot) : \boldsymbol{E} \to 2^{\boldsymbol{X}}$ is a guard condition that specifies subset of state space where certain transition is enabled;
  - $\boldsymbol{R}(\cdot, \cdot) : \boldsymbol{E} \times \boldsymbol{X} \to 2^{\boldsymbol{X}}$ is a reset map that specifies how new continuous states are related to previous continuous states.

Any physical system described by HA can also be represented through graphs with the definition given above. Interested readers are referred to the reference [72] for further description of those schematics.

2.2.1 Hiskens's Model

In [61] and [63], power systems are formulated as a set of *Differential Switched Algebraic* and *State-Reset* (DSAR) equations, based on hybrid automata. This general representation captures all the characteristics of power system dynamics. The DSAR model is as follows:

$$\dot{\boldsymbol{x}} = \boldsymbol{f}(\boldsymbol{x}, \boldsymbol{y}, \boldsymbol{z}) \ , \tag{2.1}$$

$$\dot{\boldsymbol{z}} = \boldsymbol{0} \ , \tag{2.2}$$

$$\boldsymbol{0} = \boldsymbol{g^{(0)}}(\boldsymbol{x}, \boldsymbol{y}) \ , \tag{2.3}$$

$$\boldsymbol{0} = \begin{cases} \boldsymbol{g^{i^-}}(\boldsymbol{x}, \boldsymbol{y}, \boldsymbol{z}) & \boldsymbol{y_{s,i}} < 0 \ , \\ \boldsymbol{g^{i^+}}(\boldsymbol{x}, \boldsymbol{y}, \boldsymbol{z}) & \boldsymbol{y_{s,i}} > 0 \ , \end{cases} \qquad i = 1, ..., s \tag{2.4}$$

$$\boldsymbol{z^+} = \boldsymbol{h_j}(\boldsymbol{x^-}, \boldsymbol{y^-}, \boldsymbol{z^-}) \quad \boldsymbol{y_{r,j}} = 0 \quad j \in 1, ..., r \tag{2.5}$$

where $\boldsymbol{x}$ is the vector of continuous dynamic state variables, $\boldsymbol{y}$ is the vector of algebraic state variables and $\boldsymbol{z}$ is the vector of discrete dynamic state variables. Equations (2.1) describe the differential equations, (2.3) and (2.4) describe the switched algebraic equations and (2.5) the state-reset equations. The superscript $^-$ stands for pre-event and $^+$ for post event values. The DSAR model (2.1)-(2.5) is a finite set of continuous DAEs expressed explicitly for each discrete variable change. This approach has been used for electro-mechanical dynamic analysis for power systems [58].

- **Illustrative example I:**

In order to demonstrate the ability of the DSAR structure, a simple power system network is considered with a tap-changing transformer. The test system consists of

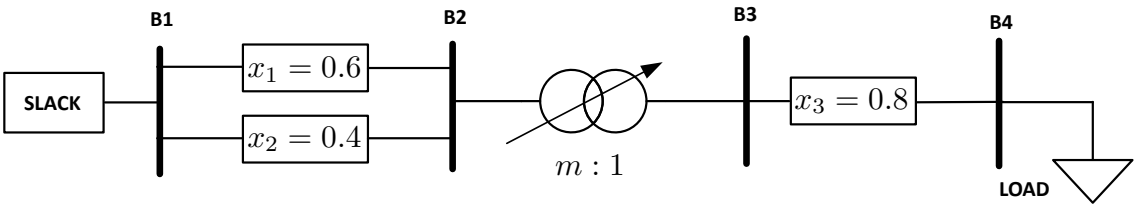

Figure 2.1: A single static generator connected to an infinite bus with a dynamic load.

four buses, one slack bus, one tap changing transformer, three transmission lines and one dynamic load. This test system and data are taken from [61] and is shown in Figure 2.1. In Figure 2.1 x_1,x_2 and x_3 are the line reactances in per unit.

The continuous dynamics of the real power load in bus 4 (B4) considered as a first order dynamic exponential recovery load given by:

$$\begin{aligned} T_p \dot{x}_p(t) &= -x_p(t) + p_o(v_t(t)^{\alpha_s} - v_t(t)^{\alpha_t}) \\ p_L(t) &= x_p(t) + p_o v_t(t)^{\alpha_t} \ , \end{aligned} \tag{2.6}$$

where, x_p is the load state driving the actual load demand p_L; v_t is the voltage at the load bus; α_s and α_t are exponents and p_o is the nominal active power load. The load undergoes an initial transient given by the term $p_o v_t^{\alpha_t}$ during a voltage disturbance and recovery of the load dictated by the time constant T_p.

Tap changing logic of the transformer is for low voltages i.e. for increasing tap ratio. Note that this tap changing transformer models are discussed in details in the next chapter. The model can be represented in the DSAR form as,

$$
\begin{aligned}
\dot{x}_1 &= y_1 y_7 \\
0 &= y_2 - v_3 + v_{\text{low}} \\
0 &= y_3 - y_4 + z_1 \\
0 &= y_6 - m + m_{\max} - m_{\text{step}}/2 \\
0 &= m v_2 - v_3 \\
0 &= y_1 - 1 \qquad \text{if } y_2 < 0 \\
0 &= \begin{cases} y_1 \\ y_4 - x_1 \end{cases} \qquad \text{if } y_2 > 0 \\
0 &= y_7 - 1 \qquad \text{if } y_6 < 0 \\
0 &= y_7 \qquad \text{if } y_6 > 0 \\
0 &= y_5 - x_1 + z_1 + T_{\text{tap}} \qquad \text{if } y_3 < 0 \\
0 &= y_5 - x_1 + y_4 + T_{\text{tap}} \qquad \text{if } y_3 > 0 \\
& \begin{cases} z_1^+ = x_1^- \\ m^+ = m^- + m_{\text{step}} \end{cases} \qquad \text{when} \quad y_5 = 0 \ ,
\end{aligned}
$$

where v_2 and v_3 are the bus 2 and 3 voltages respectively; m is the transformer tap ratio; x_1 is the state variable considered as a timer; T_{tap} is the time delay of the consecutive tap changes; $m_{\max}$ is the maximum tap ratio; m_{step} is the tap step and v_{low} is the voltage dead-band. All other algebraic ($y_1 - y_7$) and discrete variable (z_1) are internal variables.

The simulation is carried out by tripping the line with reactance, $x_2 = 0.4$ at

Table 2.1: Parameters of the illustrative example I

Component	**Parameters**
Slack	$\lvert v\rvert = 1.05,\ \angle\theta = 0$
Transformer	$v_{\text{low}} = 1.04,\ m_{\max} = 1.1,\ T_{\text{tap}} = 20\ s,\ m_{\text{step}} = 0.0125$
Load	$p_o = 0.4$ pu(MW), $T_p = 5,\ \alpha_t = 2,\ \alpha_s = 0$

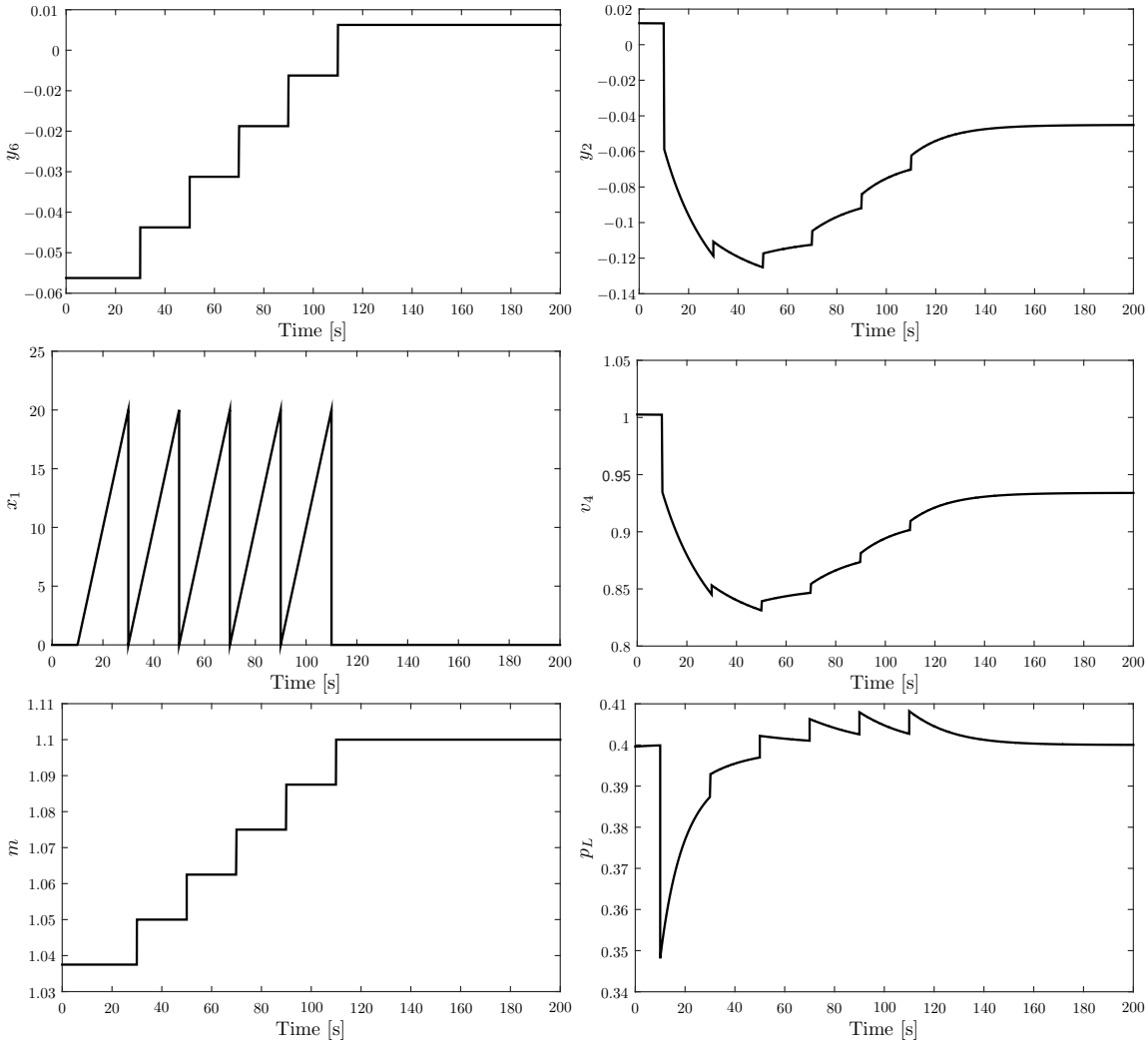

Figure 2.2: Trajectories of illustrative example I.

$t = 10$ s. The initial tap position is set to 1.0375. Data of the test system is given in Table 2.1. The simulation results are shown in Figure 2.2. The dynamics of the tap-changing transformer are driven by different events that govern the behavior of

the timer. If the voltage is within the dead-band ($y_2 > 0$) or the tap position is at the upper limit ($y_6 > 0$) then the timer is blocked. When the voltage is outside the dead-band ($y_2 < 0$), the timer will run and if the timer reaches $T_{\text{tap}}(y_5 = 0)$, a tap change occurs. After every tap change, the timer is reset but not necessarily blocked.

From the simulation results shown in Figure 2.2, it is evident that the proposed DSAR structure is capable of simulating combined continuous and discrete dynamics of power systems. However, Hiskens's formalism requires an additional algebraic variable for each discrete change. This is not strictly necessary. Moreover, this method is prone to deadlock if a sliding condition appears [60]. This is further addressed in Chapter 4-6.

2.3 Modeling in DOME

The hybrid framework used in this work considers a modified version of Hiskens's method. This framework does not require to create an additional algebraic variable (shown in Section 2.3.3), allows to identify deadlock situations (discussed in Chapter 5 and 6). In addition a semi-implicit method [75] is used to represent the mathematical model of power systems instead of an explicit DAE. The details of this modeling framework are discussed in this section.

2.3.1 Semi-implicit DAE Formulation

The following DRHS DAE formulation is used to represent the hybrid dynamical power systems,

$$\begin{aligned} \boldsymbol{T}(\boldsymbol{x},\boldsymbol{y})\dot{\boldsymbol{x}} &= \boldsymbol{f}(\boldsymbol{x},\boldsymbol{y},\boldsymbol{z}) \ , \\ \boldsymbol{R}(\boldsymbol{x},\boldsymbol{y})\dot{\boldsymbol{x}} &= \boldsymbol{g}(\boldsymbol{x},\boldsymbol{y},\boldsymbol{z}) \ , \end{aligned} \tag{2.7}$$

where $\boldsymbol{f}$ are the differential equations, $\boldsymbol{g}$ are the algebraic equations, $\boldsymbol{x}$, $\boldsymbol{x} \in \mathbb{R}^{n_x}$ are the state variables, e.g. generator rotor speeds, and $\boldsymbol{y}$, $\boldsymbol{y} \in \mathbb{R}^{n_y}$, are the algebraic variables, e.g. bus voltage magnitudes and $\boldsymbol{z}$, $\boldsymbol{z} \in \mathbb{N}^{n_z}$, are the discrete variables, e.g. status of discontinuous state variables. The functions $\boldsymbol{f}, \boldsymbol{g}$ are at least C^1. $\boldsymbol{T}(\boldsymbol{x},\boldsymbol{y})$ and $\boldsymbol{R}(\boldsymbol{x},\boldsymbol{y})$ are $n_x \times n_x$ and $m_y \times n_x$. Observe that this model becomes an explicit hybrid DAE, if $\boldsymbol{T}(\boldsymbol{x},\boldsymbol{y}) = \boldsymbol{I}_{n_x}$, where $\boldsymbol{I}_{n_x}$ is the identity matrix of order n_x and $\boldsymbol{R}(\boldsymbol{x},\boldsymbol{y}) = \boldsymbol{0}$.

Equation (2.7) is a collection of continuous DAEs, one per each discrete variable ($\boldsymbol{z}$) change using if-then rules. This is illustrated below,

$$\text{if (condition)} \ : \begin{cases} \boldsymbol{T}(\boldsymbol{x},\boldsymbol{y})\dot{\boldsymbol{x}} &= \boldsymbol{f_1}(\boldsymbol{x},\boldsymbol{y},\boldsymbol{z_1}) \ , \\ \boldsymbol{R}(\boldsymbol{x},\boldsymbol{y})\dot{\boldsymbol{x}} &= \boldsymbol{g_1}(\boldsymbol{x},\boldsymbol{y},\boldsymbol{z_1}) \ . \end{cases} \tag{2.8}$$

$$\text{else} \qquad\qquad : \begin{cases} \boldsymbol{T}(\boldsymbol{x},\boldsymbol{y})\dot{\boldsymbol{x}} &= \boldsymbol{f_2}(\boldsymbol{x},\boldsymbol{y},\boldsymbol{z_2}) \ , \\ \boldsymbol{R}(\boldsymbol{x},\boldsymbol{y})\dot{\boldsymbol{x}} &= \boldsymbol{g_2}(\boldsymbol{x},\boldsymbol{y},\boldsymbol{z_2}) \ . \end{cases} \tag{2.9}$$

In DOME, it is assumed that the numerical integration technique utilised to solve the time domain simulation is based on an implicit method, e.g., the implicit

trapezoidal method (ITM) or a backward-differentiation formula (BDF) [76]. It is also assumed that the elements of the Jacobian matrix of the DAEs, say $\boldsymbol{A_s} = \begin{pmatrix} \boldsymbol{f_x} & \boldsymbol{f_y} \\ \boldsymbol{g_x} & \boldsymbol{g_y} \end{pmatrix}$, are computed analytically and no symbolic re-factorization is required when a discrete variable is changed.

2.3.2 Event Handling

The conditions in the brackets of "if-else" block in (2.8-2.9) generally depend on time and/or state or algebraic variables. These conditions are known as *time event* and *state event* respectively [28] and briefly described below.

- **Time Events:** If the exact time at which discontinuity is known in advance of the simulation, it is known as a "time event". For example, opening a line connecting two buses at a certain time in a power system network during a time domain simulation can be scheduled in advance. As it is possible to set the point in time, a value change of discrete variable such events are handled efficiently.
- **State Events:** If the time of occurrence of a discontinuity is not known in advance, it is known as "state event". For example, if a state variable is limited to a constant magnitude, one does not know "a priori" if and when the variable will take the limit value. In such case, only the event condition is known rather than the event time and the event condition is specified in terms of a continuously varying state or algebraic variable.

The simulation of state events is not easy to implement because it requires to solve several issues, such as: event location, transversal intersections, exits from the discontinuity surface, sliding motions, etc. There are basically two methods to

perform all these tasks, namely, *time stepping* and *event driven* techniques. Both techniques are considered in DOME and briefly discussed below.

- **Time stepping method:** This method ignores the event location's detection and relies on the local error estimation to ensure the error remains acceptably small when a discontinuity occurs [41]. This method is common in power system software tools because it is less computationally demanding [47].
- **Event driven method:** This method detects the accurate time of the events using an event function. When the numerical simulation reaches an event point, the simulation restarts from that point [93]. Event functions are usually specified implicitly, i.e., in the form of zero-crossing functions. Therefore, the event detection method relies on when a variable associated with it crosses through zero [28, 111].

2.3.3 Illustrative Example II

Consider the Single Machine Infinite Bus (SMIB) system shown in Figure 2.3, the generator is equipped with an Automatic Voltage Regulator (AVR) as depicted in Figure 2.4. This AVR model is a DC1C type [8] and is described by the following differential and algebraic equations (considering the upper limit):

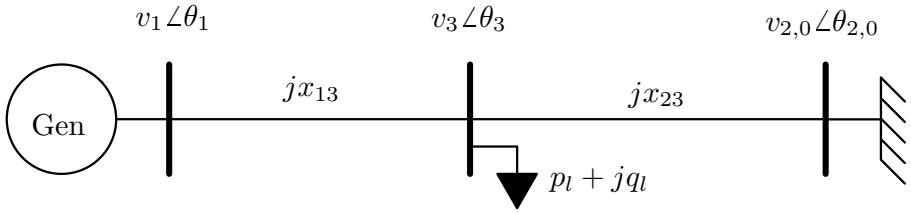

Figure 2.3: A single generator connected to an infinite bus.

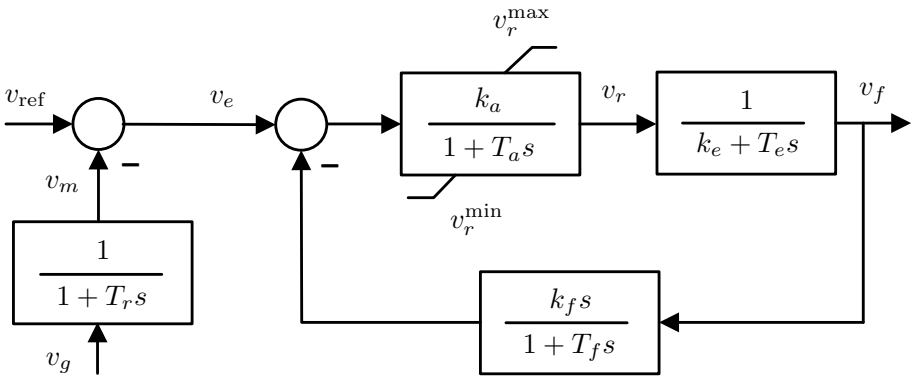

Figure 2.4: Block diagram of the DC1C type AVR.

$$T_r \dot{v}_m = v_g - v_m \ , \tag{2.10}$$

$$T_a \dot{v}_{r1} = (k_a(v_{\text{ref}} - v_m - v_{r2} - \frac{k_f}{T_f} v_f) - v_{r1}) z_1 \ , \tag{2.11}$$

$$T_f \dot{v}_{r2} = -(\frac{k_f}{T_f} v_f + v_{r2}) \ , \tag{2.12}$$

$$T_e \dot{v}_f = -(v_f k_e - v_r) \ , \tag{2.13}$$

$$0 = v_{r1} z_1 + v_r^{\max} z_2 - v_r \ . \tag{2.14}$$

where v_g is the measured voltage; v_{ref} is the reference voltage; T_r, T_a, T_f and T_e are the time constants; k_a and k_f are gains; v_f is the generator field voltage; v_m, v_{r1}, v_{r2} are the internal state variables and v_r is the algebraic variable.

The anti-windup limiter [8] on the amplifier of the AVR is implemented by changing the status of the discrete variables z_1 and z_2 (for simplification only upper limit is discussed), as follows,

$$\text{if } v_{r1} \geq v_r^{\max} : \begin{cases} z_1 & = 0 \ , \\ z_2 & = 1 \ , \end{cases} \tag{2.15}$$

$$\text{else} \qquad : \begin{cases} z_1 & = 1 \ , \\ z_2 & = 0 \ , \end{cases} \tag{2.16}$$

and the right hand side of the equations (2.11 and 2.14) are automatically switched. For both time stepping and event driven method the zero crossing or the event function is $v_{r1} - v_r^{\max}$.

In this example, the elements of Jacobian matrix $\boldsymbol{A_s}$ are derived analytically. This AVR block has, $\boldsymbol{x} = [v_m \ v_{r1} \ v_{r2} \ v_f]^T$; $\boldsymbol{y} = [v_r]$; $\boldsymbol{f(x, y, z)}$ are given by (2.10-2.13) and $\boldsymbol{g(x, y, z)}$ is given by (2.14). The elements of the $\boldsymbol{A_s}$ related to the AVR block are calculated using the partial derivatives: $\boldsymbol{f_x} = [\frac{\partial \boldsymbol{f(x,y,z)}}{\partial \boldsymbol{x}}]$; $\boldsymbol{f_y} = [\frac{\partial \boldsymbol{f(x,y,z)}}{\partial \boldsymbol{y}}]$; $\boldsymbol{g_x} = [\frac{\partial \boldsymbol{g(x,y,z)}}{\partial \boldsymbol{x}}]$ and $\boldsymbol{g_y} = [\frac{\partial \boldsymbol{g(x,y,z)}}{\partial \boldsymbol{y}}]$. Therefore calculating,

$$\boldsymbol{f_x} = \begin{bmatrix} \frac{\partial f_1}{\partial v_m} & \frac{\partial f_1}{\partial v_{r1}} & \frac{\partial f_1}{\partial v_{r2}} & \frac{\partial f_1}{\partial v_f} \\ \frac{\partial f_2}{\partial v_m} & \frac{\partial f_2}{\partial v_{r1}} & \frac{\partial f_2}{\partial v_{r2}} & \frac{\partial f_2}{\partial v_f} \\ \frac{\partial f_3}{\partial v_m} & \frac{\partial f_3}{\partial v_{r1}} & \frac{\partial f_3}{\partial v_{r2}} & \frac{\partial f_3}{\partial v_f} \\ \frac{\partial f_4}{\partial v_m} & \frac{\partial f_4}{\partial v_{r1}} & \frac{\partial f_4}{\partial v_{r2}} & \frac{\partial f_4}{\partial v_f} \end{bmatrix} = \begin{bmatrix} -1 & 0 & 0 & 0 \\ -k_a z_1 & -z_1 & -k_a z_1 & -\frac{k_a k_f}{T_f} z_1 \\ 0 & 0 & -1 & -\frac{k_f}{T_f} \\ 0 & 0 & 0 & -k_e \end{bmatrix}, \tag{2.17}$$

Table 2.2: Parameters of the SMIB system

Name	Values
Generator	$M = 8$, $D = 0$, $x'_d = 0.25$, $x_d = 1$, $p_m = 1$, $T'_{d0} = 6$
Line	$x_{13} = 0.3$, $x_{23} = 0.5$
Load	$p_l = 0.7$, $q_l = 0.01$
AVR	$k_a = 20$, $k_e = 1$, $k_f = 0.06$, $T_a = 0.2$, $v_r^{\max} = 1.5$, $T_r = 0.001$, $T_e = 1$, $T_f = 0.35$

$$\boldsymbol{f}_{\boldsymbol{y}}^T = \begin{bmatrix} \frac{\partial f_1}{\partial v_r} & \frac{\partial f_2}{\partial v_r} & \frac{\partial f_3}{\partial v_r} & \frac{\partial f_4}{\partial v_r} \end{bmatrix}^T = \begin{bmatrix} 0 & 0 & 0 & 1 \end{bmatrix}^T, \tag{2.18}$$

$$\boldsymbol{g}_{\boldsymbol{x}} = \begin{bmatrix} \frac{\partial g_1}{\partial v_m} & \frac{\partial g_1}{\partial v_{r1}} & \frac{\partial g_1}{\partial v_{r2}} & \frac{\partial g_1}{\partial v_f} \end{bmatrix} = \begin{bmatrix} 0 & z_1 & 0 & 0 \end{bmatrix}, \tag{2.19}$$

$$\boldsymbol{g}_{\boldsymbol{y}} = \begin{bmatrix} \frac{\partial g_1}{\partial v_r} \end{bmatrix} = \begin{bmatrix} -1 \end{bmatrix}. \tag{2.20}$$

The DAEs of the AVR (2.10-2.14) and Jacobian matrices (2.17-2.20) are used to implement the model in DOME. By following this, all other models are implemented too. Considering a third-order type generator model [76] the SMIB system (see Figure 2.3) is simulated by applying a three-phase fault at time $t = 1$ s for 150 ms and the parameters of all the components are given in Table 2.2. This perturbation at 1 s is an example of a time event. The trajectories of v_{r1}, v_f, v_3 and z_1 are shown in Figure 2.5. Following the fault state variable v_{r1} reaches to the maximum limit and the discrete variable z_1 switches to zero. This makes the right-hand side of equation (2.11) zero and precludes the windup affect. This is an example of a state event. A little bit after the fault is cleared v_{r1} returns within the limit and the integration starts again through switching z_1 to 1. In addition, for every switching of

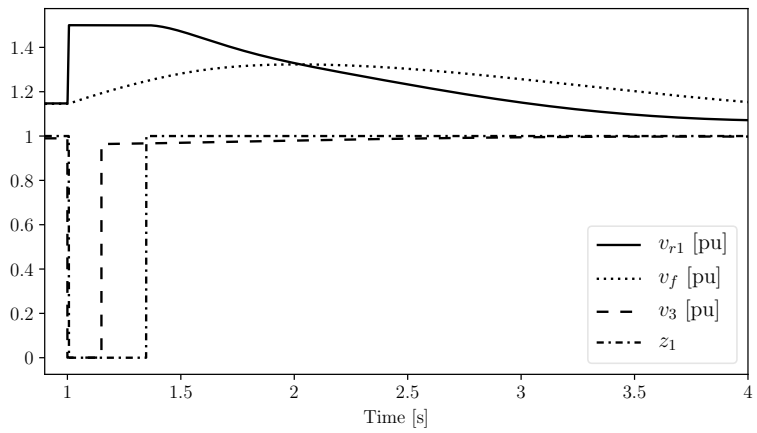

Figure 2.5: Trajectories of v_{r1}, v_f, v_3 and z_1 in the SMIB system.

z_1, a re-factorization of the Jacobian matrices is completed. However, the diagonal elements remain non-null to avoid the singularity.

2.4 Conclusions

This chapter introduces hybrid dynamical systems and discusses power systems' mathematical modeling as a class of hybrid systems. Specific implementations of hybrid models representing power systems for time-domain simulation are presented and illustrated through two examples. Hybrid automata are the most effective implementations and this is the model adopted in this thesis.

3 Under Load Tap Changers

3.1 Introduction

Long-term voltage control is aimed at maintaining the voltage magnitude of buses at the transmission and distribution levels within a given range and properly share the reactive power among available resources. The most common long-term voltage controllers equip the Under-Load Tap Changer (ULTC) transformers that interface transmission and distribution networks.

Most transformers those interfacing the transmission with the distribution systems, have under-load tap changing capability. The modeling of such transformers is crucial for long term voltage stability analysis [112] due to the presence of non-linearity (dead-band, time delay, discrete tap positions) in these transformers. Even though the circuit model of tap changing transformers is well known, the model of the controller of such devices differs depending on the applications and/or implementations [77].

As the integration of stochastic distributed renewable energy resources increases, undesirable voltage fluctuations are observed in different levels of power systems. While this behavior is expected, to properly reproduce the precise dynamic behavior of ULTC regulators through simulations is not a trivial task. Moreover, as thoroughly discussed in this chapter, the ULTC controller's implementation significantly

impacts the overall system dynamic response. This chapter addresses this modeling issue from a dynamic point of view, considering stochastic variation of the load power consumption and wind power generation at the distribution system level.

The effect of stochastic distributed generation such as wind power and photovoltaic on the frequency of tap change and performance of the ULTC have been studied in [17, 70, 99]. These studies are relevant from the economic point of view as 50% of maintenance cost of such transformers is related to the number of tap operations. However, the aforementioned studies are based on step-wise power flow solutions, and do not consider the dynamic behavior of ULTC controllers. Studies based on time domain or quasi-steady-state simulations are considered in [96] and [12], respectively. These references do not consider stochastic modeling.

Most of the previous studies showed the behavior of ULTC transformers considering either steady-state power flow or quasi steady-state analyses. This is adequate enough for the appraisal of power system operation. However, when considering a short period, e.g. within a time frame of 5 to 15 minutes, stochastic fluctuations due to loads and distributed generation can lead to variations of the tap changers that might not be captured using a steady-state or quasi-steady state approaches. That is why the focus of this chapter is on ULTC operations occurring in a time scale of 15 minutes.

The remainder of this chapter is organized as follows. Section 3.2 briefly introduces tap changer transformers and and Section 3.3 presents the discrete and continuous models of ULTCs and their controllers for dynamic studies. Section 3.5 discusses the dynamic response of such devices considering deterministic scenarios. Section 3.6 includes load and wind speed models formulated as stochastic differential equations which properly capture the probability distribution and autocorrelation of

the stochastic processes and Section 3.7 presents the stochastic case study. Finally, in Section 3.8, conclusions are drawn.

3.2 Under-Load Tap Changer

Transformers are ubiquitous in transmission and distribution systems. They connect sections of the network at different voltage levels. Depending on the system structure, these transformers are:

- Step-up transformers at generator terminals;
- Transformers connecting different transmission voltage levels; and
- Transformers feeding a distribution system.

Voltage control through changing transformer ratios by using "taps" at different voltage level is a common strategy. For example transformers feeding to a distribution system compensate changes in the voltage due to changes in the load without interruption employing a automatic tap changing mechanism. Such transformers are often known as Load Tap Changing (LTC) or ULTC or On Load Tap Changing (OLTC) transformer. Details of fundamentals on transformers can be found in [51]. Next the modeling of the circuit of ULTC transformers as well as a variety of discrete and continuous voltage control schemes are discussed.

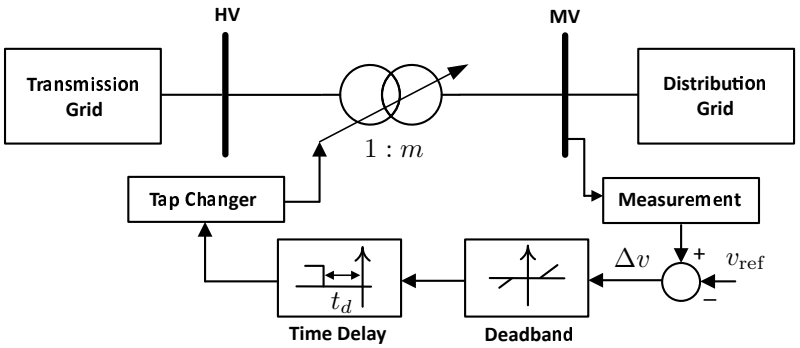

Figure 3.1: A tap-changer under-load transformer with a voltage controller.

3.3 Model

The general scheme of an ULTC transformer with automatic voltage control is shown in Figure 3.1. Three main physical components compose these transformers: (i) an automatic voltage regulator; (ii) a tap changer with a switching mechanism; and (iii) the main transformer.

The voltage regulator includes: (i) a measuring element to measure the voltage (or reactive power) on the connected bus; (ii) a unit to compare the difference between measured and reference quantity; (iii) a dead-band element that reduces the sensitivity of the controller; and (iv) a time-delay element that limits the number of variations of the tap position.

The tap changer selects a tap to change from the previous position using a switching principal and there exists several switching mechanisms. Few commonly found mechanisms are: the high-speed resistor type, the reactor type and the vacuum type [42]. The whole process of the tap changer is achieved through a driving mechanism.

An illustration of the switching sequence of a resistor-oil type ULTC comprising

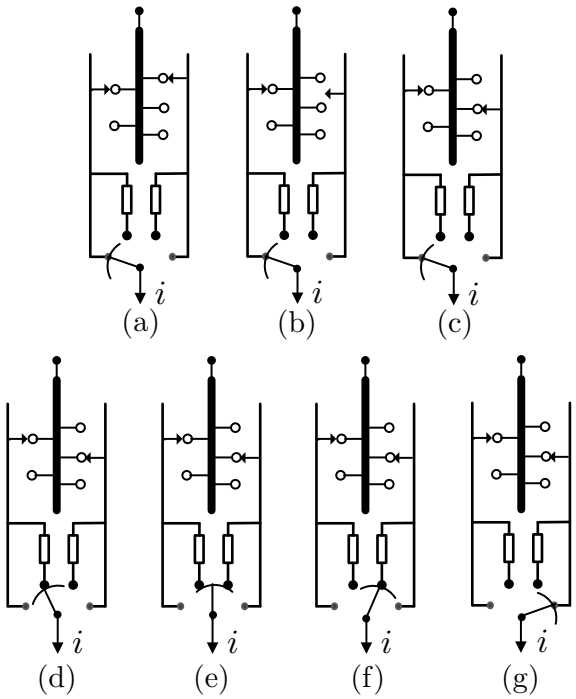

Figure 3.2: Sequence of switching of tap changer: tap selector (a-c) and diverter switch (d-g) [42].

a diverter switch and a tap selector in Figure 3.2. The tap selector first selects the tap at no load (see (a)-(c) in Figure 3.2). Next, the diverter switch transfers the load current selected tap from the tap in operation (see (d)-(g) in Figure 3.2). A driving mechanism completes the switching tasks.

3.3.1 Circuit

Figure 3.3 shows the equivalent circuit of a two-winding transformer assuming the tap is on the primary [76]. As $\bar{v}'_h = \bar{v}_h/m$, the currents injections at buses h'

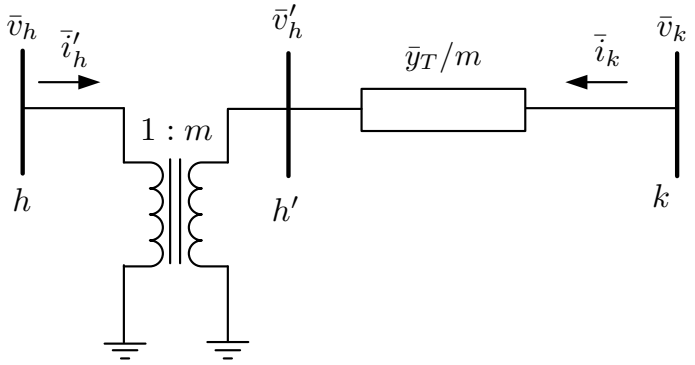

Figure 3.3: Equivalent circuit of the transformer with tap ratio module and series impedance.

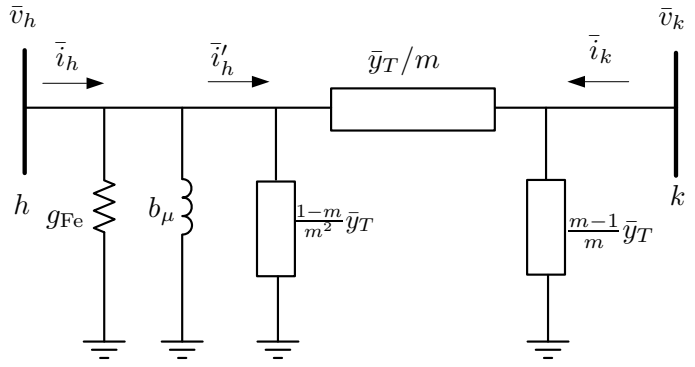

Figure 3.4: Equivalent circuit of a transformer.

and k are:

$$\begin{bmatrix} \bar{i}'_h \\ \\ \bar{i}_k \end{bmatrix} = \bar{y}_T \begin{bmatrix} \frac{1}{m^2} & -\frac{1}{m} \\ \\ -\frac{1}{m} & 1 \end{bmatrix} \begin{bmatrix} \bar{v}_h \\ \\ \bar{v}_k \end{bmatrix} . \tag{3.1}$$

Considering the physical buses h and k and including magnetization and iron losses on the primary winding (see Figure 3.4), one obtains:

$$\begin{bmatrix} \bar{i}_h \\ \\ \bar{i}_k \end{bmatrix} = \begin{bmatrix} g_{\text{Fe}} + jb_\mu + \bar{y}_T \frac{1}{m^2} & -\bar{y}_T \frac{1}{m} \\ \\ -\bar{y}_T \frac{1}{m} & \bar{y}_T \end{bmatrix} \begin{bmatrix} \bar{v}_h \\ \\ \bar{v}_k \end{bmatrix} , \tag{3.2}$$

where $\bar{y}_T = (r_T + jx_T)^{-1}$; g_{Fe}, b_μ, r_T and x_T are transformer iron loss, magnetizing susceptance, resistance and reactance respectively. Finally, the power injections at buses h and k are:

$$\begin{aligned} p_h &= v_h^2(g_{\text{Fe}} + g_T/m^2) - v_h v_k(g_T \cos\,\theta_{hk} + b_T \sin\,\theta_{hk})/m \ , \\ q_h &= -v_h^2(b_\mu + b_T/m^2) - v_h v_k(g_T \sin\,\theta_{hk} - b_T \cos\,\theta_{hk})/m \ , \\ p_k &= v_k^2 g_T - v_h v_k(g_T \cos\,\theta_{hk} - b_T \sin\,\theta_{hk})/m \ , \\ q_k &= -v_k^2 b_T + v_h v_k(g_T \sin\,\theta_{hk} + b_T \cos\,\theta_{hk})/m \ . \end{aligned} \tag{3.3}$$

Where p_h and q_h are the active and reactive powers at bus h; p_k and q_k are the active and reactive powers at bus k; θ_{hk} is the angle difference between bus h and k i.e., $\theta_{hk} = \theta_h - \theta_k$; g_T is the transformer conductance.

3.4 Control

In this section, two commonly used control models are considered based on the references [27, 77, 112, 119], namely, (i) the discrete model and (ii) the continuous model.

3.4.1 Discrete model

In this model, the tap ratio m is a discrete variable that can take only fixed values in the range of $m^{\max}$ and $m^{\min}$ by a fixed step Δm. The tap ratio can move up or down by one step Δm if the controlled voltage v_k deviates more than a given dead-band db with respect to the reference voltage v^{ref} for longer than a given period Δt. The switching logic of the tap ratio is:

$$m(t) = m(t - \Delta t) + f\big(e(t), c(t), \tau(t)\big)\ \Delta m\ , \tag{3.4}$$

where e models the dead-band, τ the time-delay, c is a memory function that stores the time elapsed since the tap change and $\tau = \tau_d + \tau_m$ is the time delay. τ_d is the adjustable time delay of the controller and τ_m mechanical switching time delay. The e and c are expressed as:

$$e(\Delta v(t), m(t - \Delta t), db, m^{\max}, m^{\min}) =$$
$$\begin{cases} 1, & \text{if } \Delta v(t) > db \text{ and } m(t - \Delta t) < m^{\max}\ , \\ -1, & \text{if } \Delta v(t) < -db \text{ and } m(t - \Delta t) > m^{\min}\ , \\ 0, & \text{otherwise}\ , \end{cases} \tag{3.5}$$

$$c(e(t), c(t - \Delta t)) =$$
$$\begin{cases} c(t - \Delta t) + \Delta t, & \text{if } e(t) = 1 \text{ and } c(t - \Delta t) \geq 0\ , \\ c(t - \Delta t) - \Delta t, & \text{if } e(t) = -1 \text{ and } c(t - \Delta t) \leq 0\ , \\ 0, & \text{otherwise}\ , \end{cases} \tag{3.6}$$

$$\tag{3.7}$$

where t is the current simulation time, $t - \Delta t$ is the previous simulation step.

The function f depends upon the mode of operation: sequential or non-sequential mode. The control mechanism of sequential and non-sequential models are shown in Figures 3.5 and 3.6, respectively. The timer is reset after each tap change in non-sequential mode whereas in sequential mode the timer is reset only after the voltage is back within the dead-band range.

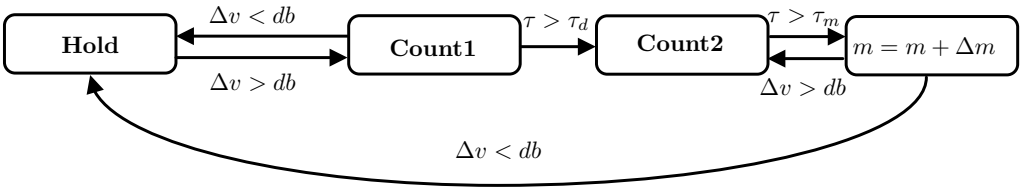

Figure 3.5: Sequential control mode.

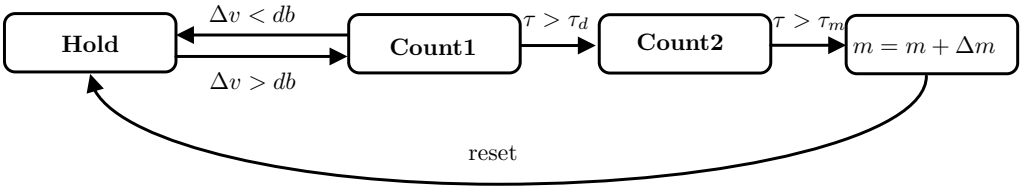

Figure 3.6: Non-sequential control mode.

The function f is as follows:

- For non-sequential mode,

$$f\big(e(t), c(t), \tau(t)\big) = \begin{cases} 1, & \text{if } e(t) = 1 \text{ and } c(t) > \tau(t) \\ -1, & \text{if } e(t) = -1 \text{ and } c(t) < \tau(t) \\ 0, & \text{otherwise ,} \end{cases} \tag{3.8}$$

- For sequential mode,

$$f\big(e(t), c(t), \tau(t)\big) = \begin{cases} 1, & \text{if } e(t) = 1 \text{ and } c(t) > \tau(t) \text{ ,} \\ & \text{for subsequent taps if } e(t) = 1 \text{ and } c(t) > \tau_m(t) \\ -1, & \text{if } e(t) = -1 \text{ and } c(t) > \tau(t) \text{ ,} \\ & \text{for subsequent taps if } e(t) = -1 \text{ and } c(t) > \tau_m(t) \\ 0, & \text{otherwise ,} \end{cases} \tag{3.9}$$

the time delay τ can be fixed or variable. In case of variable time delay, the higher the voltage error the faster the tap change. Depending on different time-delay settings four different discrete models are considered for both sequential and non-sequential mode and summarized below:

- D1: both delays are fixed, $\tau_d = \tau_{d,0}$ and $\tau_m = \tau_{m,0}$;
- D2: τ_d is combination of fixed and variable time, $\tau_d = \tau_{d,0} \cdot \frac{db}{|\Delta v|} + \tau_{d,1}$ and τ_m is fixed, $\tau_m = \tau_{m,0}$;
- D3: τ_d is variable, $\tau_d = \tau_{d,0} \cdot \frac{db}{|\Delta v|}$ and τ_m is fixed, $\tau_m = \tau_{m,0}$;
- D4: both delays are variable, $\tau_d = \tau_{d,0} \cdot \frac{db}{|\Delta v|}$ and $\tau_m = \tau_{m,0} \cdot \frac{db}{|\Delta v|}$.

3.4.2 Continuous model

The continuous control model approximates the tap ratio step Δm to be small, so that tap ratio m can vary continuously. The time delays are approximated as a

lag transfer function and the tap ratio differential equation is given by:

$$\dot{m}(t) = -Hm(t) + K\big(v_k(t) - v_{\text{ref}}\big) \ , \quad m^{\min} \leq m(t) \leq m^{\max} \ , \tag{3.10}$$

where H, K, v_k and v_{ref} are the integral deviation, inverse time constant, secondary bus voltage and controlled reference voltage, respectively. The dead-band is not included in this model. Note that it is possible to create an equivalent continuous model of each discrete model discussed in the previous Section [77].

3.5 Deterministic Case Studies

The impact of the voltage control action of different Under-Load Tap Changer (ULTC) discrete controller implementations to the long-term voltage stability is studied in this section using deterministic case studies.

3.5.1 Case Study 1: Four-Bus System

The four bus system presented in Section 2.2 is used. Compared to the illustrative example I discussed in Section 2.2, only the network data is modified to consider ULTC impedance. This is illustrated in Figure 3.7 and the ULTC data are given in Table 3.1. The adjustable and mechanical switching time delay parameters are also given in Table 3.1. To prevent unnecessary tap changes a non-zero adjustable time delay is generally used and depending the tap change switching mechanism the switching delay is varied. The range of these delay parameters is discussed in [112]. In this example The contingency consists of a line outage between B1 and B2 at $t = 5$ s ($x = 0.4$). Figures 3.8-3.9 show the trajectories of voltage at bus 3 for

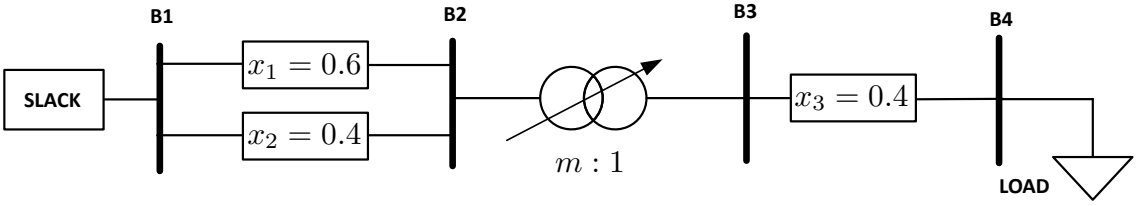

Figure 3.7: A single static generator connected to an infinite bus.

Table 3.1: Base case parameters of the test system of Figure 3.7

Component	**Parameters**
Discrete Model	$db = 4\%$, $\Delta m = 0.0125$, $\tau_{d,0} = 15$ s, $\tau_{d,1} = 5$ s, $\tau_{m,0} = 8$ s
All ULTCs	$m^{\max} = 1.1$, $m^{\min} = 0.8$, $r_t = 0$, $x_t = 0.4$ pu

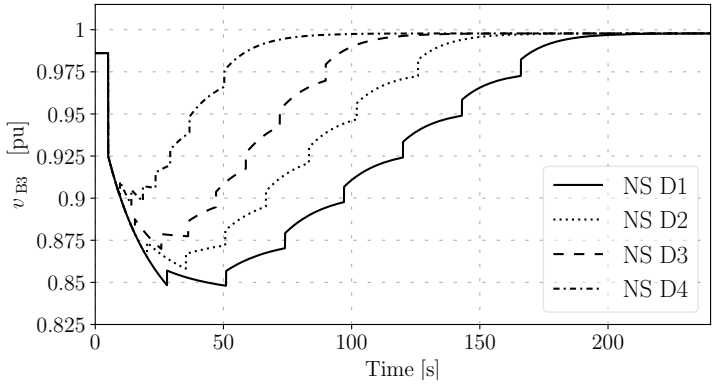

Figure 3.8: Voltage magnitude at bus 3 using non-sequential discrete ULTC models.

non-sequential and sequential discrete models respectively.

Following the disturbance, the voltage response is faster using the sequential models compared to the non-sequential models. This is due to the reset logic of the time delay (see Figures. 3.5-3.6). While using non-sequential tap changers the delay setting is reset after each tap change however for sequential model reset happens after the voltage level is restored within the normal operating range. That is why a faster response is achieved for sequential type model.

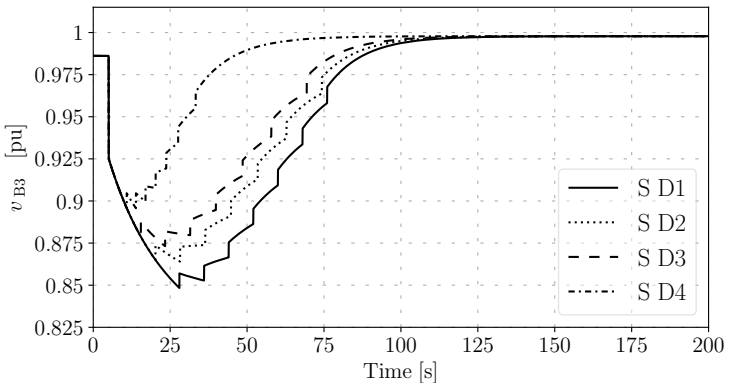

Figure 3.9: Voltage magnitude at bus 3 using sequential discrete ULTC models.

Comparing all non-sequential models (NS D1 - NS D4) and sequential models (S D1 - S D4), the voltage response is comparatively faster when moving from delay settings D1 to D4 because the time delay changes dynamically depending on the voltage deviation. Moreover, all ULTCs restore the voltage at the same voltage so number of tap operation is same for all ULTCs. These results indicate that the sequential model with variable time delay (D4) restores the voltage within the dead-band faster compared to all other discrete tap changers.

3.5.2 Case Study II: Nodic-32 System

The Nordic test system presented in [64] is used for the second deterministic case study. The system includes 74 buses; 102 branches, of which 20 step-up and 22 distribution transformers with ULTCs; 20 generators, of which 7 are round rotor and 13 are salient pole types, with Turbine Governors (TGs), Automatic Voltage Regulations (AVRs), Power System Stabilizers (PSSs), and Over-Excitation Limiters (OELs). The system consists of four areas: North, Central, Equivalent and South. The base case of the system is heavily loaded with large power transfers from North

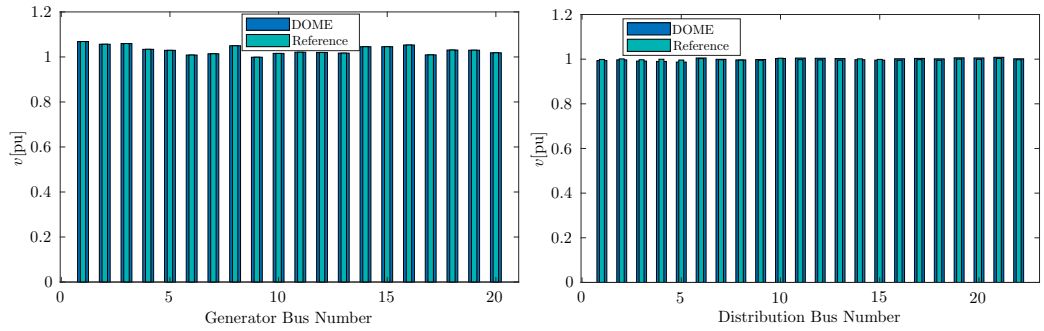

Figure 3.10: Voltages at the generator and distribution buses in DOME and reference [64].

to Central areas. The power flow results achieved in DOME for the base case are very close to the results given in [64]. Figure 3.10 shows the comparison of bus voltages in generator terminals and distribution buses respectively. Small mismatches in the power flow results are due the ULTCs in the network.

All dynamic models used in this case study match those reported in [64], except for the OELs, which are modeled as in [76]. Therefore using DOME trajectories achieved do not match exactly with reference [64], however dynamic solution shows similar stability issue. The parameters of all devices are also given in [64]. All distribution transformers are equipped with a ULTC controller with dead-band $db = 2\%$, maximum and minimum tap position are $m^{\max} = 1.2$ and $m^{\min} = 0.8$ with step size $\Delta m = 0.01$. The values for the time delays are given in Table 3.2.

The comparison discussed in this section considers the dynamic response following a three-phase fault at bus 4032, occurring at $t = 1$ s and cleared at $t = 1.06$ s by opening the line between buses 4032-4044. Transient response of voltage of a distribution bus at the Central area is shown in Figures 3.11-3.12 for non-sequential and sequential discrete tap changers respectively.

The line trip following the fault forces power to flow North-Central corridor over the remaining lines. However, the reactive power capabilities of the Central and

Table 3.2: Delays of ULTCs

Transformer	Delays (s)			Transformer	Delays (s)		
	τ_{d0}	τ_{d1}	τ_m		τ_{d0}	τ_{d1}	τ_m
11-1011	30	5	8	41-4041	31	5	9
12-1012	30	5	9	42-4042	31	5	10
13-1013	30	5	10	43-4043	31	5	11
22-1022	30	5	11	46-4046	31	5	12
1-1041	29	5	12	47-4047	30	5	8
2-1042	29	5	8	51-4051	30	5	9
3-1043	29	5	9	61-4061	30	5	10
4-1044	29	5	10	62-4062	30	5	11
5-1045	29	5	11	63-4063	30	5	12
31-2031	29	5	12	71-4071	31	5	9
32-2032	31	5	8	72-4072	31	5	11

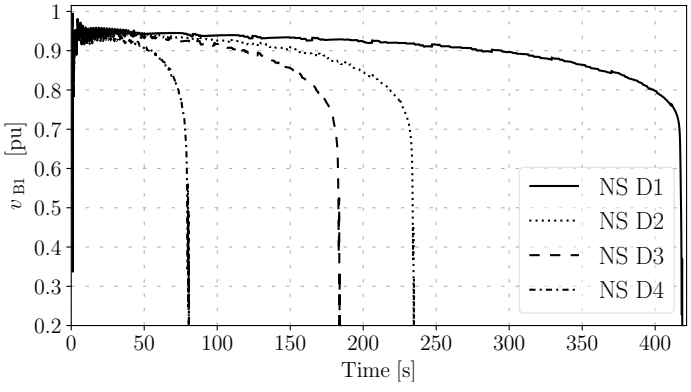

Figure 3.11: Voltage magnitude at bus 1 using non-sequential discrete ULTC models.

Northern generators impacts the maximum power delivered to the Central loads. On the other hand, the ULTCs try to restore the voltages of the distribution buses and load powers. In this case, however, the amount of power that the ULTCs have to restore is greater than the maximum power that can be delivered by the generation and the transmission system and, hence, a voltage instability occurs, which eventually leads to a voltage collapse. It is discussed in the previous example

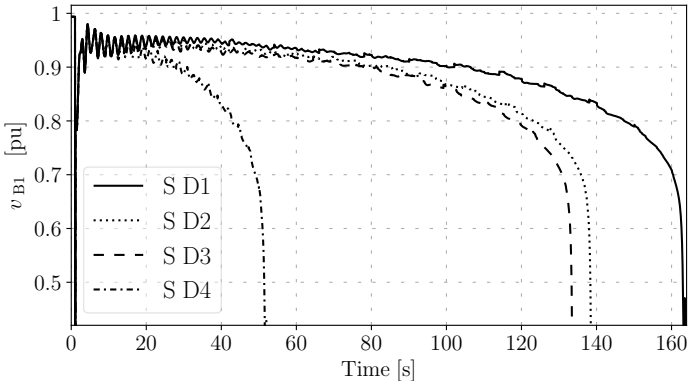

Figure 3.12: Voltage magnitude at bus 1 using sequential discrete ULTC models.

that the sequential models restore the voltage level faster compared to the non-sequential models. However in this case study if the ULTCs act faster the power mismatch will happen faster which in turn results in a faster collapse. The collapse occurs in the time scale of minutes, hence the notation *long-term voltage instability*.

Similar to Case Study 1 in Section 3.5.1, due to the dependency of the time-delay of the tap switching on the voltage error, non-sequential and sequential ULTC controllers show different transient responses. Due to its slow response, the non-sequential ULTCs controllers take a longer time than sequential ULTC controllers to drive the system to collapse.

3.6 Stochastic Modeling

This section outlines the load consumption and wind speed models considered in the stochastic case study discussed in the example of Section 3.7. These models include stochastic perturbations modeled by means of the following Itô-type differ-

ential equation:

$$\dot{\eta}(t) = a\big(\eta(t), t\big) + b\big(\eta(t), t\big)\ \xi(t)\ , \tag{3.11}$$

where η is the state variable that describes the stochastic process, a and b are the drift and the diffusion terms respectively, and ξ is the white noise, i.e. the formal time derivative of the Wiener process [52]. Equation (3.11) is a general expression that can take into account both Gaussian and non-Gaussian processes and is thus appropriate to model load power variations [78] and wind speed fluctuations [121].

3.6.1 Voltage Dependent Load

The well-known Voltage Dependent Load (VDL) model is given by [76]:

$$\begin{aligned} p_L(t) &= -p_{L,o}(v(t)/v_o)^\gamma\ , \\ q_L(t) &= -q_{L,o}(v(t)/v_o)^\gamma\ , \end{aligned} \tag{3.12}$$

where $p_{L,o}$ and $q_{L,o}$ are the active and reactive powers at the the nominal voltage v_o; v is the voltage magnitude of the bus where the load is connected; and γ is the power exponent. For the VDL model $\gamma = 2$.

Merging together the stochastic equation (3.11) and the load equations (3.12) lead to a Stochastic VDL (SVDL) load model. Since load variations are approximately Gaussian and show a constant standard deviation, we define the diffusion terms a and b in (3.11) to resemble an Ornstein-Uhlenbeck process [78]. The resulting

SVDL load model is:

$$\begin{aligned} p_L(t) &= (-p_{L,o} + \eta_p(t))(v(t)/v_o)^\gamma \ , \\ q_L(t) &= (-q_{L,o} + \eta_q(t))(v(t)/v_o)^\gamma \ , \\ \dot{\eta}_p(t) &= \alpha_p(\mu_p - \eta_p(t)) + b_p\xi_p(t) \ , \\ \dot{\eta}_q(t) &= \alpha_q(\mu_q - \eta_q(t)) + b_q\xi_q(t) \ , \end{aligned} \tag{3.13}$$

where the α terms are the speed at which the stochastic variables η are "attracted" towards the mean values μ, and the b terms represents the volatility of the processes.

3.6.2 Wind Speed

To emulate the wind speed, a and b in (3.11) must be defined so that the probability distribution of η is a Weibull process. It is also important to reproduce the autocorrelation of the wind speed, which is assumed to be exponentially decaying. This can be achieved through the regression theorem and the stationary Fokker-Planck equation, as thoroughly discussed in [121]. The resulting drift and diffusion terms are:

$$\begin{aligned} a\big(\eta(t)\big) &= -\alpha \cdot \big(\eta(t) - \mu_{\mathrm{W}}\big) \ , \\ b\big(\eta(t)\big) &= \sqrt{b_1\big(\eta(t)\big) \cdot b_2\big(\eta(t)\big)} \ , \end{aligned} \tag{3.14}$$

where α is the autocorrelation coefficient; μ_{W} is the mean of the Weibull distribution; and

$$\begin{aligned} b_1\big(\eta(t)\big) &= \frac{2\ \alpha}{p_{\mathrm{W}}\big(\eta(t)\big)} \ , \\ b_2\big(\eta(t)\big) &= \lambda \cdot \Gamma\left(1 + \frac{1}{k}, \left(\frac{\eta(t)}{\lambda}\right)^k\right) - \mu_{\mathrm{W}} \cdot e^{-(\eta(t)/\lambda)^k} \ , \end{aligned}$$

where p_W is the Weibull Probability Density Function (PDF); Γ is the incomplete Gamma function; k and λ are the shape and scale parameters of the Weibull distribution, respectively.

3.7 Stochastic Case Study

The test network considered in this example is a small Irish distribution system with both radial and meshed configurations [81]. The network includes eight buses, six loads, two wind generation, one slack bus and eight transmission lines. The operating nominal voltage of B1-B8 is 38 kV and the buses are fed by an ULTC type step down transformer from a 110 kV network. The network topology is shown in Figure 3.13. Network parameters can be found in [81].

The active and reactive power loading of the system are 15.02 MW and 8.29 MVAr respectively and the nominal wind farm capacities are 12 MW and 20 MW at B5 and B3 respectively. 5% of the loads is a SVDL modeled as in (3.13) and the 95% is modeled as constant PQ ($\gamma = 0$ in (3.13)). The wind generator model is a 5th-order doubly-fed induction generator with variable-speed wind turbine having discrete pitch control, first-order AVR, turbine governor and Maximum Power Point Tracking (MPPT). The input to wind turbine is a stochastic wind modeled as in (3.14).

Five different case studies are considered for different delay and dead-band settings of the discrete ULTC models. 500 15-minute Monte Carlo simulations are considered for each model and parameter set. The average number of tap operations using sequential type ULTCs for different dead-band and time-delay settings are

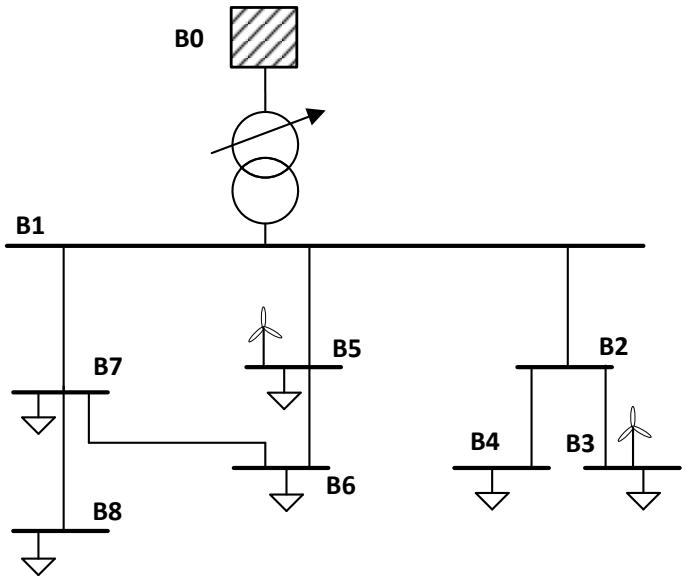

Figure 3.13: Topology of the test distribution network [81].

Table 3.3: Average number of tap operations using sequential discrete models

Cases	Parameter			D1	D2	D3	D4
	db	τ_{d0}	τ_{m0}				
C1	2.2	15	8	4.40	3.46	4.72	7.94
C2	2.4	15	8	2.43	2.23	2.56	2.60
C3	2.5	15	8	1.79	1.68	1.83	1.85
C4	2.5	20	10	1.60	1.43	1.64	1.66
C5	3	15	8	0.97	0.95	0.97	0.97

given in Table 3.3. As expected, the higher the time delay and dead-band, the lower the number of tap changes. This case study only considers sequential type ULTCs. Due to the stochastic variation of the load and wind speed, non-sequential ULTC controller models also yield similar results as sequential types because of similar delay logic of first tap switch.

Figures 3.14 and 3.15 show 500 trajectories of the voltage at bus 1 for cases C1 and C5 (see Table 3.3) with D1 type discrete model. These figures also include the mean, μ, and $\mu \pm 3\sigma$, where σ is the standard deviation. The mean and the

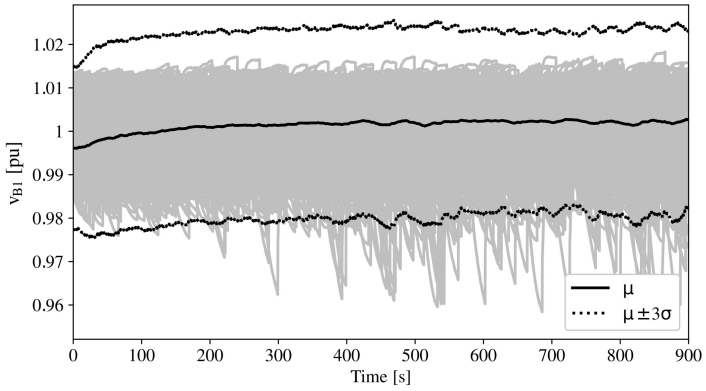

Figure 3.14: 500 stochastic trajectories and statistical properties of the bus 1 voltage using sequential discrete model (D1) for case C1.

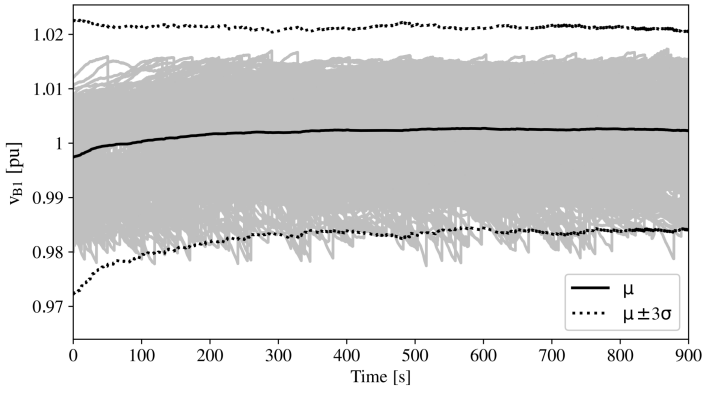

Figure 3.15: 500 stochastic trajectories and statistical properties of the bus 1 voltage using sequential discrete model (D1) for case C5.

standard deviation of the 500 trajectories are calculated at every time instant of the simulation interval which is 0.01 s. Observe that the distribution of the trajectories is non-Gaussian. The average voltage trajectory is similar in both figures, however C1 shows more than four times the tap operations of C5. Thus stochastic variations are important to take account for preventing unnecessary tap changes.

3.8 Conclusions

This chapters presents modeling and control of ULTCs for deterministic and stochastic studies. The dead-band and delay settings of ULTCs play a vital role in voltage restoration or collapse of the system. The deterministic case studies shows that with the same number of tap changes sequential and non-sequential models show different dynamic response. Though sequential models are preferred for a faster dynamic performance but they can also contribute to faster system collapse. Therefore this aspect has to taken account during system planning.

This Chapter presents an in detail stochastic case study through Monte Carlo simulation to calculate the number of tap changes considering a 15-minute operating window. When considering stochastic processes, the time domain analysis can properly take account for ULTC tap variations as these cannot be rightly captured considering steady-state analysis. Until now only steady-state analysis is considered. Simulation results also allow concluding that, depending on the ULTC control model, the number of tap operations can be significantly different, so it is crucial to implement the right control logic accurately. This is another aspect that cannot be captured by conventional steady-state analyses.

4 Limiters of PI Controllers

4.1 Introduction

PI controllers are ubiquitous in power system applications, such as FACTS devices [97], VSCs [91], IEEE standard excitation system models ST4C, ST6C, ST8C, AC7C and AC11C [8], standard model for type-III wind turbine generators developed by the Western Electricity Coordinating Council (WECC) [2], among others because of their simple structure, easy tuning and overall good dynamic performance. While the normal operation of PI controllers is univocal and straightforward to implement, there is no commonly accepted standard for the implementation of hard limits on PI controllers. This modeling uncertainty is particularly critical for VSC-based applications where it is crucial to keep the currents of the converter within their operational limits. Also, due to the open access market and integration of stochastic renewable energy, VSC applications of power systems are currently often operated closer to their limits.

Figure 4.1 shows a real-world example of such a situation, where the High-Voltage Direct Current (HVDC) links of Great Britain are operated at their limits for a significant period of time during daily operation [3]. To protect the converter switches from any over current the VSCs employ current limiters. Therefore it is important to take into account the current limiters of VSC-based devices and adequately model their hard limits.

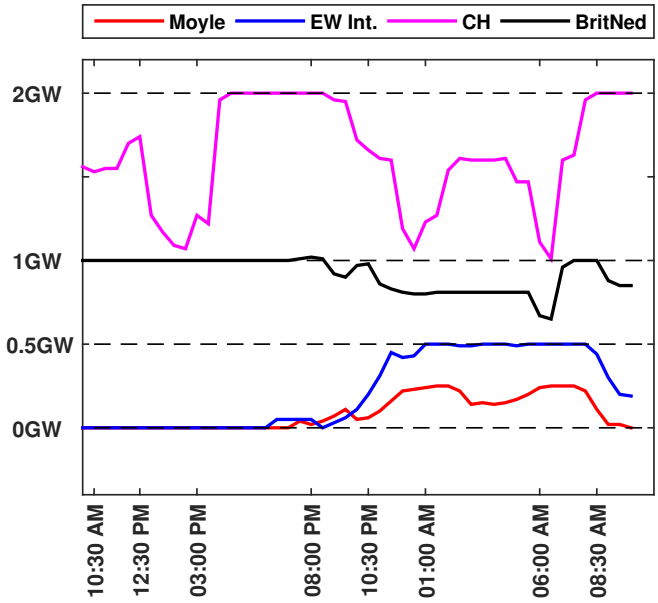

Figure 4.1: Power flow through the HVDC links of Great Britain (GB): Moyle (0.5 GW), East–West Interconnector (0.5 GW), HVDC Cross-Channel (CH, 2 GW) and BritNed (1 GW) in July 03-04, 2017 [3].

This chapter addresses the modeling issue of PI controllers from a simulation point of view and studies the impact of different implementations of PI limiters on the dynamic response of power systems.

The remainder of this chapter is organized as follows. Section 4.2 introduces different limiting methods of PI controllers and Section 4.3 discusses the implementation and numerical issues associated with PI controllers with anti-windup limiters. Next, Section 4.4 presents the model of the VSC, its controllers along with tuning method and shows how the limiting methods are applied to the controllers of the VSC-based devices. Then Section 4.5-Section 4.7 illustrate the dynamic behavior of the PI limiters of VSCs through WSCC 9-bus network and two real-world case studies: (i) a 1,479-bus dynamic model of the all-island Irish system connected to a simplified 63-bus dynamic model of the GB system through an HVDC link that represents the East-West Interconnector (EWIC); and (ii) a 74-bus dynamic

model of the Nordic system with the inclusion of a STATCOM device. Finally a brief discussion on simulation results and conclusions are drawn in Section 4.8 and Section 4.9 respectively.

4.2 PI Controllers

The Proportional, Integral and Differential (PID) control is the most common control technique utilized in engineering applications. In power systems, the derivative component is often dropped as it can deteriorate the dynamic performance due to the presence of noise and the occurrence of large disturbance [16]. Thus in this work PI controllers are considered.

Figure 4.2 shows the schemes of the PI controllers considered in the remainder of this chapter. These include an unconstrained standard PI model; a PI with windup limiter; the PI with conditional integrator anti-windup limiter recommended by the IEEE standard 421.5-2016; three back-calculation (or tracking anti-windup) anti-windup types of PI controllers limiters; and a PI with combined conditional and back-calculation limiter. Each model is discussed below.

4.2.1 Linear Model

PI0 is the conventional model without constraints:

$$\begin{aligned} \dot{x} &= k_i u \ , \\ y &= k_p u + x \ , \end{aligned} \tag{4.1}$$

where u, y, x, k_p and k_i are the input, output without limits, state variable,

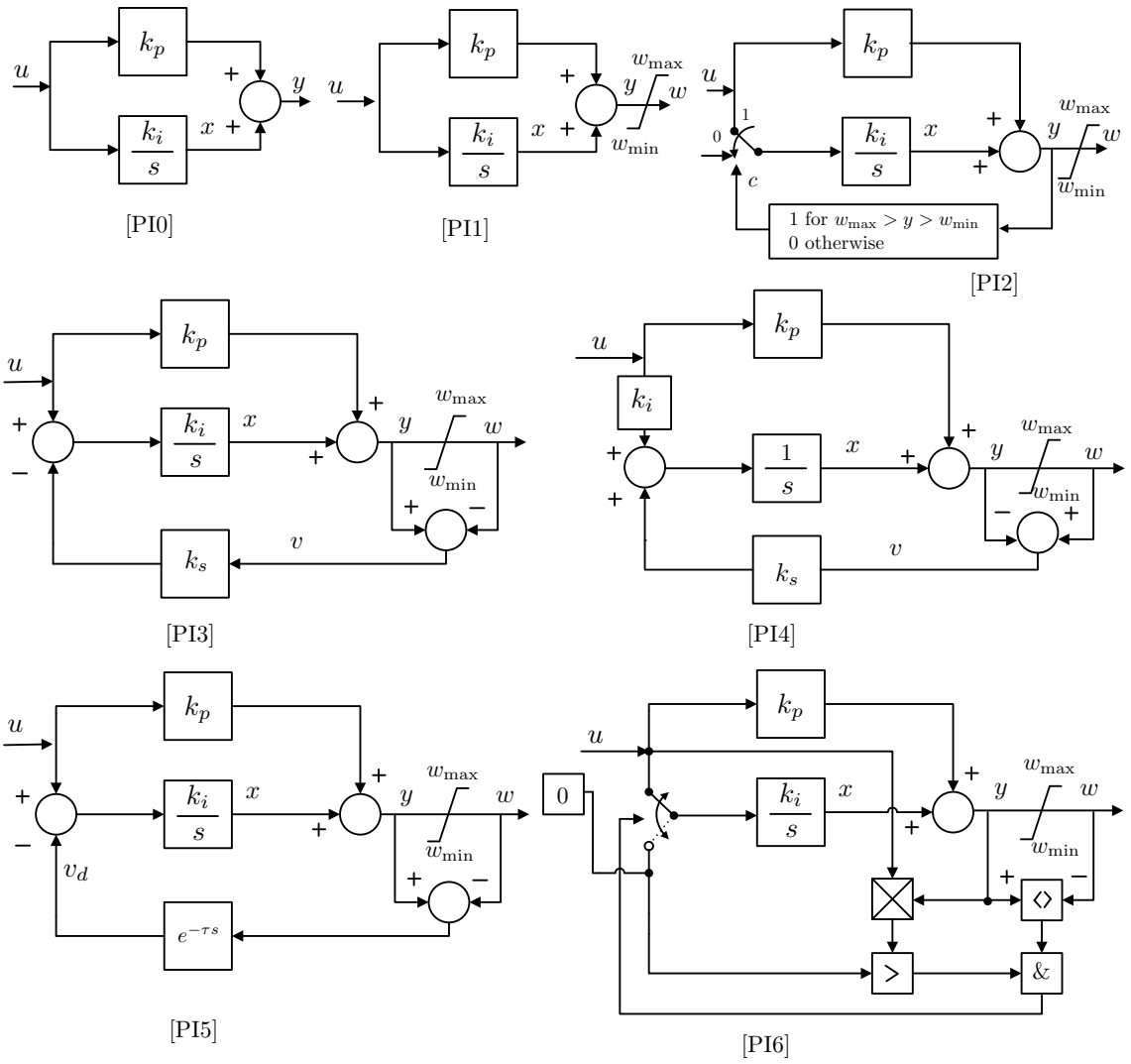

Figure 4.2: PI models: (PI0) no limits; (PI1) windup limiter; (PI2) IEEE Standard 421.5-2016 with conditional integrator; (PI3) back calculation type I, (PI4) back calculation type II; (PI5) back calculation with delay; and (PI6) combined conditional and back calculation.

proportional and integral gains, respectively.

4.2.2 Windup Limiter

The PI1 model only limits the output y and thus the integral action is continuous (smooth). This model is given by (4.1) and:

$$w = \begin{cases} w_{\max} & \text{if } y \geq w_{\max} \ , \\ y & \text{if } w_{\min} < y < w_{\max} \ , \\ w_{\min} & \text{if } y \leq w_{\min} \ , \end{cases} \tag{4.2}$$

where w is the limited output of the controller; $w_{\max}$ and $w_{\min}$ are the maximum and minimum limits respectively.

4.2.3 Anti-windup Limiters

Models PI2 to PI6 include an anti-windup (AW) limiter. Only the AW models commonly used in power system devices and software tools are considered. The interested reader can find a detailed theoretical treatment of AW limiters of PI controllers in [54].

- **Conditional integrator:** Conditional integration techniques consist in switching off the integration to avoid windup effects depending on certain conditions on the variables of the PI. There are several definitions of the switching conditions [116]. PI2 implements the solution proposed in IEEE Standard 421.5-2016 for

power system applications, as follows [8]:

$$\begin{aligned} &\text{if } y \geq w_{\max} : w = w_{\max} \text{ and } \dot{x} = 0 \ , \\ &\text{if } y \leq w_{\min} : w = w_{\min} \text{ and } \dot{x} = 0 \ , \\ &\text{otherwise} : w = y = k_p u + x \text{ and } \dot{x} = k_i u \ . \end{aligned} \tag{4.3}$$

- **Back calculation:** The back calculation technique consists in tracking the difference $v = y - w$ and using v as a feedback signal to compensate the input of the integrator channel of the PI when the output limits are binding. This method is also known as *tracking anti-windup* or *anti-reset windup* and can be implemented in several ways [108]. Three different tracking types are considered. Among these, two utilize the feedback signal with gain (PI3 and PI4); and the third one implements the feedback as a pure delay (PI5).

  The model of PI3 is [65]:

$$\dot{x} = k_i u - \widehat{k}_s v \ , \tag{4.4}$$

  where $\widehat{k}_s = k_i k_s$ and k_s is the feedback gain.

  The model of PI4, which is used in the software tool Simscape [6], is [59]:

$$\dot{x} = k_i u - k_s v \ , \tag{4.5}$$

  PI5 is available in the software tool EMTP-RV [74] among several other AW techniques. The integral action is:

$$\dot{x} = k_i (u - v_d) \ , \tag{4.6}$$

where $v_d = v(t - \tau)$ is the delayed feedback signal and τ is the constant time delay.

- **Combined conditional and back-calculation:** Model PI6 combines a conditional integration and a back calculation approach, where the summing point that performs the feedback to the integral term is replaced by a switch [76, 116]. The status of the switch depends on the following conditions:

$$\begin{aligned} \text{if } y \neq w, \text{ and } uy > 0 \ &: \dot{x} = k_i(u - v) \ , \\ \text{otherwise} &: \dot{x} = k_i u \ . \end{aligned} \tag{4.7}$$

4.3 Numerical Issues

This section discusses numerical issues arising from the software implementation of PI controller models presented in Section 4.2, as well as available techniques and modeling solutions to avoid such issues. In particular, this section discusses the *deadlock* (or *chattering*) phenomenon that occurs in model PI2 [48, 60]. Particular care is devoted to properly distinguish numerical problems due to the discretization required by computer-based integration schemes from the actual behavior of the PI controllers due to their hardware implementation. It is important that the discussion of section considers limit values of PI controller models are constant during time domain simulation.

4.3.1 Software Implementation of PI controllers

The software implementation of models PI0 to PI6 is discussed below.

- Model PI0 is linear and, thus, does not show any numerical issues, except those due to possible discontinuities and jumps of the input signal u, which are not discussed here.

- Model PI1 implements a windup limiter. This means that only the output algebraic variable w is affected by the limits. The windup limits do not lead to any numerical issue.

- Model PI2 can be implemented in various ways, some of which are known to lead to numerical issues. The numerical issue is addressed in Section 4.3.2. The implementation consists in introducing a discrete variable z in the equation of the integrator channel of the PI:

$$\dot{x} = k_i u z \ , \tag{4.8}$$

  with $z = 1$ if the output of the PI controller is not saturated, and $z = 0$ otherwise. If, during the simulation, z switches from 1 to 0, x becomes constant.

- Models PI3-PI4 do not switch the dynamic state during the simulation, so it does not require to use a discrete variable and do not present numerical integration issues.

- Model PI5 uses a delay, whose integration can lead to spurious oscillations, even with A-stable integration schemes such as the ITM [21]. However, no numerical issue arises for the typical values of the delays of model PI5 used in power system applications.

- Model PI6 is described by a set of hybrid DAEs, i.e., DAEs that mix continuous and discrete variables. It has to be noted that, in this case, discrete variables are part of the actual hardware implementation, not just a modeling issue. Physical

Boolean variables, however, are treated in the same way as those introduced to emulate windup and anti-windup limits in models PI1 and PI2, respectively.

4.3.2 IEEE Standard 421.5-2016

The state transitions of PI2 model are illustrated in Figure 4.3. The model has three different states namely, integration (INT); maximum (MAX) and minimum (MIN). In this section a simple example is used to explain the deadlock phenomenon that can occur when using model PI2.

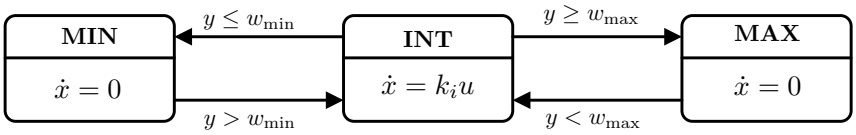

Figure 4.3: State transitions of the anti-windup PI controller model.

Let us assume that the following input signal is given to a model PI2:

$$\text{if } t > 2 \ \& \ \ t < 6 \text{ then: } \dot{u} = -1 \ ,$$

$$\text{else: } \dot{u} = 1 \ ,$$

and assume the following parameters, $w_{\max} = 1.2$, $w_{\min} = -1.2$, $k_i = 20$, $k_p = 1$ and the initial values for $t = 0$ are $x_0 = 0.05$ and $u_0 = 0$. The system is simulated for 10 s with a time step 0.001 s. Simulation results are shown in Figure 4.4. Below, we describe how a deadlock condition is reached.

- For $t < 2$ the input u to the PI controller increases. Hence, the algebraic variables of the PI, y and w, increase. Just before 1 second, $y > w_{\max} = 1.2$, w becomes constant, the integrator is locked and $\dot{x}$ switches to 0.

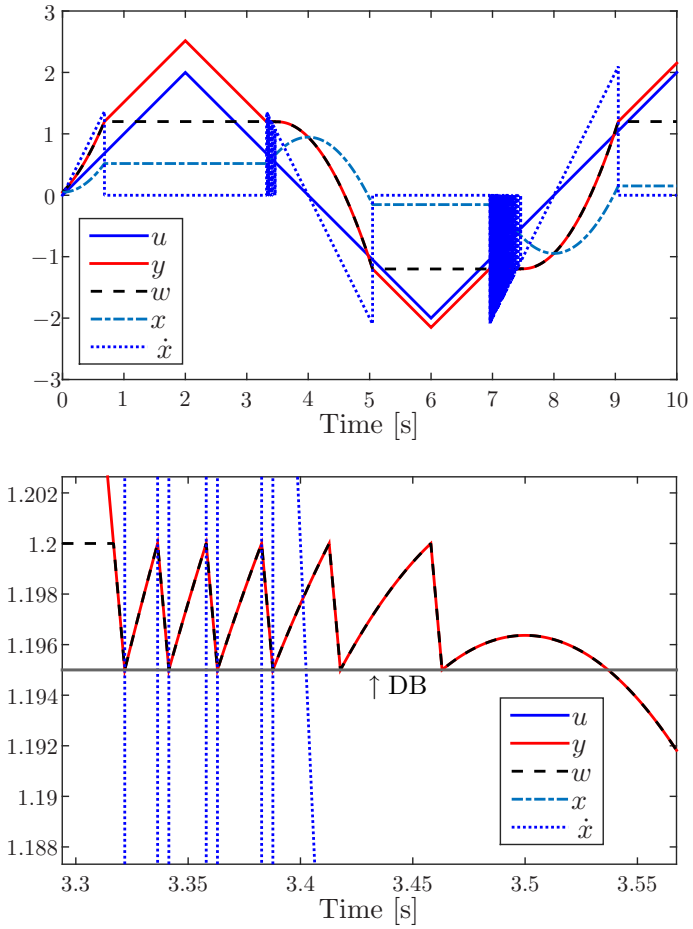

Figure 4.4: Simple example to explain the deadlock phenomenon that occurs with the PI2 model.

- For $t > 2$, u and y decrease.
- At $t = 3.317$ s, $y < 1.2$ and the integrator should unlock. However, at the very same time, $u > 0$ and, so, also $\dot{x} > 0$. Then x will increase, thus causing y to increase again towards $w_{\max}$. Depending on the time step of the integration and on the value of $\dot{x}$ and on the rate of change of the input u, a deadlock (cycling) situation can arise which consists in locking and unlocking the state variable x preventing the numerical integration to converge.

In the next chapter it is shown that this issue cannot be removed by reducing the

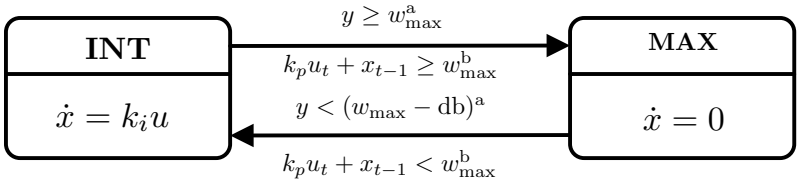

Figure 4.5: State transitions of the anti-windup PI controller for existing solutions: superscripts a and b indicate the deadband- and time delay-based techniques, respectively.

time step of the integration scheme, thus, this deadlock is not just a software issue. In any case, the digital hardware implementations also work with discrete quantities and are thus prone to the same issues as the numerical integration. There exists several techniques to avoid the numerical deadlock of the IEEE Std. type AW PI controller. These are the following.

- **DB (S1):** A deadband (DB) is included into the switching logic of the integrator [59]. The DB is implemented in such a way that if the integrator is locked, it can not be unlocked unless the output w reaches the DB boundary. This technique is illustrated in Figure 4.5. This solution also known as hysteresis [60], with similar properties and issues of the deadband. As resulting equations for both approaches are same, in this work DB approach is considered.

- **LIT (S2):** A decoupled AW on the integrator [48], known as Limited Integrator Technique (LIT). The complete model is given by the following two sets of if-then loops:

$$\begin{aligned} &\text{if } y \geq w_{\max} : w = w_{\max} \ , \\ &\text{if } y \leq w_{\min} : w = w_{\min} \ , \\ &\text{otherwise} : w = y = k_p u + x \ , \text{ and} \end{aligned} \tag{4.9}$$

$$
\begin{aligned}
&\text{if } x \geq x_{\max} \text{ and } k_i u \geq 0 \ : x = x_{\max} \text{ and } \dot{x} = 0 \ , \\
&\text{If } x \leq x_{\min} \text{ and } k_i u \leq 0 \ : x = x_{\min} \text{ and } \dot{x} = 0 \ , \\
&\text{otherwise} : \dot{x} = k_i u \ .
\end{aligned} \tag{4.10}
$$

- **Semi-implicit (S3):** This technique consists in using a semi-implicit DAE formulation [48] to convert the integrator state variable into an algebraic variable to continue the simulation during deadlock.

- **TD (S4):** To move from the INT state to the MAX or the MIN, this method considers the value of the integrator state variable from the previous time step (see Figure 4.5).

- **No-Convergence (S5):** A simulator forces the solver to move to the next time step after certain number of iterations even if the solver does not converge.

The drawbacks of the techniques: DB, TD and No-Convergence above are that they do not truly represent the hybrid model and introduce artificial chattering. Though it does not show chattering, the semi-implicit formulation (S3) does not consider the effect of disturbances of the input to evaluate state transitions while the state is in the deadlock region [48]. Moreover, the semi-implicit formulation requires a solver-dependent implementation and is not supported by most software tool. Finally, LIT does not yield same mathematical model of IEEE Std. (PI2).

In the remainder of this chapter, only DB and LIT are considered. Note that using a DB of 0.005 the trajectory of the PI shown in Figure 4.4 does not show a deadlock. However, the value of the DB is problem-dependent and cannot be fixed *a priori*. Further discussion on this point is provided in Section 4.7.1.

4.4 Voltage-Sourced Converter

In recent years, the voltage-sourced converter (VSC) has become the most common AC/DC device for renewable generation, energy storage systems and HVDC connections. Both electromagnetic and averaged models have been proposed [91]. For the purpose of transient stability analysis, the Average Value Models (AVM) of electronic converters appears the most adequate [30,31]. The AVM of the VSC along with its control, parameter tuning and constraints are presented in the remainder of this section.

4.4.1 Dynamic Model of the VSC

The configuration of a VSC is depicted in Figure 4.6 which includes a transformer in the AC side, a bi-directional AC/DC converter, a condenser and its controllers.

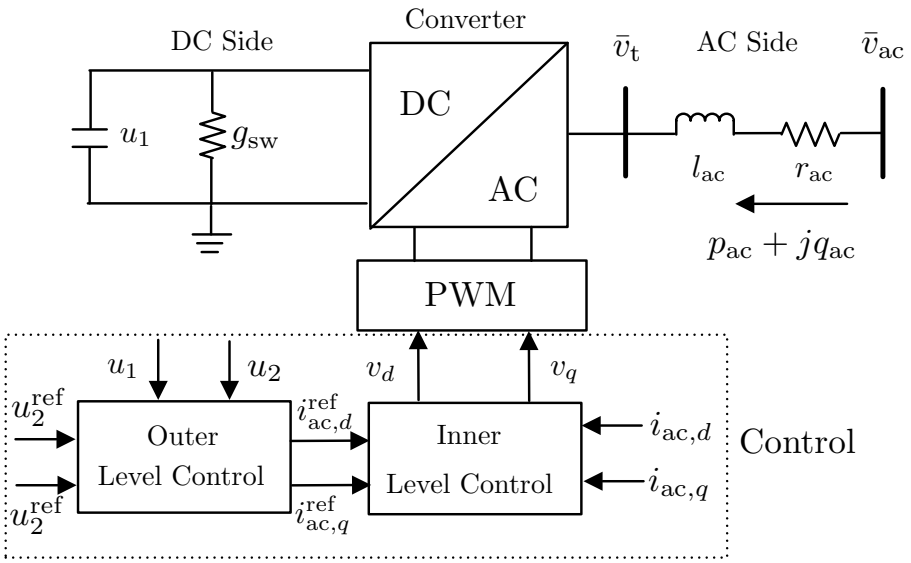

Figure 4.6: VSC scheme interfacing a DC grid with an AC grid.

The dynamics of the AC side of the VSC considering a rotating dq-frame are

given by:

$$\begin{aligned} r_{\mathrm{ac}} i_{\mathrm{ac},d} + l_{\mathrm{ac}} \frac{di_{\mathrm{ac},d}}{dt} &= \omega_{\mathrm{ac}} l_{\mathrm{ac}} i_{\mathrm{ac},q} + v_{\mathrm{ac},d} - v_{\mathrm{t},d} \ , \\ r_{\mathrm{ac}} i_{\mathrm{ac},q} + l_{\mathrm{ac}} \frac{di_{\mathrm{ac},q}}{dt} &= -\omega_{\mathrm{ac}} l_{\mathrm{ac}} i_{\mathrm{ac},d} + v_{\mathrm{ac},q} - v_{\mathrm{t},q} \ , \end{aligned} \tag{4.11}$$

where $r_{\mathrm{ac}} + jx_{\mathrm{ac}}$ is the aggregated impedance of the converter and transformer impedances ($x_{\mathrm{ac}} = \omega_{\mathrm{ac}} l_{\mathrm{ac}}$, l_{ac} is the inductance), r_{ac} is the resistance; ω_{ac}, v_{ac}, i_{ac} and v_{t} are the frequency, AC grid voltage, AC side current and AC terminal voltage, respectively. The power balance between the AC and DC sides of the converter is given by:

$$p_{\mathrm{ac}} + v_{\mathrm{dc}} i_{\mathrm{dc}} - p_{\mathrm{loss}} - \frac{1}{2} c_{\mathrm{dc}} \frac{d(v_{\mathrm{dc}}^2)}{dt} = 0 \ , \tag{4.12}$$

where $p_{\mathrm{ac}} = (\frac{3}{2})(v_{\mathrm{ac},d} i_{\mathrm{ac},d} + v_{\mathrm{ac},q} i_{\mathrm{ac},q})$; $\frac{1}{2} c_{\mathrm{dc}} \frac{d(v_{\mathrm{dc}}^2)}{dt}$ is the energy variation in the capacitor; $p_{\mathrm{loss}} = (\frac{3}{2}) r_{\mathrm{ac}} i_{\mathrm{ac}}^2 + g_{\mathrm{sw}} v_{\mathrm{dc}}^2$ are the circuit and switching losses of the converter respectively, with $i_{\mathrm{ac}}^2 = i_{\mathrm{ac},d}^2 + i_{\mathrm{ac},q}^2$ and g_{sw} is obtained from a given constant conductance g_0 and the quadratic ratio of the actual current to the nominal one, as follows [82]:

$$g_{\mathrm{sw}} = g_0 \left(\frac{i_{\mathrm{dc}}}{i_{\mathrm{dc}}^{\mathrm{nom}}} \right)^2 \ . \tag{4.13}$$

In the equations above, AC quantities are expressed in the dq-reference frame, achieved through a Phase-Locked Loop (PLL). The PLL forces the angle of the dq-frame to track the angle θ_{ac}.

4.4.2 VSC Control

Figure 4.7 shows the vector-current control considered in this work. This control strategy uses a dq-composition with the grid voltage as phase reference, an inner current control loop to decouple the current into its d and q components. The reference currents for the inner control are achieved using an outer or high level controller loop.

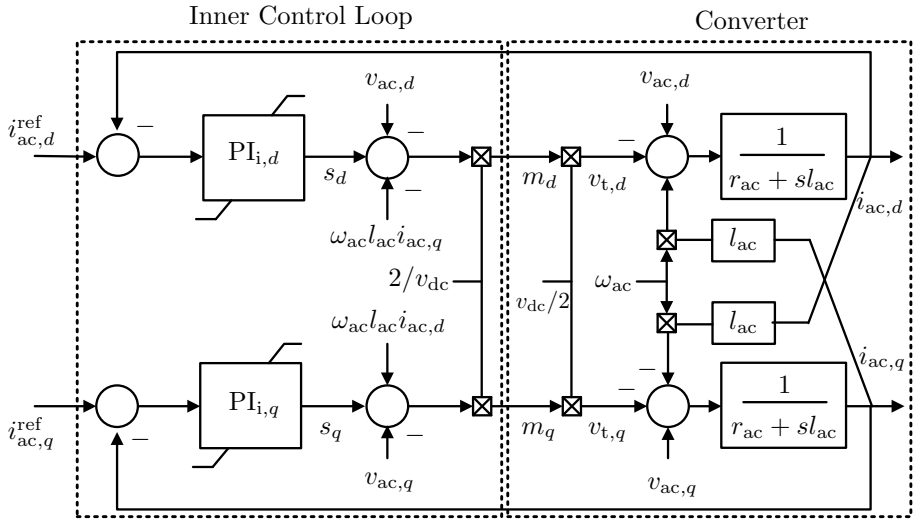

Figure 4.7: VSC converter and inner current control in dq-frame.

An outer control loop utilizes the d component to control active power or DC voltage, and the q component to control reactive power or AC voltage. Both inner and outer loops are implemented with PI controllers [19, 98]. Based on the current limiting method of the VSCs, the outer control loop can have a constant or variable limits. Figure 4.8 shows the possible configurations for the outer control loop. In this chapter only constant limits on PIs i.e. configuration [I] is considered and other types are discussed in Chapter 6.

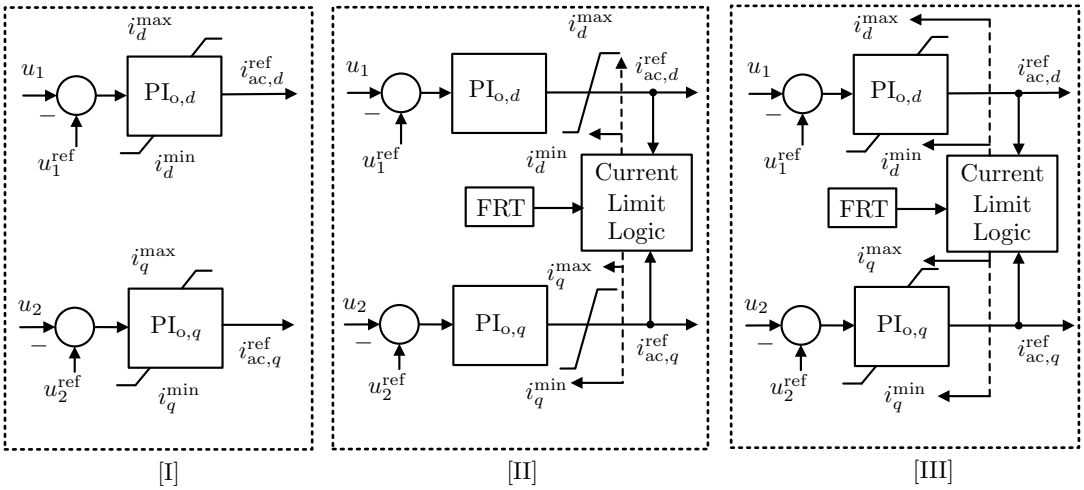

Figure 4.8: Outer control configurations: [I] constant limits; [II] variable limits with wind-up PIs and [III] variable limits with AW PIs.

4.4.3 Current Limiters

Active and reactive power transfer capabilities are always constrained in VSC-based devices. Violations of the operating limits can occur following a large disturbances such as a fault or a line outage. Protections strategies aim at recovering VSC currents to the pre-fault steady state. Depending on the power-electronic interface, commonly found protection mechanisms include [113]: (i) ac-side over-current limiting; (ii) modulation index limiting; (iii) reactive current boosting during faults; and (iv) fault-ride-through during ac faults.

The advantage of using the control structure described in Section 4.4.2 is that it can limit the current flowing into the converter during the disturbances. In the implemented model of the VSC, such current limitation strategy is achieved through the PI controllers and the current limiter of the outer loop. Current limit values are chosen based on the priority between active (p) power or DC voltage and reactive (q) power or AC voltage depending on the applications.

For configuration [I] in Figure 4.8, if the priority is given to the active power or DC voltage, $i_{\mathrm{ac},d}^{\mathrm{ref}}$ is limited to the maximum current capacity $\pm i_{\max}$ whereas $i_{\mathrm{ac},q}^{\mathrm{ref}}$ is limited in such a way that the total current does not exceed the maximum current rating of the converters [19], as follows:

$$\begin{aligned} i_d^{\max} &= i_{\max} \ , \\ i_q^{\max} &= \sqrt{i_{\max}^2 - i_{\mathrm{ac},d}^2} \ . \end{aligned} \tag{4.14}$$

4.4.4 Tuning of the Controller

The tuning of the PI controllers is carried out considering the closed-loop dynamic response of the system when the PI control is *not* limited. In practice, PI controllers are first designed without explicitly considering saturation constraints. Then an anti-windup limiter is applied to reduce the windup effect [16], [34]. Since the model of a non-saturated PI controller is unique, the first step will always result in same proportional and integral gain parameters for all the PI models considered in this Chapter.

The structure of the controllers for both d- and q-axis current control loops are identical and so are assumed to be their parameters. The gains for the PI controllers in the inner control are chosen based on the pole cancellation technique as follows [30],

$$k_p = \frac{l_{\mathrm{c}}}{\tau_c} \quad \text{and} \quad k_i = \frac{r_{\mathrm{c}}}{\tau_c} \ , \tag{4.15}$$

where l_{c} and r_{c} are the inductance and resistance respectively, τ_c is the desired time constant of the closed loop step response, the typical range of τ_c for VSC-based applications is $[0.5, 5]$ ms [11]. A trial-and-error technique is used for the tuning

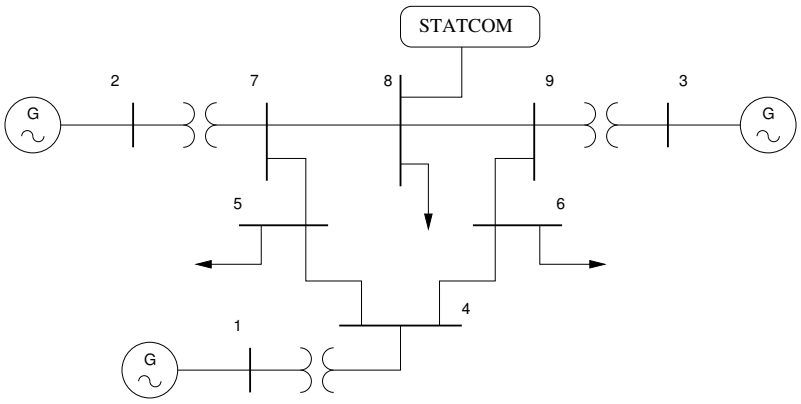

Figure 4.9: WSCC 9-bus test system with a VSC-based STATCOM connected at bus 8.

of the outer controllers and the back calculation gains for PI3 and PI4. However feedback gains in PI3 and PI4 can be tuned using other techniques, i.e., a Linear Matrix Inequality (LMI) technique such as the one discussed in [105].

4.5 Case Study I: WSCC 9-Bus System

The WSCC 9-bus test system (see Figure 4.9) with a VSC-based STATCOM, connected at bus 8 is used for time domain simulation. The test network consists of three synchronous machines, three two-winding transformers, three loads and six transmission lines. All generators are equipped with AVRs and TGs. The current limit is set by giving priority to reactive power. The STATCOM parameters are given in Table 4.1.

4.5.1 WSCC-9 Bus: Simulation Results

A three phase fault at bus 6 was simulated at $t = 1$ s and cleared after 80 ms through disconnecting the line that connects buses 6 and 9. This line is put

Table 4.1: VSC-based STATCOM parameters

Name	Values
Converter	$x_{\text{ac}} = 0.041$ pu, $r_{\text{ac}} = 0.003$ pu
Current Limits	$i_q^{\max} = 0.3$ pu, $i_q^{\min} = -0.23$ pu, $i_{\text{ac},d}^{\lim} = \pm 0.01$ pu
Outer Control	$k_p^{\text{o},q} = 5.5$, $k_p^{\text{o},d} = 50$, $k_i^{\text{o},q} = 45$, $k_i^{\text{o},d} = 25$
Inner Control	$k_p^{\text{i},q} = 0.2$, $k_p^{\text{i},d} = 0.2$, $k_i^{\text{i},q} = 20$, $k_i^{\text{i},d} = 20$

$k_p^{\text{o},q}, k_p^{\text{o},d}, k_i^{\text{o},q}, k_i^{\text{o},d}$ are the outer level q and d axis proportional and integral gains;
$k_p^{\text{i},q}, k_p^{\text{i},d}, k_i^{\text{i},q}, k_i^{\text{i},d}$ are the inner level q and d axis proportional and integral gains.

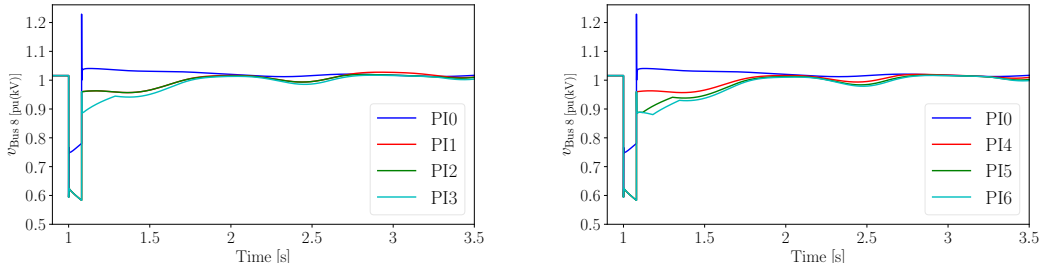

Figure 4.10: Response of the bus voltage $v_{\text{Bus 8}}$ of the WSCC 9-bus system: using PI0 - PI3 (left); using PI0 and PI4 - PI6 (right).

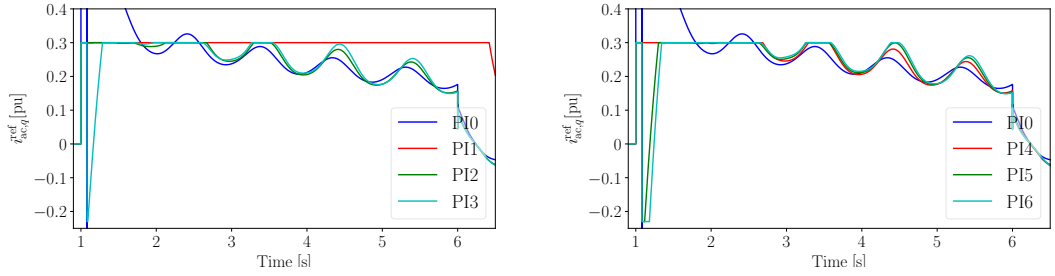

Figure 4.11: Response of the q-axis current reference of STATCOM ($i_{\text{ac},q}^{\text{ref}}$) in the WSCC 9-bus system: using using PI0 - PI3 (left); using PI0 and PI4 - PI6 (right).

back in service at $t = 6$ s. Simulation is carried out considering both the upper and lower current limits (see Table 4.1) of the PIs (PI0 - PI6) controlling AC and DC voltages. The trajectories of the voltage at bus 8 ($v_{\text{Bus 8}}$) and q-axis current reference ($i_{\text{ac},q}^{\text{ref}}$) are shown in Figures 4.10 and 4.11, respectively, for the different PI controller configurations.

The response of PI0 (no limits) is used as reference for the comparison. PI3 - PI6 provide fairly similar transient responses because they consider a feedback when the output hits the limit. The non-zero feedback signal drives the integrator in order to restore the output to within limit, therefore these models provide similar transient responses. For all the PI types the current reference converges to steady state, however the convergence rate is different. It is evident from Figures 4.10 and 4.11 that there is a considerable difference in the transient behavior when considering different anti-windup strategies (PI2 - PI6) because of difference in the response of the integrator state variable.

4.5.2 Effect of Feedback Gain of PI3 and PI4

The response of the WSCC 9-bus test system facing the same disturbance in previous Section using different k_s of the PI3 and PI4 are now studied. The trajectories of the bus voltage ($v_{\text{Bus 8}}$) and state variables of AC voltage controller are shown in Figure 4.12. It can be seen that there are differences in the trajectories due to the different values of the feedback gain parameter. To ensure a relatively fast response of the integrator, it is recommended to use a higher value of this feedback gain. Nevertheless a higher feedback gain does not ensure a better transient response (see Figures 4.12 - 4.13). So it is important to tune this parameter appropriately.

4.6 Case Study II: Irish System

This case study considers the all-island Irish transmission system connected through the VSC-HVDC link, namely, the East-West Interconnector (EWIC), to the

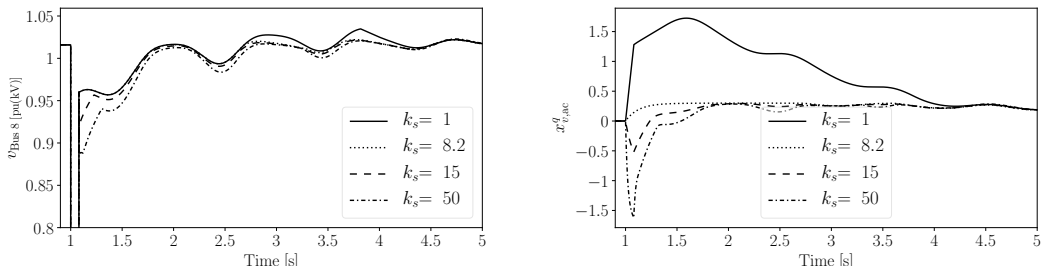

Figure 4.12: Response of the bus voltage $v_{\text{Bus 8}}$ of the WSCC 9-bus system using PI3 with different feedback gain.

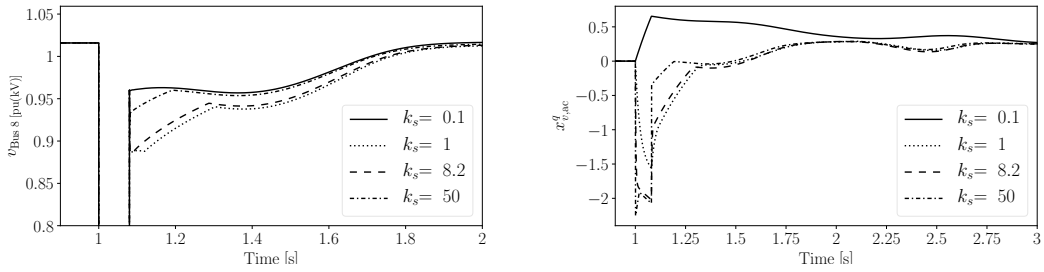

Figure 4.13: Response of the bus voltage $v_{\text{Bus 8}}$ of the WSCC 9-bus system using PI4 with different feedback gain.

GB grid. The Irish network is built based on the static data provided by the Irish transmission system operator, EirGrid Group, and the dynamic data defined based on power plant capacities and technologies [83]. The system consists of 1,479 buses, 1,851 transmission lines and transformers, 245 loads, 22 Synchronous Generators (SGs) with AVRs and TGs, 6 PSSs, 173 wind generators of which 139 are doubly-fed induction generators (DFIGs) and 34 with constant speed wind turbine. The GB grid is based on [20] and consists of 63 buses (29 high voltage buses, 33 generator buses, 1 HVDC link), 98 transmission lines, 30 synchronous generators with AVRs and TGs (28 thermal, 2 hydro), 3 DFIGs, 29 loads.

Table 4.2: HVDC link and cable parameters

Name	Parameter
Rating	500 MW
DC voltage	±200 kV
AC voltage	400 kV
Cable (each)	$r = 3.7\ \Omega$, $l = 0.0365$ mH
Converter	$r_{\text{ac}} = 1^{-3}$ pu, $x_{\text{ac}} = 1.3^{-3}$ pu, $c_{\text{dc}} = 93.6\ \mu$F, $g_{\text{sw}} = 7^{-5}$ pu

4.6.1 VSC-HVDC Link: Simulation Results

The initial operating condition assumes that 450 MW are imported from the GB system to the Irish grid through the EWIC, which is modeled as a symmetric monopole-type VSC as described in [44] and parameters used are listed in Table 4.2. In nominal conditions, the VSC on Irish side to be acting as inverter (DC to AC) and the VSC at GB side is acting as rectifier (AC to DC). The VSC controller limits on both sides of the EWIC are imposed based on converter rating and priority is given to active power.

The contingency consists of a three phase fault occurring at 0.2 s, cleared after 60 ms and located near to VSC on the Irish side of the EWIC. During the fault, both the AC voltage and active power controllers of the VSC on the Irish side reach their limits. The responses of the outer controller state variables, outputs and reactive powers provided by the VSC for different PI controllers are shown in Figures 4.14-4.18. The response of model PI0 is included for reference to show the behavior of the system when no limits are included. Simulation results clearly show that different PI limiter models lead to considerably different transient behaviors. Relevant remarks on each PI model are given below.

The windup limiter of PI1 does not lock the integral variable x when the limits are

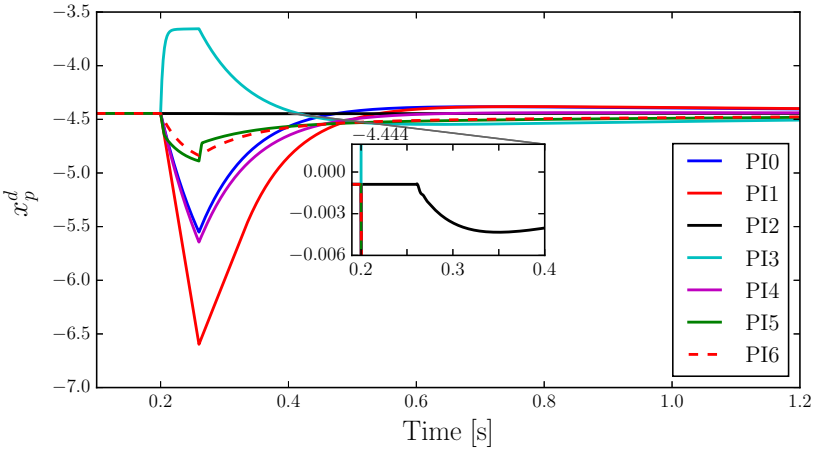

Figure 4.14: Response of the integrator state variable (x_p^d) of the active power controller of the Irish-side VSC.

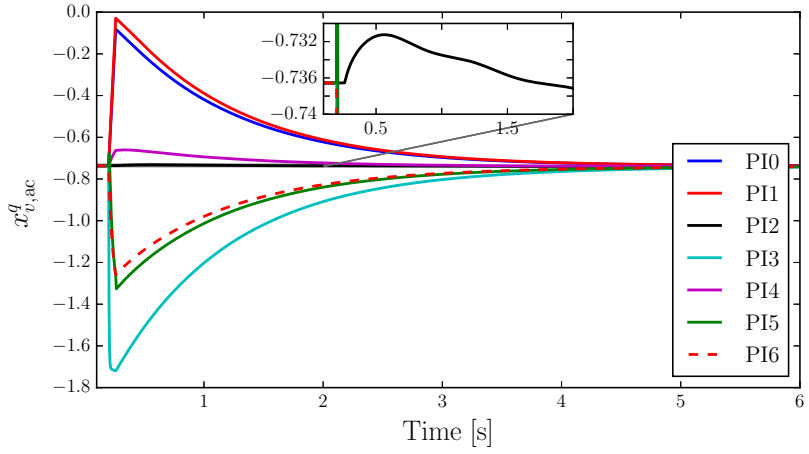

Figure 4.15: Response of the integrator state ($x_{v,\mathrm{ac}}^q$) of the AC voltage controller of the Irish-side VSC.

binding, which results in a slower recovery to the control mode after the disturbance. This poor performance is typical of windup limiters, which are thus not to be recommended.

The AW limiter of model PI2 locks the integrator state variable as soon as the PI limits are binding as shown in the zoom in Figures 4.14 and 4.15. The response of model PI2 is thus faster than that of all other PI models.

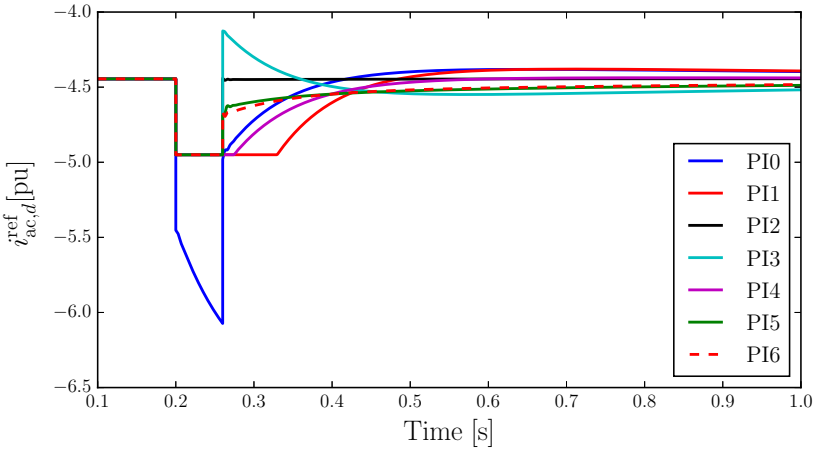

Figure 4.16: Response of the output of the active power controller of the Irish-side VSC.

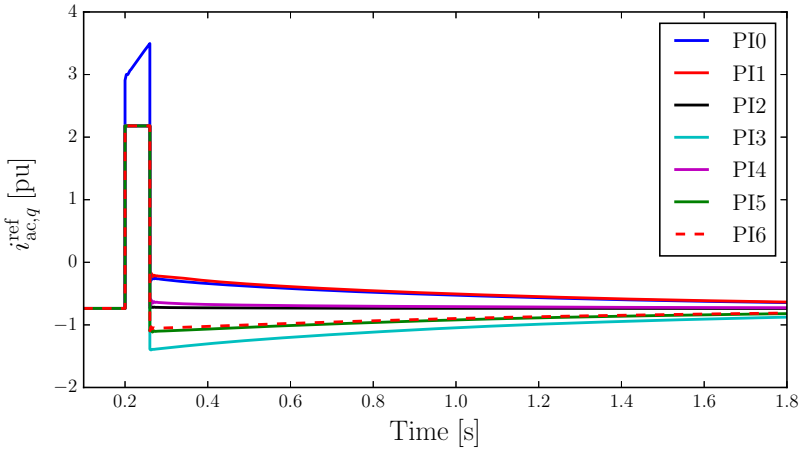

Figure 4.17: Response of the output of the AC voltage controller of the Irish-side VSC.

For the back calculation models PI3 to PI6, the integral term of the controller is recomputed through a feedback signal and reset to a new value so that it prevents the integrator from winding up.

As the disturbance lasts 60 ms and is cleared before the integrator settles to a new value (see Figures 4.14-4.15), back calculation methods show different responses (see Figures 4.16-4.17) compared to model PI2, also with respect to the active and reactive power supports (the trajectory of the reactive power is shown in Figure

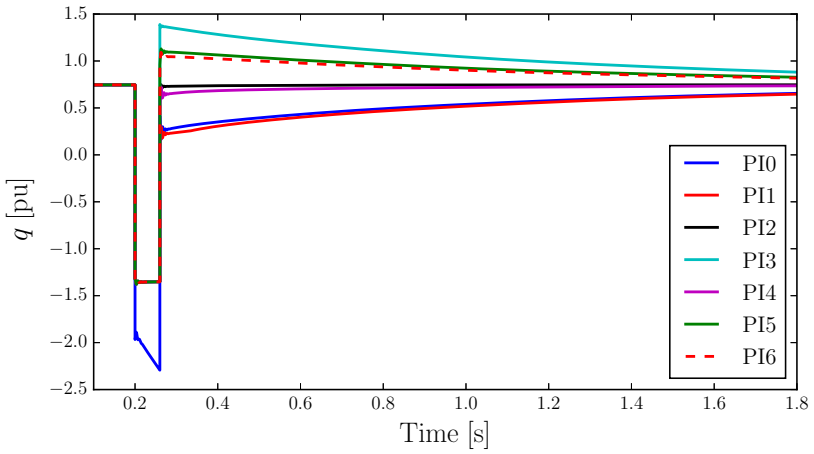

Figure 4.18: Response of the reactive power support of the Irish-side VSC.

4.18).

Finally, both models PI3 and PI4 include a feedback gain. If same gain values are used, due to their different implementations, namely (4.4) and (4.5), the two models show a different behavior. Special care, thus, has to be taken when tuning these models and/or switching among PI models.

4.7 Case Study III: Nodic-32 System

The Nordic system presented in Section 3.5.2 is used with a VSC-based STATCOM. The STATCOM is connected to the Nordic test system at bus 1044. Thus the current limits of the VSC device are set in such a way that priority is given to the q-axis component.

4.7.1 STATCOM: Comparison of Alternative Solutions of IEEE Standard

The comparison discussed in this section considers the dynamic response of the PI controllers following a three-phase fault at bus 4044, occurring at $t = 1$ s and cleared at $t = 1.06$ s. Two scenarios are studied: (a) the fault is cleared by opening the line between bus 4044-4032 at $t = 1.06$ s, then the line is re-closed at $t = 5$ s; and (b) the fault is cleared at $t = 1.06$ s without opening any line.

In both scenarios, the conventional implementation of model PI2 shows the numerical issues discussed in Section 4.3.2. Using other integration methods, i.e., second order BDF and implicit backward Euler, and reducing the time step or changing to adaptive step size do not remove the deadlock problem. This allows comparing the performance of methods S1 and S2, discussed in Section 4.3.2. The conventional PI2 model leads to a deadlock at $t = 1.605$ s (see the vertical line in Figure 4.19). Model PI2-S1 with a DB of 0.002 allows completing the simulation. For model PI2-S2, which never shows the deadlock issue, the integrator is limited to the same values as the current reference limits.

Figures 4.19 and 4.20 show the trajectories of the q-axis current reference of the VSC outer control and its corresponding state ($x^q_{v,\mathrm{ac}}$) with the input ($u_{v,\mathrm{ac}} = v^{\mathrm{ref}}_{\mathrm{ac}} - v_{\mathrm{ac}}$) for both contingencies respectively. Figure 4.20 also shows the reactive power provided by the STATCOM.

While model PI2-S1 avoids the deadlock phenomenon, its transient response depends on the magnitude of the DB and the severity of the contingency. If the DB is too small or the contingency is too severe, the deadlock can occur again. Model

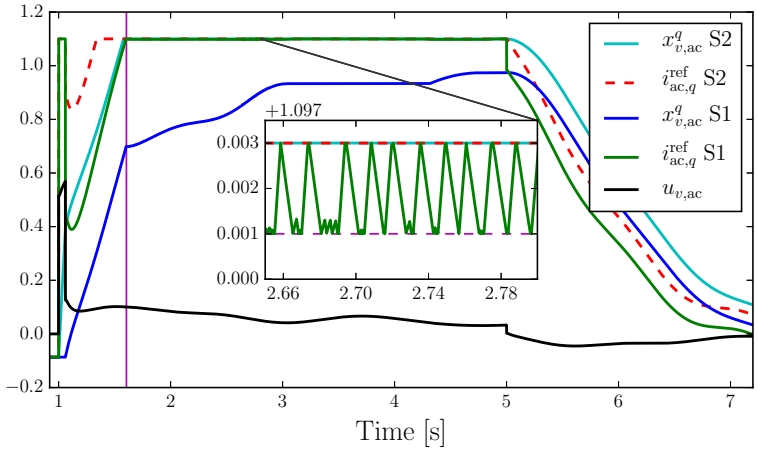

Figure 4.19: Scenario (a): Response of the AC voltage controller of the outer level of the STATCOM, using models PI2-S1 and PI2-S2.

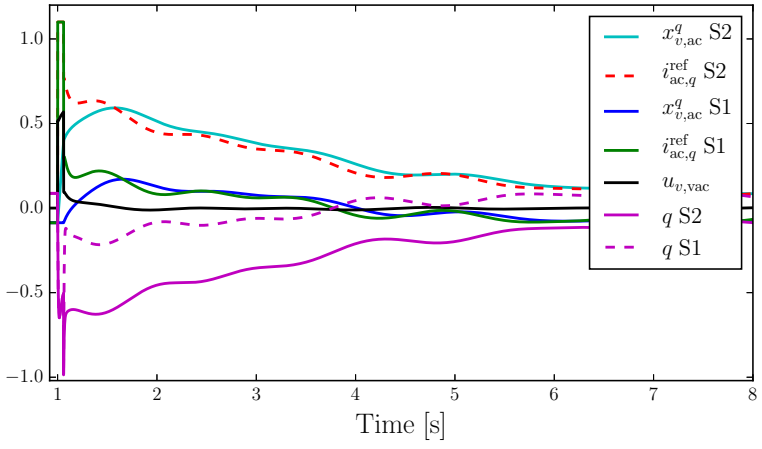

Figure 4.20: Scenario (b): Response of the AC voltage controller of the outer level and reactive power support provided by the STATCOM, using models PI2-S1 and PI2-S2.

PI2-S2 never shows the trajectory deadlock but can lead to significant differences in the transient response and final steady-state conditions because the integrator state is not locked unless it hits a limit (see Figure 4.20). Unfortunately, the exact values of such limits for integrator state are often unknown. Typically, same limits as the algebraic PI output are used, but this is not necessarily the best approach as the state variable can wind up independently (and inconsistently) with respect to the

output of the PI.

4.7.2 STATCOM: Comparison of all PI models

Figures 4.21 and 4.22 show the reactive power response of models PI0 to PI6 using the scenarios (a) and (b) described in Section 4.7.1. DB=0.002 is used for model PI2-S1.

Compared to previous case study, the impact of PI model differences on the transient response is more significant. In particular, Figure 4.21 shows that the response of models PI0 and PI1 are not acceptable.

Back calculation models PI3 and PI4 leads the STATCOM to absorb reactive power whereas model PI2-S1 leads to the opposite behavior, at least for a few seconds. This mixed response can be changed by reducing the feedback gain value. However a high feedback gain value is recommended to reset the integrator quickly [16, 59]. Tracking methods with delay and the combined type (models PI5 and PI6) show better transient response than the other PI types considered in this case study.

4.8 Discussion on Simulation Results

PI models with AW limiters are to be preferred to windup ones due to their faster transient response. However, since there are several ways to implement AW limiters, it is difficult to anticipate the response of each PI model. Results depend not only on the PI model itself, but also on the severity of the disturbance, the PI parameters, network configuration and initial operating point.

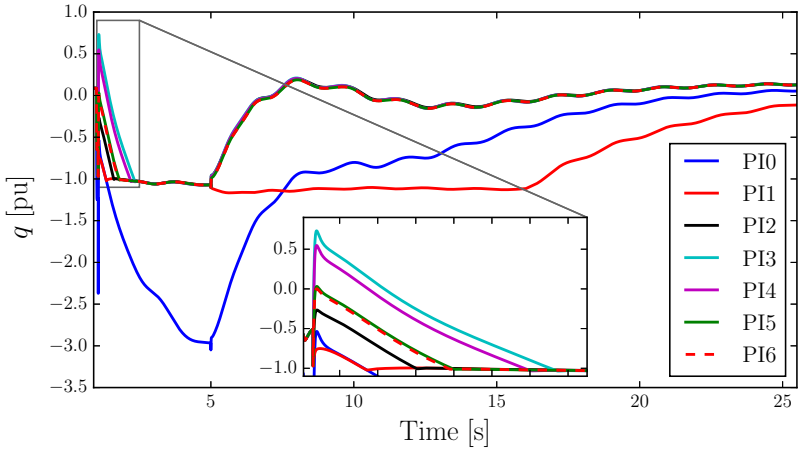

Figure 4.21: Scenario (a): reactive power support from STATCOM, using models PI0 to PI6.

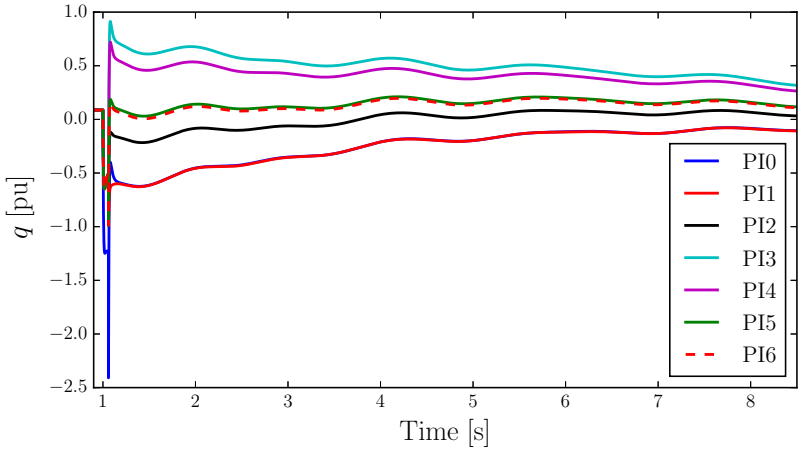

Figure 4.22: Scenario (b): reactive power support from STATCOM, using models PI0 to PI6.

For the IEEE PI model (PI2), a deadband (or hysteresis) or other numerical solutions can be required to avoid trajectory deadlock. This raises a variety of implementation issues. An early reference [15] suggests that this problem is not only a software issue due to the discretization of the integration scheme and that it can affect also the physical digital controller. However, in practice, the input quantities to the controller will eventually change and possibly unlock the device. On the other

hand, in simulations, the deadlock prevents the integration scheme to converge and is thus critical to identify and/or avoid it with adequate software implementation "tricks." It is worth mentioning that PI2 is also tested in Modelica based software tool OpenModelica [5] and Dymola [1] where solvers are strictly separated from models. Solvers in OpenModelica and Dymola also show same numerical chattering issue as DOME shows. This will be further discussed in the next Chapter.

Compared to the other AW types, model PI2 provides a better transient response, namely, fast convergence to post disturbance equilibrium, as well as low over- and under-shoot. It is also worth noticing that the deadlock issue does not occur if $k_p = 0$.

The main advantage of back calculation models PI3 to PI6 is that they intrinsically avoid the deadlock. There is also no difference in the response of the hardware and software implementations of these models. But they have other issues. Since the state variable of the integrator is never really locked, their time response is slower, which can deteriorate the overall performance of the VSC controllers. Then models PI3 to PI5 require tuning an extra parameter, and model PI6 is intrinsically complex due to the mix of continuous and discrete variables and logical operations. Tuning the back calculation gain or delay requires particular care because of their significant impact on the overall PI dynamic behavior.

The test systems considered in this Chapter are dominated by conventional synchronous generation and, hence, the dynamics of electronic converters have a smaller impact on the overall system. For high-dimensional nonlinear sets of differential-algebraic equations often the results can not be generalized. The best that can be done is to show possible issues and discuss why these issues appear. Based on the results of this Chapter, it is fair to conclude that the models of

the limiters of the PI controllers can vary significantly the behavior of the VSC controllers, and, if the penetration of such devices is high, also that of the overall grid.

4.8.1 Remarks and Recommendations

According to the literature, the most commonly used anti-windup method on a PI controller is the back calculation. Despite being a standard, the model described in the IEEE standard 421.5-2016 is less common and among all considered models, the IEEE standard, in fact, is the most complex as it requires to introduce a fictitious deadband to work properly. Models PI3 and PI4, on the other hand, are the simplest models.

- **Dynamic Performance:**

  For small disturbances, e.g., load variations and line outages without faults, all PI models show very similar transient response, even if they saturate. This has to be expected as, for light disturbances, the differences in state variable between the PI models that lock their internal state variable (IEEE standard) and those that do not (back calculation, PI3-PI6) is small. So in this cases, models PI3 to PI6 are to be preferred as they do not create numerical issues.

  On the other hand, significant differences of the dynamic response of the PI models are observed for large disturbances, e.g., faults and large generator outages. In these cases, the dynamic response of the IEEE standard PI model is the best choice as it locks the PI internal state variable and reduce the delay of the operation of the controller when the input signal is back to normal.

- **Best practice:**

For dynamic analysis of real-world power system networks the best practice is to carefully model PI controllers according to the actual hardware and specifications provided by the vendors of the VSC devices. If the real implementation is unknown, the choice becomes a trade-off between dynamic performance and implementation complexity. Whenever priority is the performance following a large disturbance, IEEE standard (PI2) is recommended. To avoid trajectory deadlock a deadband should be considered in the implementation. In order to avoid implementation complexity a back calculation method is preferred. In particular, the model PI4 is recommended and if a trial and error tuning technique is preferred to avoid complex tuning techniques, a convenient initial guess of the back calculation gain is $k_s \approx (1/t_i)$, where $t_i = \frac{k_p}{k_i}$, is the integral time constant [14].

4.9 Conclusions

The Chapter shows that different implementations of PI control limiters result in significantly different transient responses of interconnected power systems. Among the considered implementations of the anti-windup types, three main groups based on their characteristic features: (i) conditional integration (PI2); (ii) feedback-type integrators (PI3 - PI5) and (iii) combined conditional and feedback-type integrators (PI6) are identified. Furthermore it reviews and compares the dynamic behavior of VSC-HVDC links and STATCOM device considering different PI controller models with windup and anti-windup limiters. Simulation results indicate that anti-windup limiters are to be preferred but their implementation and design require particular care. The PI model based on the IEEE Standard 421.5-2016 shows the fastest

dynamic response but also the most critical implementation, which can lead to numerical issues.

Due to the world-wide trend to increase the penetration of VSC-based generation, it appears more and more important to pay attention to modeling aspects, such as PI limiters, that in the past have been often overlooked. The Chapter also distinguishes between modeling and solver issues to serve the practitioners who deals with power system dynamic analysis and software implementation.

5 Applications of Filippov Theory

5.1 Introduction

Filippov theory (FT) generalizes the discontinuities on the first-order ordinary differential equations and provides proper switching conditions. Moreover, if the solution enters into a constrained subset of the state space, typically known as sliding, the formalism given by Filippov [49] allows defining a vector field on the sliding surface to properly handle discontinuities. This theory has been applied in other fields, e.g., in power electronics [53]; and energy harvesters [55] to study sliding bifurcations. However, attempts to apply the FT to power system dynamic analysis have not been conducted thus far. In this work the focus is on the smooth continuation of trajectories during numerical simulation.

While effective, the FT-based approach poses several challenges, especially with respect to the numerical integration of DAEs. The main challenge is the definition of the analytical conditions and, thereafter, the implementation of a robust algorithm to automatically switch between different discontinuous states through capturing accurate non smooth dynamics [24, 40].

This Chapter discusses in details the deadlock behavior that prevents the numerical integration of trajectories related to IEEE Std. AW PI controller. Then the proof of concept of the application of FT on the IEEE Std. AW PI model is given.

After that a general purpose hybrid model for software implementation of Filippov system models is proposed. Finally the effectiveness of the generalized design is discussed using one mechanical system model and the IEEE Std. AW PI model.

The deadlock of numerical integration techniques related to the IEEE Std. AW model is presented in Section 5.2. Section 5.3 briefly discusses Filippov theory and Section 5.4 shows how FT effectively removes the deadlock by smoothing the trajectory using two examples: an illustrative example and a simple single machine power system network. Section 5.5 presents the generalized FT based hybrid model and its software implementation. Numerical validation of the generalized design is presented in Section 5.6 and Section 5.7 using two applications namely, a relay feedback model and the IEEE Std. AW PI model, respectively using the Modelica language as well as the power system software tool DOME. Finally, Section 5.8 draws conclusions.

5.2 Numerical Integration

This section describes the numerical issues intrinsic of the IEEE AW PI model considering three commonly used numerical integration techniques, namely Backward and Forward Euler and Trapezoidal. An in depth analysis in the context of exclusive numerical integration approaches: explicit partitioned method, execution-list based method, and implicit trapezoidal method also given in [33].

Let us assume that at the beginning of the simulation, the input to the PI controller has an initial integrating state (INT) that is within the controller limits (see Figure 4.3) and that such an input the output reaches its maximum limit at t_1.

Then, at t_1, one has:

$$x_{t_1} + k_p u_{t_1} = w_{\max} \ , \tag{5.1}$$

where x_{t_1} and u_{t_1} are the values of the integrator state variable and input, respectively, at t_1. Now, let us assume that the condition to switch back to the INT state are satisfied at t_2, as follows:

$$y < w_{\max} \ . \tag{5.2}$$

While the state is in the maximum state (MAX), the value x_{t_1} is constant and u_{t_2} is the input at t_2. Thus, re-writing (5.2):

$$x_{t_1} + k_p u_{t_2} < w_{\max} \ \Rightarrow \ u_{t_2} < \frac{w_{\max} - x_{t_1}}{k_p} = u_{t_1} \ , \tag{5.3}$$

considering $k_p > 0$, if the input u_{t_2} becomes lower than u_{t_1} i.e. condition (5.3) is fullfilled then a transition from the MAX state to the INT state will happen. Assuming at t_2 the input u_{t_2} decreases from u_{t_1} at an integration step and $\Delta u = u_{t_2} - u_{t_1} < 0$. Depending on the integration method, and the step size h, the change in state variable $\Delta x = x_{t_2} - x_{t_1}$, can be obtained as:

- Backward Euler: $\Delta x = h\dot{x}_{t_2} = k_i h u_{t_2}$,
- Forward Euler: $\Delta x = h\dot{x}_{t_{2-1}} = k_i h u_{t_1}$,
- Trapezoidal: $\Delta x = \frac{h}{2}(\dot{x}_{t_{2-1}} + \dot{x}_{t_2}) = k_i \frac{h}{2}(u_{t_1} + u_{t_2})$.

Assuming $k_i > 0$ and $u_{t_2} > 0$, then $\Delta x > 0$. For a feasible transition from the MAX to the INT state at the end of the integration step, $y < w_{\max}$ must hold i.e.

$$\Delta x + k_p \Delta u < 0 \ , \tag{5.4}$$

using the values of Δx and Δu into (5.4) for the Backward Euler integration method, one has:

$$\begin{aligned} k_i h u_{t_2} + k_p(u_{t_2} - u_{t_1}) < 0 \ , \\ \Rightarrow \ \frac{u_{t_2}}{u_{t_1}} < \frac{1}{1 + \frac{k_i h}{k_p}} \ . \end{aligned} \tag{5.5}$$

Similarly for the Forward Euler and Trapezoidal method, one has:

$$\frac{u_{t_2}}{u_{t_1}} < 1 - \frac{k_i h}{k_p}, \ \frac{u_{t_2}}{u_{t_1}} < \frac{k_p - \frac{h}{2} k_i}{k_p + \frac{h}{2} k_i} \ . \tag{5.6}$$

The conditions (5.5)-(5.6) need to be satisfied to switch from the MAX to the INT region. Otherwise a deadlock situation arises. The deadlock consists in an infinite loop where the state variables switch between the MAX and INT states. For implicit integration schemes, the deadlock also prevents the solver to converge at a given time step and thus the simulation gets stuck. Note that the conditions (5.5)-(5.6) depend on the integration step-size h, gain values and current value of the input. The deadlock originates due to the time discretization of the numerical integration scheme. For $h \to 0$, in fact, the conditions (5.5)-(5.6) are always satisfied and the deadlock does not occur.

5.3 Filippov Theory

Filippov systems form a subclass of discontinuous dynamical systems which can be described by a set of first-order ordinary differential equations (ODEs) with a discontinuous right-hand side [49]. Consider the following switched dynamical

system:

$$\dot{\boldsymbol{x}} = \boldsymbol{f}(\boldsymbol{x}) = \begin{cases} \boldsymbol{f_1}(\boldsymbol{x}) & \text{when } h(\boldsymbol{x}) < 0 \\ \boldsymbol{f_2}(\boldsymbol{x}) & \text{when } h(\boldsymbol{x}) > 0 \end{cases} \tag{5.7}$$

where, the event function $h : \mathbb{R}^n \to \mathbb{R}$ and an initial condition $\boldsymbol{x}(t_0) = \boldsymbol{x_0}$ are known.

The state space $\mathbb{R}^n$ is split into two regions R_1 and R_2 separated by a hypersurface Σ where R_1, R_2 and Σ are characterized as (see Figure 5.1),

$$\begin{aligned} R_1 &= \{\boldsymbol{x} \in \mathbb{R}^n \mid h(\boldsymbol{x}) < 0\}, \\ R_2 &= \{\boldsymbol{x} \in \mathbb{R}^n \mid h(\boldsymbol{x}) > 0\}, \\ \Sigma &= \{\boldsymbol{x} \in \mathbb{R}^n \mid h(\boldsymbol{x}) = 0\}, \end{aligned} \tag{5.8}$$

such that $\mathbb{R}^n = R_1 \cup \Sigma \cup R_2$, assuming that the gradient of h at $\boldsymbol{x} \in \Sigma$ never vanishes, $\boldsymbol{h_x}(\boldsymbol{x}) \neq \boldsymbol{0}$ for all $\boldsymbol{x} \in \Sigma$.

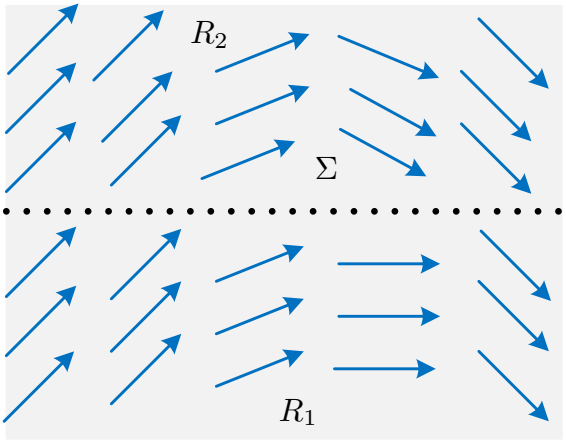

Figure 5.1: The state space with two regions divided by a hyperspace.

The vector field on Σ is defined by Filippov continuation approach, known as *Filippov convex method* [49]. This method states that the vector field on the surface of discontinuity is a convex combination of the two vector fields in the different

regions of the state-space:

$$\dot{\boldsymbol{x}} = \boldsymbol{f}(\boldsymbol{x}) = \begin{cases} \boldsymbol{f_1}(\boldsymbol{x}), & \boldsymbol{x} \in R_1 \\ \overline{co}\{\boldsymbol{f_1}(\boldsymbol{x}), \boldsymbol{f_2}(\boldsymbol{x})\}, & \boldsymbol{x} \in \Sigma \\ \boldsymbol{f_2}(\boldsymbol{x}), & \boldsymbol{x} \in R_2 \end{cases} \tag{5.9}$$

where, $\overline{co}(\boldsymbol{f_1}, \boldsymbol{f_2})$ is the minimal closed convex set containing $\boldsymbol{f_1}$ and $\boldsymbol{f_2}$, i.e.

$$\overline{co}\{\boldsymbol{f_1}, \boldsymbol{f_2}\} = \{\boldsymbol{f}_F : \boldsymbol{x} \in \mathbb{R}^n \to \mathbb{R}^n : \boldsymbol{f}_F = (1-\alpha)\boldsymbol{f}_1 + \alpha \boldsymbol{f}_2\}, \tag{5.10}$$

where $\alpha \in [0, 1]$.

Definition 1: An absolutely continuous function $\boldsymbol{x} : [\boldsymbol{0}, \boldsymbol{\tau}] \to \mathbb{R}^n$ is said to be a solution of (5.7) in the sense of Filippov, if for almost all $t \in [\boldsymbol{0}, \boldsymbol{\tau}]$ it holds that

$$\dot{\boldsymbol{x}} \in \boldsymbol{F}(\boldsymbol{x}(t))$$

where $\boldsymbol{F}(\boldsymbol{x}(t))$ is close convex hull in (5.10).

Now, the question is what happens when the trajectory of $\dot{\boldsymbol{x}} = \boldsymbol{f_1}(\boldsymbol{x})$, with $\boldsymbol{x}(\boldsymbol{0}) = \boldsymbol{x_0}$ reaches at Σ in finite time. The possibilities are: (a) transversal crossing, (b) attractive sliding or repulsive sliding and (c) smooth exit. Filippov formulated a first order theory to decide what to do in such situations. This theory is outlined below.

5.3.1 Filippov First Order Theory

Filippov first order theory defines the vector field if the solution approaches the discontinuous surface. Let $\boldsymbol{x} \in \Sigma$ and $\boldsymbol{n(x)}$ is the unit normal to Σ at $\boldsymbol{x}$ i.e. $\boldsymbol{n(x)} = \frac{\boldsymbol{h_x(x)}}{\|\boldsymbol{h_x(x)}\|}$ where, $\boldsymbol{h_x(x)} = \nabla h(\boldsymbol{x})$ and $\nabla = \frac{\partial}{\partial \boldsymbol{x}}$; the components of $\boldsymbol{f_1(x)}$ and $\boldsymbol{f_2(x)}$ onto the normal to the Σ are $\boldsymbol{n}^T\boldsymbol{(x)f_1(x)}$ and $\boldsymbol{n}^T\boldsymbol{(x)f_2(x)}$ respectively.

- **Transversal Crossing:** If at $\boldsymbol{x} \in \Sigma$,

$$(\boldsymbol{n}^T\boldsymbol{(x)f_1(x)}).(\boldsymbol{n}^T\boldsymbol{(x)f_2(x)}) > 0, \tag{5.11}$$

the trajectory leaves Σ, and two cases are possible. The system will move to R_2 with $\boldsymbol{f} = \boldsymbol{f_2}$, if $\boldsymbol{n}^T\boldsymbol{(x)f_1(x)} > 0$ (see Figure 5.2[I]) or it will enter to R_1 with $\boldsymbol{f} = \boldsymbol{f_1}$, if $\boldsymbol{n}^T\boldsymbol{(x)f_1(x)} < 0$.

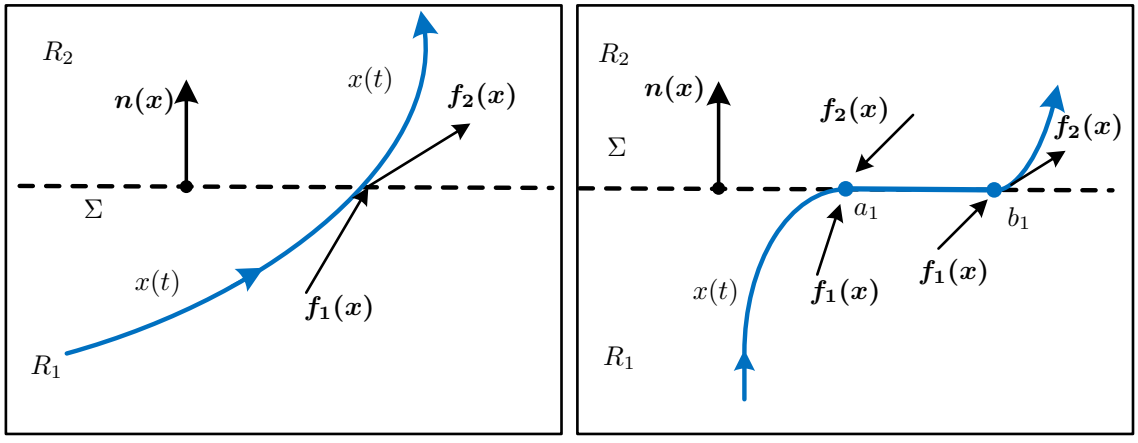

Figure 5.2: Different regions of the state space with [I] transversal and [II] sliding trajectory.

- **Sliding mode:** Sliding occurs, at $\boldsymbol{x} \in \Sigma$ if,

$$(\boldsymbol{n}^T(\boldsymbol{x})\boldsymbol{f_1}(\boldsymbol{x})).(\boldsymbol{n}^T(\boldsymbol{x})\boldsymbol{f_2}(\boldsymbol{x})) < 0 \ . \tag{5.12}$$

The sliding mode can be an attracting or a repulsive one. An attracting sliding mode will occur if (see a_1 in Figure 5.2[II]),

$$(\boldsymbol{n}^T(\boldsymbol{x})\boldsymbol{f_1}(\boldsymbol{x})) > 0 \quad \text{and} \quad (\boldsymbol{n}^T(\boldsymbol{x})\boldsymbol{f_2}(\boldsymbol{x})) < 0, \ \boldsymbol{x} \in \Sigma. \tag{5.13}$$

While sliding along Σ, time derivative $\boldsymbol{f}_F$ is given by:

$$\boldsymbol{f}_F(\boldsymbol{x}) = (1 - \alpha(\boldsymbol{x}))\boldsymbol{f_1}(\boldsymbol{x}) + \alpha(\boldsymbol{x})\boldsymbol{f_2}(\boldsymbol{x}), \tag{5.14}$$

where, $\alpha(\boldsymbol{x})$ is given by [proof, see [49]]:

$$\alpha(\boldsymbol{x}) = \frac{\boldsymbol{n}^T(\boldsymbol{x})\boldsymbol{f_1}(\boldsymbol{x})}{\boldsymbol{n}^T(\boldsymbol{x})(\boldsymbol{f_1}(\boldsymbol{x}) - \boldsymbol{f_2}(\boldsymbol{x}))} \ . \tag{5.15}$$

The sliding mode continues until one of the vector fields starts to point away.

- **Exit conditions:**

If, while in sliding mode, one of the vector fields drifts away, the solution continues above or below the sliding surface (see b_1 in Figure 5.2[II]). The exit point is calculated by finding either the root $\alpha(x) = 0$ or $\alpha(x) = 1$ as appropriate.

The following remarks are relevant:

– *If* $\boldsymbol{f}_F(\boldsymbol{x}) \neq \boldsymbol{f_1}(\boldsymbol{x})$, $\boldsymbol{f}_F(\boldsymbol{x}) \neq \boldsymbol{f_2}(\boldsymbol{x})$ *such a solution is often called a sliding motion.*

– A solution having an attractive sliding mode exists and is unique, in forward time.

– If at the point of discontinuity, condition (5.12) becomes ≤ 0 and $\boldsymbol{f_1(x)} \neq \boldsymbol{f_2(x)}$ then a continuous vector-valued function $\boldsymbol{f}_F(\boldsymbol{x})$ is given which determines the velocity of motion $\dot{\boldsymbol{x}} = \boldsymbol{f}_F(\boldsymbol{x})$ along the discontinuity line. If $\boldsymbol{n}^T(\boldsymbol{x})\boldsymbol{f_1(x)} = 0$ then $\boldsymbol{f}_F(\boldsymbol{x}) = \boldsymbol{f_1(x)}$; if $\boldsymbol{n}^T(\boldsymbol{x})\boldsymbol{f_2(x)} = 0$ then $\boldsymbol{f}_F(\boldsymbol{x}) = \boldsymbol{f_2(x)}$.

If the signs are opposite in (5.13) the sliding mode is called *repulsive* and does not generally have a unique solution. For this reason, the repulsive sliding mode is not considered in this work.

5.4 Illustrative Examples

In order to demonstrate the application of Filippov theory on IEEE AW PI controller two illustrative case studies are considered. The first case study is similar to the example discussed in Section 4.3.2 and the second one considers an SMIB power system network used in Section 2.3.3. The algorithm described in [93] is applied for numerical simulation. These results are achieved using simulation tool Matlab [4]. Furthermore the results are compared with DB (S1) and LIT (S2) based techniques discussed in Section 4.3.2.

5.4.1 Example I

Let the following signal be the input signal to the IEEE AW PI controller:

$$\begin{aligned} &\text{if } t < 3 \text{ then: } \dot{u} = 1 \ , \\ &\text{else: } \dot{u} = -1 \ , \end{aligned} \tag{5.16}$$

and the parameters considered are, $k_i = 3$, $k_p = 1$, $w_{\max} = 1.2$, $w_{\min} = -1.2$ and the initial values at $t = 0$ are $x_0 = 0.5$, and $u_0 = 0$. The mathematical model for upper limit becomes:

$$\dot{\boldsymbol{x}} = \boldsymbol{f}(\boldsymbol{x}) = \begin{cases} \boldsymbol{f_1}(\boldsymbol{x}) = \boldsymbol{f_{ns}} = \begin{bmatrix} \dot{u} \\ k_i x_1 \end{bmatrix} & \text{when } h(\boldsymbol{x}) < 0 \ , \\ \boldsymbol{f_2}(\boldsymbol{x}) = \boldsymbol{f_s} = \begin{bmatrix} \dot{u} \\ 0 \end{bmatrix} & \text{when } h(\boldsymbol{x}) > 0 \ , \end{cases}$$

where $\boldsymbol{f_{ns}}$ and $\boldsymbol{f_s}$ are the differential equations when the controller is not saturated and saturated, respectively and u varies according to (5.16). The controller output signal $y = k_p x_1 + x_2$. The switching manifold is given by: $h(\boldsymbol{x}) = y - 1.2$. So, $\boldsymbol{h_x}(\boldsymbol{x}) = [\frac{\partial h(\boldsymbol{x})}{\partial x_1} \quad \frac{\partial h(\boldsymbol{x})}{\partial x_2}]^T = [k_p \quad 1]^T$, and the normal to the switching surface is: $\boldsymbol{n}^T(\boldsymbol{x}) = [k_p \quad 1]$.

The simulation results are shown in Figure 5.3 and how FT is applied at each discontinuous point described below.

- $t = 0$ (s): With initial conditions $[0; 0.5]$, $h(\boldsymbol{x}) < 0$, thus the system starts in the non-saturated region and is modeled with $\boldsymbol{f} = \boldsymbol{f_{ns}}$.

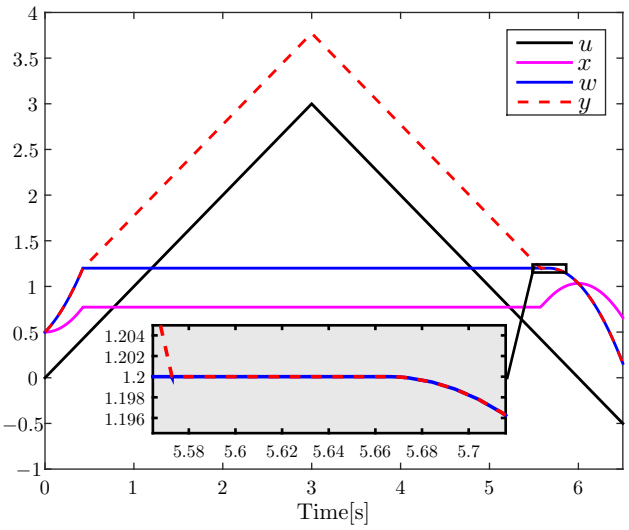

Figure 5.3: Response of trajectories using Filippov theory.

- $t = 0.4268$ (s): The system has struck the switching manifold i.e. $h(\boldsymbol{x}) = 0$ with $u = 0.4268$. At the switching surface, calculating,

$$\boldsymbol{n}^T(\boldsymbol{x})\boldsymbol{f_1}(\boldsymbol{x}) = [1 \quad 1] \begin{bmatrix} 1 \\ \\ 3(0.4268) \end{bmatrix} = 2.2804 \ ,$$

$$\boldsymbol{n}^T(\boldsymbol{x})\boldsymbol{f_2}(\boldsymbol{x}) = [1 \quad 1] \begin{bmatrix} 1 \\ \\ 0 \end{bmatrix} = 1 \ .$$

  The system undergoes a transversal intersection since $[\boldsymbol{n}^T(\boldsymbol{x})\boldsymbol{f_1}(\boldsymbol{x})].[\boldsymbol{n}^T(\boldsymbol{x})\boldsymbol{f_2}(\boldsymbol{x})] = 2.2804 > 0$. Since $\boldsymbol{n}^T(\boldsymbol{x})\boldsymbol{f_1}(\boldsymbol{x}) > 0$, the system moves region with $\boldsymbol{f} = \boldsymbol{f_s}$.

- $t = 3$ (s): a time dependent switching occurs, exactly at that moment for $\dot{u} = -1$, and $h(\boldsymbol{x}) > 0$ so, the system continues with $\boldsymbol{f} = \boldsymbol{f_s}$. For values of t greater than 3, the input signal now starts to decrease.

- $t = 5.5728$ (s): The system has again struck the switching manifold with $u = 0.4268$. At this point, calculating,

$$\boldsymbol{n}^T(\boldsymbol{x})\boldsymbol{f_1}(\boldsymbol{x}) = [1 \quad 1] \begin{bmatrix} -1 \\ \\ 3(0.4268) \end{bmatrix} = 0.2804 \ ,$$

$$\boldsymbol{n}^T(\boldsymbol{x})\boldsymbol{f_2}(\boldsymbol{x}) = [1 \quad 1] \begin{bmatrix} -1 \\ \\ 0 \end{bmatrix} = -1 \ .$$

$[\boldsymbol{n}^T(\boldsymbol{x})\boldsymbol{f_1}(\boldsymbol{x})].[\boldsymbol{n}^T(\boldsymbol{x})\boldsymbol{f_2}(\boldsymbol{x})] = -0.2804 < 0$ and according to (5.13), the system slides along Σ. Next, the sliding vector field on Σ is calculated using (5.14,5.15):

$$\alpha(\boldsymbol{x}) = \frac{\boldsymbol{n}^T(\boldsymbol{x})\boldsymbol{f_1}(\boldsymbol{x})}{\boldsymbol{n}^T(\boldsymbol{x})(\boldsymbol{f_1}(\boldsymbol{x}) - \boldsymbol{f_2}(\boldsymbol{x}))} = \frac{3u-1}{3u} \ ,$$

$$\begin{aligned} \boldsymbol{f}_F(\boldsymbol{x}) &= (1-\alpha(\boldsymbol{x}))\boldsymbol{f_1}(\boldsymbol{x}) + \alpha(\boldsymbol{x})\boldsymbol{f_2}(\boldsymbol{x}) \\ &= \begin{bmatrix} x_1 \\ \\ x_2 \end{bmatrix} = \begin{bmatrix} -1 \\ \\ 1 \end{bmatrix} \ . \end{aligned}$$

- $t = 5.6663$ (s): At this point, $\alpha(\boldsymbol{x}) = 0$ for $u = \frac{1}{3}$ and the trajectory leaves Σ with vector field $\boldsymbol{f_{ns}}$.

- **Comparison with DB and LIT:** The DB value for S1 used is 0.003 and the integrator is limited ± 1.1 for S2. The simulation results are shown in Figure 5.4. Using FT and LIT (S2) the trajectory continues smoothly before and after each event; the DB approach will always results in chattering whenever a deadlock

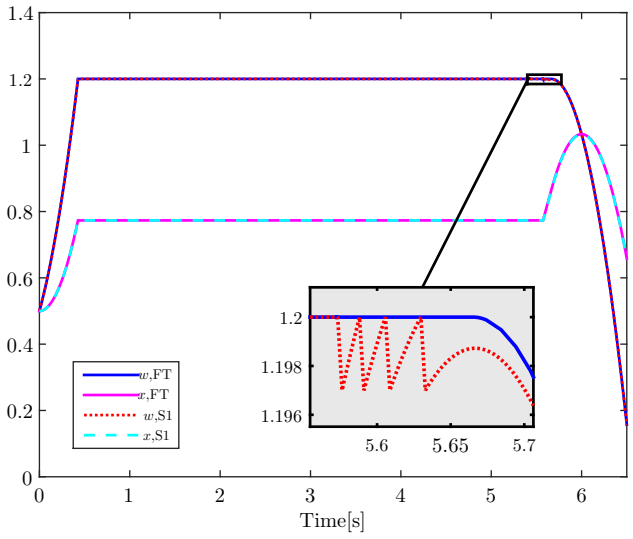

Figure 5.4: Comparison of trajectories using Filippov theory (FT), deadband approach (S1).

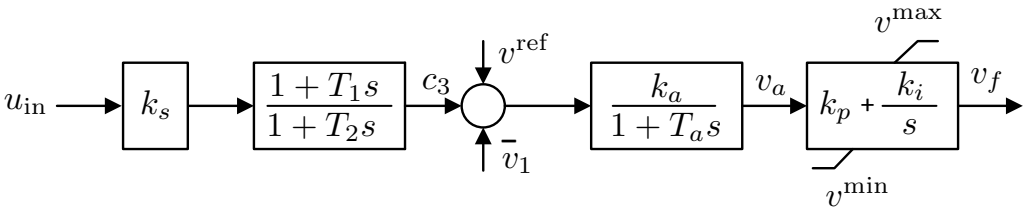

Figure 5.5: Block diagram of AVR and PSS.

condition appears.

5.4.2 Example II: Single Machine Infinite Bus

Consider the SMIB system shown in Figure 2.3, the generator is equipped with an AVR and a PSS as depicted in Figure 5.5. The generator model is a third order type; the PSS consists of a stabilizer gain and a lead lag block and the AVR is an static type with PI control [76]. The dynamics of the system is described by a set of explicit DAEs in the following form,

$$\dot{\boldsymbol{x}} = \boldsymbol{f}(\boldsymbol{x}, \boldsymbol{y}) \ , \tag{5.17}$$

$$\boldsymbol{0} = \boldsymbol{g}(\boldsymbol{x}, \boldsymbol{y}) \ , \tag{5.18}$$

where $\boldsymbol{x}$ and $\boldsymbol{y}$ are the vector of state and algebraic variables respectively.

For this test system, $\boldsymbol{x} = [\delta \ \omega \ e'_q \ v_a \ x_i \ s_1]^T$, $\boldsymbol{y} = [v_1 \ v_3 \ \theta_1 \ \theta_3 \ v_f \ c_1 \ c_2 \ c_3]^T$, where δ, ω, e'_q are the rotor angle, rotor speed and q-axis transient voltage respectively; v_a, x_i and s_1 are the state variables of AVR and PSS; v_1, v_3, θ_1, θ_3 are the bus voltages and angles respectively; v_f is the generator field voltage; c_1, c_2, c_3 are the algebraic variables of PSS.

The algebraic equations of the SMIB system are given by,

$$\begin{aligned}
0 &= -p_e + b_{13} v_1 v_3 \sin(\theta_1 - \theta_3) \ , \\
0 &= b_{13} v_3 v_1 \sin(\theta_3 - \theta_1) + b_{23} v_3 \sin(\theta_3) + p_l \ , \\
0 &= -q_e + b_{13}[v_1^2 - v_1 v_3 \cos(\theta_1 - \theta_3)] \ , \\
0 &= b_{13}[v_3^2 - v_3 v_1 \cos(\theta_3 - \theta_1)] + b_{23}[v_3^2 - v_3 \cos(\theta_3)] + q_l \ , \\
0 &= -v_f + k_p v_a + x_i \ , \\
0 &= c_1 - u_{\text{in}} k_s \ , \\
0 &= c_2 - c_1(1 - \frac{T_1}{T_2}) \ , \\
0 &= c_3 - c_1(\frac{T_1}{T_2}) - s_1 \ ,
\end{aligned}$$

where $b_{13} = 1/x_{13}$ and $b_{23} = 1/x_{23}$ are known line parameters; k_p, k_s, T_1 and T_2 are the control parameters of AVR and PSS; input to the PSS is $u_{\text{in}} = \omega$; $p_l = p_{l0}(\frac{v_3}{v_{30}})$, $q_l = q_{l0}(\frac{v_3}{v_{30}})^2$, v_{30} is known from power flow calculation; p_{l0} and q_{l0} are the active and reactive power of the load respectively; the reactive and active power of the

generator are: $q_e = -\frac{1}{x'_d}[v_1^2 - e'_q v_1 \cos(\theta_1 - \delta_1)]$, $p_e = \frac{e'_q v_1}{x'_d}\sin(\delta - \theta_1)$ respectively. Note that, the voltage and angle of the infinite bus are $v_{20} = 1$ and $\theta_{20} = 0$ respectively.

The PI controller in AVR (see Figure 5.14) is an IEEE Std. type. Lets consider the switching manifold for an upper limit, $h(\boldsymbol{x}) = k_p v_a + x_i - v^{\max}$. When $h(\boldsymbol{x}) < 0$, the differential equations of the SMIB system are given by ,

$$\dot{\delta} = \omega \ , \tag{5.19}$$

$$\dot{\omega} = \frac{1}{M}(p_m - p_e - D\omega) \ , \tag{5.20}$$

$$\dot{e}'_q = \frac{1}{T'_{d0}}(v_f - \frac{x_d}{x'_d}e'_q + \frac{x_d - x'_d}{x'_d}v_1 \cos(\delta - \theta_1)) \ , \tag{5.21}$$

$$\dot{v}_a = (k_a(v^{\text{ref}} + c_3 - v_1) - v_a)/T_a \ , \tag{5.22}$$

$$\dot{x}_i = k_i v_a \ , \tag{5.23}$$

$$\dot{s}_1 = \frac{1}{T_2}(c_2 - s_1) \ , \tag{5.24}$$

where x_d, x'_d are the d-axis synchronous and transient reactance respectively; T'_{d0}, M, D and p_m are the d-axis open circuit transient time constant, the mechanical starting time, the damping coefficient and the mechanical power input to the generator respectively; v^{ref} is the reference voltage; T_a, k_i and k_a are the control parameters of AVR and PSS.

When $h(\boldsymbol{x}) > 0$ i.e. the field voltage reaches to its upper limit ($v^{\max}$) then (5.21) and (5.23) will be switched and all other states will remain same, as follows:

$$\dot{e}'_q = \frac{1}{T'_{d0}}(v^{\max} - \frac{x_d}{x'_d}e'_q + \frac{x_d - x'_d}{x'_d}v_1 \cos(\delta - \theta_1)) \ , \tag{5.25}$$

$$\dot{x}_i = 0 \ . \tag{5.26}$$

Table 5.1: Parameters of the AVR and PSS

Name	Values
AVR	$k_a = 2$, $T_a = 0.005$, $k_p = 5.5$, $k_i = 35$, $v^{\max} = 1.58$, $v^{\min} = -1.5$, $v^{\text{ref}} = 1$
PSS	$k_s = 1.5$, $T_1 = 0.23$, $T_2 = 0.12$

We consider $\boldsymbol{f_1(x, y)}$ is (5.19)-(5.24) and $\boldsymbol{f_2(x, y)}$ is (5.19), (5.20), (5.25), (5.22), (5.26) and (5.24). Calculating, $\boldsymbol{h_x(x)} = [\frac{\partial h(\boldsymbol{x})}{\partial x_1} \quad \frac{\partial h(\boldsymbol{x})}{\partial x_2} \ ... \ \frac{\partial h(\boldsymbol{x})}{\partial x_6}]^T = [0\ 0\ 0\ k_p\ 1\ 0]^T$, and the normal to the switching surface is: $\boldsymbol{n}^T(\boldsymbol{x}) = [0\ 0\ 0\ k_p\ 1\ 0]$.

The initial values of the state variables and algebraic variables are calculated from the power flow solution and are: $\boldsymbol{x_0} = [\delta_0\ \omega_0\ e'_{q0}\ v_{a0}\ x_{i0}\ s_{10}]^T = [0.702\ 0\ 1.10\ 0\ 1.478\ 0]^T$, $\boldsymbol{y_0} = [v_{10}\ v_{30}\ \theta_{10}\ \theta_{30}\ v_{f0}\ c_{10}\ c_{20}\ c_{30}]^T = [1\ 0.962\ 0.473\ 0.156\ 1.478\ 0\ 0\ 0]^T$. The parameters of the generator, load and lines are given in Table 2.2 and rest of the component's parameters are given in Table 5.1.

The SMIB test system is simulated by applying a step increase to load ($p_{l0} = 0.701, q_{l0} = 0.015$) and voltage reference set-point of AVR ($v^{\text{ref}} = 1.01$) at 5 s. The response of the PI controller state, field voltage and limited field voltage (v_f^*) using FT are shown in Figure 5.6. To explain how FT is applied during each event, $h(\boldsymbol{x})$; $r_1 = \boldsymbol{n}^T(\boldsymbol{x})\boldsymbol{f_1(x, y)}$ and $r_2 = \boldsymbol{n}^T(\boldsymbol{x})\boldsymbol{f_2(x, y)}$ are shown in Figure 5.7. Simulation results clearly show that a piece-wise smooth solution is achieved using Filippov solution technique. Relevant remarks on the simulation results are given below:

- For the initial operating point of the system $h(\boldsymbol{x}) < 0$, so the system simulation starts with $\boldsymbol{f_1(x, y)}$.
- At 5 s the disturbance is applied and a little bit after that the system reaches to the switching manifold i.e. $h(\boldsymbol{x}) = 0$. Due to the condition (5.11) and $r_1 > 0$ (see

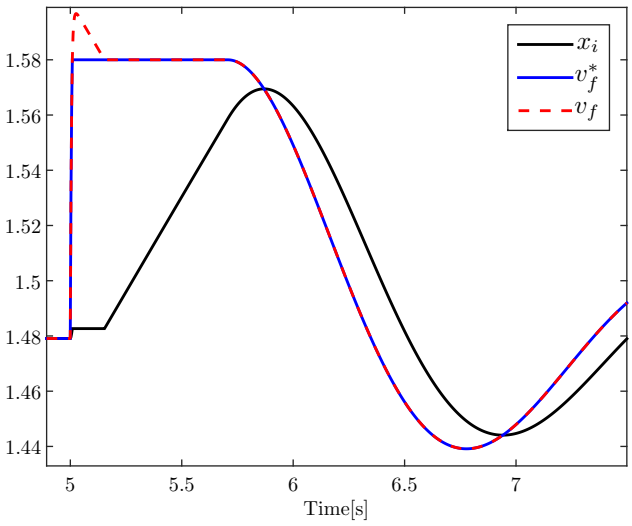

Figure 5.6: Response of the state and field voltage using Filippov theory.

Figure 5.7) a transversal crossing is happened. The system switches to $\boldsymbol{f_2(x, y)}$ and the integrator state and the field voltage become constant (see Figure 5.6). The system continues with $\boldsymbol{f_2(x, y)}$ as long as $h(\boldsymbol{x}) > 0$.

- At $t = 5.153$ s, $h(\boldsymbol{x}) = 0$ again (see the arrow in Figure 5.7) and the conditions (5.12) and (5.13) are met, so an attracting sliding mode occurs on $h(\boldsymbol{x}) = 0$. The vector field ($\boldsymbol{f}_F(\boldsymbol{x}, \boldsymbol{y})$) and $\alpha(\boldsymbol{x}, \boldsymbol{y})$ are calculated numerically using (5.14) and (5.15). Therefore during that sliding $h(\boldsymbol{x})$ remains at 0, the system continues with $\boldsymbol{f}_F(\boldsymbol{x}, \boldsymbol{y})$ (see Figures 5.6-5.7).

- The system moves to $\boldsymbol{f_1(x, y)}$ when $h(\boldsymbol{x}) < 0$.

The theory of Filippov assumes systems are modeled using ODEs. However in this example, the system model employs DAEs to simulate power systems. The application of FT was possible due to the fact that $h(\boldsymbol{x})$ depended only on the state variables and not the algebraic ones. In addition, the case studies shows the effectiveness of FT for upper limit of the IEEE AW PI controller but it is trivial to

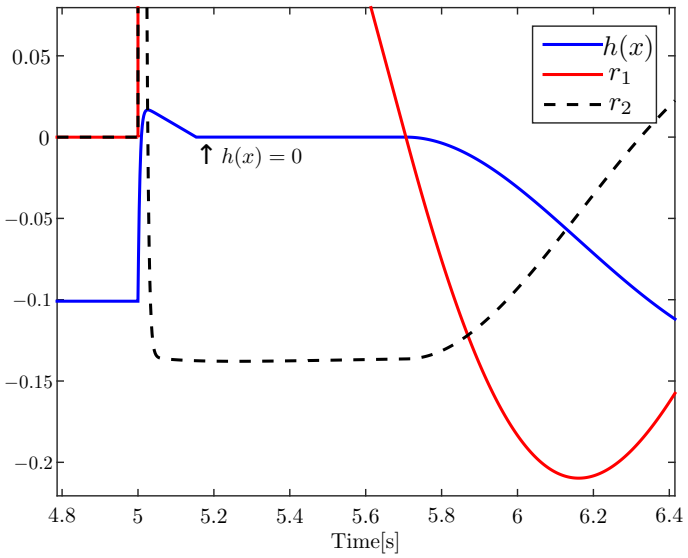

Figure 5.7: Response of the switching manifold $h(\boldsymbol{x})$, $r_1 = \boldsymbol{n}^T(\boldsymbol{x})\boldsymbol{f_1}(\boldsymbol{x},\boldsymbol{y})$ and $r_2 = \boldsymbol{n}^T(\boldsymbol{x})\boldsymbol{f_2}(\boldsymbol{x},\boldsymbol{y})$ using Filippov theory.

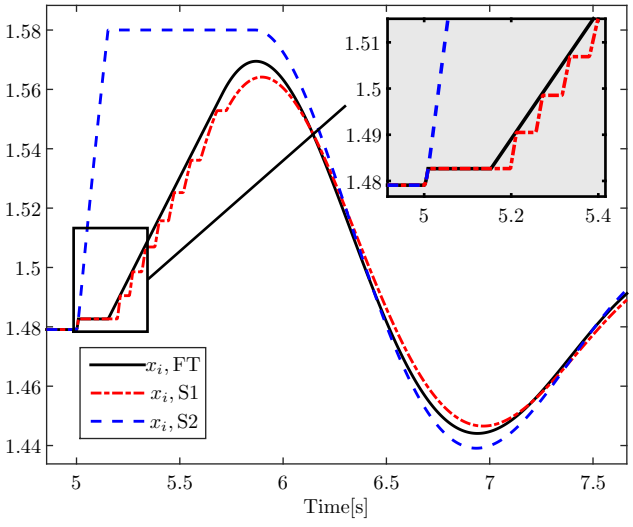

Figure 5.8: Comparison of trajectories using Filippov theory (FT), deadband approach (S1) and limited integrator technique (S2).

apply for lower limit too. For completeness Figure 5.8 compares the DB and LIT with the FT (only the integrator state is shown).

5.5 General-Purpose Design

According to FT, for every switching manifold a system can have three states, the two states for $h(\boldsymbol{x}) < 0$ (R1) and $h(\boldsymbol{x}) > 0$ (R2), and a new state called SLIDING, characterized by $h(\boldsymbol{x}) = 0$. For implementation in a software tool, two discrete variables are introduced, say z_1 and z_2, into the differential equations, as follows:

$$\dot{\boldsymbol{x}} = \boldsymbol{f_1}(\boldsymbol{x})z_1(1 - z_2) + \boldsymbol{f_2}(\boldsymbol{x})(1 - z_1)(1 - z_2) + \boldsymbol{f_F}(\boldsymbol{x})z_2 \ . \tag{5.27}$$

Observe that in the above equation, depending on the values of z_1 and z_2 (e.g. 1 or 0), a proper vector field needs to be activated during time domain simulation. Figure 5.9 shows the changes in (z_1, z_2) for the three states and the conditions to move from one state to another. All these conditions are based on FT and are evaluated the moment at which the event function ($h(\boldsymbol{x})$) crosses zero.

In the SLIDING state the value of $z_2 = 1$. This automatically deactivates $\boldsymbol{f_1}(\boldsymbol{x})$ and $\boldsymbol{f_2}(\boldsymbol{x})$ (see (5.27)) without the need of changing the value of z_1. So the previous value (z_1) is retained. The sliding vector field $\boldsymbol{f_F}(\boldsymbol{x})$ is derived explicitly according to (5.14). The exit conditions are defined based on (5.15). In particular, $\alpha(x) = 0$ and $\alpha(x) = 1$ are the conditions that indicate to move to the R1 and R2 regions, respectively.

5.5.1 Implementation

The generalized design is applied to IEEE Std. AW PI controller to create a modular model so that one implementation can be used in different power system

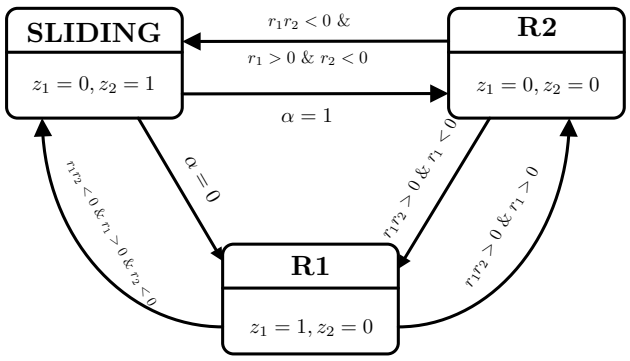

Figure 5.9: Generalized state transitions of Filippov systems.

components. This is presented in Section 5.7. In addition it can be also applied to other Filippov system models for example, Stick-Slip system [93], Relay Feedback System [93]. In Section 5.6 one such system is discussed.

For implementation in a computer language of this design a event driven or a time stepping approach can be used. Both approaches are previously discussed in Section 2.3.2. In following the applications presented utilize the Modelica language [7] considers an event driven implementation and the case studies utilize Dome considers a time stepping implementation.

5.6 Application I: A Relay Feedback System

A relay feedback system with single-input and single-output is as follows [93]:

$$\begin{aligned} \dot{\boldsymbol{x}} &= \boldsymbol{A}\boldsymbol{x} + \boldsymbol{B}u \ , \\ \boldsymbol{y} &= \boldsymbol{C}\boldsymbol{x} \ , \\ \boldsymbol{u} &= -\mathrm{sgn}(\boldsymbol{y}) \ , \end{aligned} \tag{5.28}$$

or

$$\dot{\boldsymbol{x}} = \begin{cases} \boldsymbol{A}\boldsymbol{x} + \boldsymbol{B}, & \text{when } \boldsymbol{C}x < 0 \ , \\ \boldsymbol{A}\boldsymbol{x} - \boldsymbol{B}, & \text{when } \boldsymbol{C}x > 0 \ , \end{cases} \tag{5.29}$$

where,

$$\boldsymbol{A} = \begin{pmatrix} -(2\zeta\omega + 1) & 1 & 0 \\ -(2\zeta\omega + \omega^2) & 0 & 1 \\ -\omega^2 & 0 & 0 \end{pmatrix}, \boldsymbol{B} = \begin{pmatrix} 1 \\ -2\sigma \\ 1 \end{pmatrix}, \boldsymbol{C} = \begin{pmatrix} 1 \\ 0 \\ 0 \end{pmatrix}.$$

The state vector of this model is $\boldsymbol{x} = [x_1, x_2, x_3]^T$ and the discontinuity surface Σ is defined by $h(\boldsymbol{x}) = x_1$. Re-writing the dynamical system according to FT,

$$\dot{\boldsymbol{x}} = \boldsymbol{f}(\boldsymbol{x}) = \begin{cases} \boldsymbol{f_1}(\boldsymbol{x}) & \text{when } h(\boldsymbol{x}) < 0 \ , \\ \boldsymbol{f_2}(\boldsymbol{x}) & \text{when } h(\boldsymbol{x}) > 0 \ , \end{cases} \tag{5.30}$$

with

$$\boldsymbol{f_1}(\boldsymbol{x}) = \begin{pmatrix} -(2\zeta\omega + 1)x_1 + x_2 + 1 \\ -(2\zeta\omega + \omega^2)x_1 + x_3 - 2\sigma \\ -\omega^2 x_1 + 1 \end{pmatrix},$$

$$\boldsymbol{f_2}(\boldsymbol{x}) = \begin{pmatrix} -(2\zeta\omega + 1)x_1 + x_2 - 1 \\ -(2\zeta\omega + \omega^2)x_1 + x_3 + 2\sigma \\ -\omega^2 x_1 - 1 \end{pmatrix}.$$

Here, $h_x(\boldsymbol{x}) = [1 \quad 0 \quad 0]^T$, thus on Σ (i.e. $x_1 = 0$), calculating,

$$r_1 = -(2\zeta\omega + 1)x_1 + x_2 + 1 \ , r_2 = -(2\zeta\omega + 1)x_1 + x_2 - 1 \ .$$

The sliding vector field on Σ obtained using equations (5.14,5.15):

$$\alpha(x) = (-(2\zeta\omega + 1)x_1 + x_2 + 1)/2 \ ,$$

$$\boldsymbol{f_F(x)} = \begin{pmatrix} 0 \\ b + 4(-(2\zeta\omega + 1)x_1 + x_2 + 1)/2 \\ c - 2(-(2\zeta\omega + 1)x_1 + x_2 + 1)/2 \end{pmatrix} \ ,$$

where $b = -(2\zeta\omega + \omega^2)x_1 + x_3 - 2\sigma$ and $c = -\omega^2 x_1 + 1$.

This example is implemented using Modelica language both in direct form (without considering FT) and using the proposed FT based formulation. The parameters considered are: $\zeta = 0.05, \omega = 25$ and $\sigma = -1$.

OpenModelica and Dymola were used to simulate this example, however these tools halt when simulating this example without considering FT. In OpenModelica, all solvers fail to simulate and report an error message because of deadlock. On the other hand, Dymola's solver DASSL fails to continue the simulation. However some fixed time step solvers for example: RkFix2 (second order Runge Kutta) and Euler allows to continue simulation exposing chattering. The simulation results obtained using Dymola are shown in Figures 5.10-5.11. Observe that chattering does not occur for the model implemented following the proposed approach based on FT. Because of unnecessary chattering during the simulation, the results are not

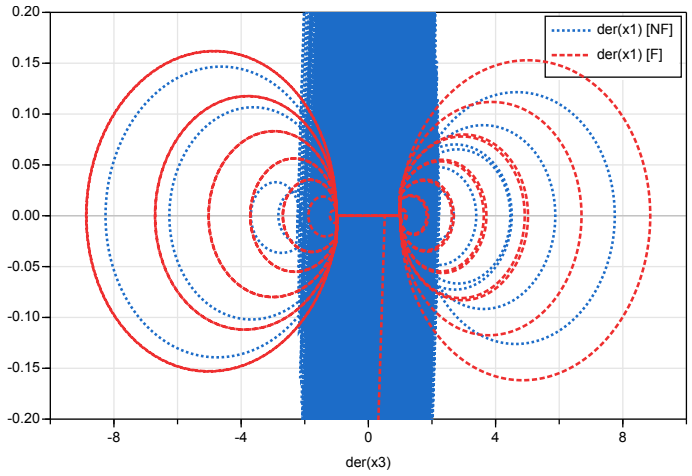

Figure 5.10: Time derivative of state variable ($\dot{x}_1$) of the relay feedback system model without (NF) and with (F) Filippov theory simulated in Dymola.

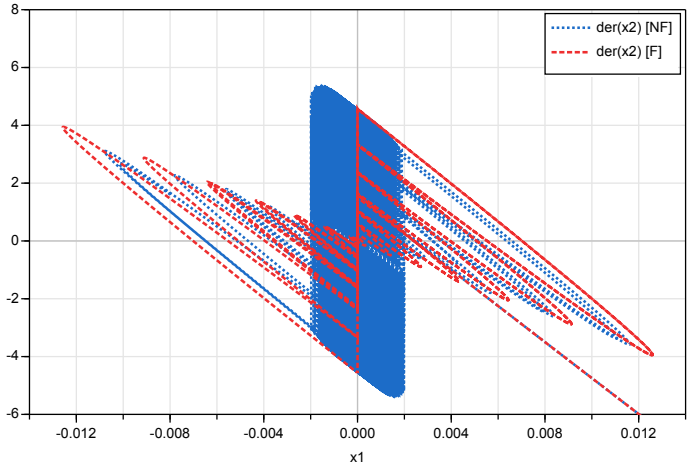

Figure 5.11: Time derivative of state variable ($\dot{x}_2$) of the relay feedback system model without (NF) and with (F) Filippov theory simulated in Dymola.

mathematically correct and it is not possible to understand the dynamic behavior of the real physical system. Therefore this generalized design overcomes deadlock and chattering and provides a smooth dynamic response.

Finally the validation of the results of Modelica tools against the implementation in Matlab [93] is shown in Figure 5.12. The Modelica code of this example is posted online: `https://github.com/ALSETLab/Modelica_Fillipov_Sliding_Models`.

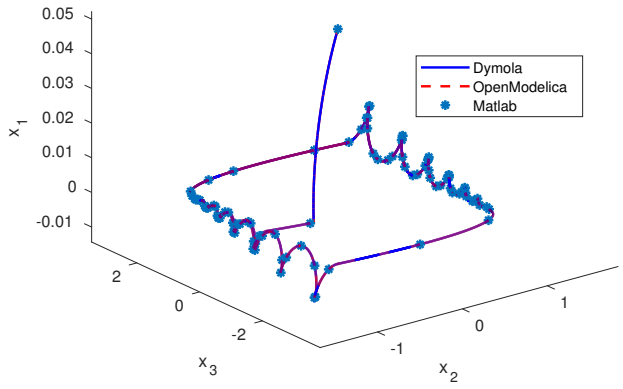

Figure 5.12: State space response for the relay feedback system obtained in different simulation software tools using Fillipov theory.

5.7 Application II: IEEE Std. AW PI Controller

Power systems models are described as DAEs. Therefore the input to a PI controller can be an algebraic or a state variable depending on the application. However FT is based exclusively on ODEs. References [10, 23, 24] where FT is applied into DAEs propose two possible ways briefly discussed in following.

- The first method converts the DAEs into ODEs. For example, if (5.18) can be re-write as $\boldsymbol{y} = \boldsymbol{k}(\boldsymbol{x})$, then (5.17) can be converted into $\dot{\boldsymbol{x}} = \boldsymbol{f}(\boldsymbol{x}, \boldsymbol{k}(\boldsymbol{x}))$. However for power system, the relation in (5.18) is non-linear and it is not trivial to convert the DAEs into ODEs.

- The second method considers directly the DAEs described by (5.17) and (5.18). However due to the lack of a theory on the coupling between the algebraic equations during sliding this method is still an open research [40].

Considering the limitations of the available methods to apply FT directly into all

form of DAEs, this Section presents a FT-based modular general purpose model of the IEEE Std. AW PI controller that is compatible with DAEs.

Let us consider the PI controller in Figure 5.13. This system is represented by (4.3) and

$$\begin{aligned} \dot{u} &= (v_1 - u)/T \ , \\ v_1 &= v - v^{\text{ref}} \ , \end{aligned} \tag{5.31}$$

where v_1 is the controlled signal and v^{ref} is the reference signal.

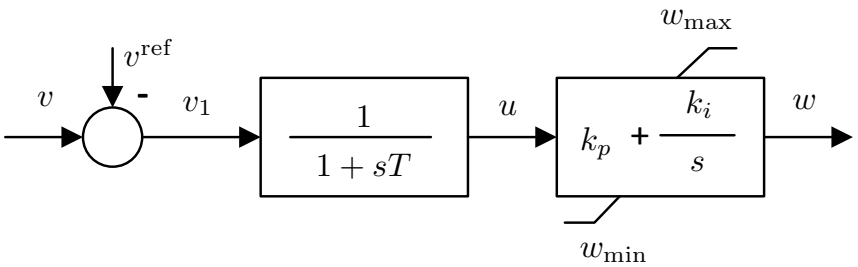

Figure 5.13: Generalized IEEE Std. anti-windup PI controller based on FT.

According to FT, the dynamical equations of this system can be represented as (considering the upper limit only),

$$\dot{\boldsymbol{x}} = \boldsymbol{f}(\boldsymbol{x}) = \begin{cases} \boldsymbol{f_1}(\boldsymbol{x}) & \text{if } h(\boldsymbol{x}) < 0 \ , \\ \boldsymbol{f_2}(\boldsymbol{x}) & \text{if } h(\boldsymbol{x}) > 0 \ , \end{cases}$$

with

$$\boldsymbol{f_1}(x) = \begin{pmatrix} (v_1 - u)/T \\ \\ k_i u \end{pmatrix}, \qquad \boldsymbol{f_2}(\boldsymbol{x}) = \begin{pmatrix} (v_1 - u)/T \\ \\ 0 \end{pmatrix},$$

and the surface Σ is defined by zero of $h(\boldsymbol{x}) = y - w_{\max} = k_p u + x - w_{\max}$ and

$h_x(\boldsymbol{x}) = [\frac{\partial h(x)}{\partial u} \quad \frac{\partial h(x)}{\partial x}]^T = [k_p \quad 1]^T$; $n^T(\boldsymbol{x}) = [k_p \quad 1]$. Hence

$$
\begin{aligned}
r_1 &= (k_p\ 1) \begin{pmatrix} (v_1 - u)/T \\ \\ k_i u \end{pmatrix} = k_p\big((v_1 - u)/T\big) + k_i u \ , \\
r_2 &= (k_p\ 1) \begin{pmatrix} (v_1 - u)/T \\ \\ 0 \end{pmatrix} = k_p\big((v_1 - u)/T\big) \ .
\end{aligned}
\tag{5.32}
$$

If a sliding condition is met, the sliding vector field on Σ using (5.14) and (5.15) becomes:

$$
\begin{aligned}
\alpha(x) &= \frac{k_p((v_1 - u)/T) + k_i u}{k_i u} \ , \\
\boldsymbol{f_F}(\boldsymbol{x}) &= \begin{pmatrix} (v_1 - u)/T \\ \\ -k_p((v_1 - u)/T) \end{pmatrix} \ .
\end{aligned}
\tag{5.33}
$$

An AW PI controller based on (5.32) and (5.33) provides correct dynamic response for any disturbance and transient condition. This is obtained through the introduction of the low pass filter. The FT, in fact, requires that all input signals are smooth (i.e. continuous and differentiable) variables. The low pass filter, however introduces a small delay in the transient behaviour of the input and, thus, has to be tuned so that its dynamic is faster than that of the PI controller. Since power system DAE models are intrinsically stiff, the condition on the dynamic of the low pass filter can be easily accommodated by any solver designed for transient stability analysis.

Based on (5.32) and (5.33), the controller has three states, the two states for

$h(\boldsymbol{x}) < 0$ (INT) and $h(\boldsymbol{x}) > 0$ (MAX), and a new state called SLIDING, characterized by $h(x) = 0$. For the computer implementation of the FT-based AW PI model the integrator differential equations, as follows:

$$\dot{x} = k_i u\, z_1 - \big(k_p(v_1 - u)/T\big)\, z_2 \ .$$

To consider the lower limit, $h(\boldsymbol{x}) = y - w_{\min} = k_p u + x - w_{\min}$ and $h_x(\boldsymbol{x}) = [\frac{\partial h(x)}{\partial u} \quad \frac{\partial h(x)}{\partial x}]^T = [k_p \quad 1]^T$; $n^T(\boldsymbol{x}) = [k_p \quad 1]$. Therefore, following a similar procedure, the minimum (MIN) state is implemented.

5.7.1 SMIB with ST4C Excitation System

The SMIB system presented in Section 5.4.2 (see Figure 2.3) is considered in this case study. However, the AVR is replaced with a simplified version of the ST4C static excitation system [8]. Observe that in this AVR there are two PI controllers. Utilizing the modular model in the previous section only one implementation is used with different inputs and outputs. Therefore one instance of the implemented model can be used as many times required by any application.

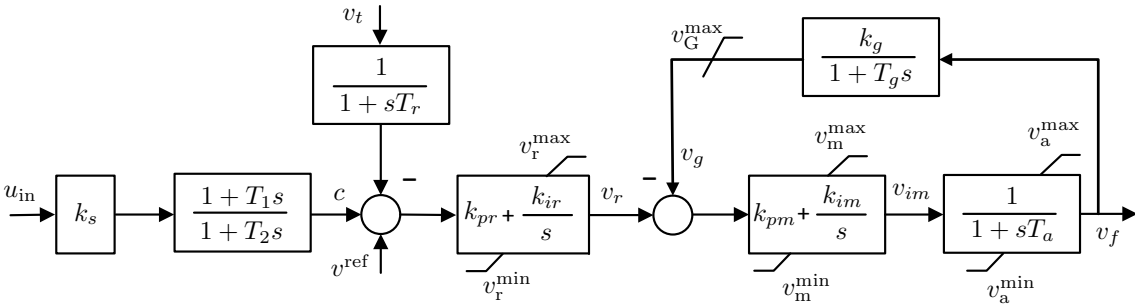

Figure 5.14: Control diagram of the ST4C static excitation system with inclusion of a PSS.

Table 5.2: Parameters of the ST4C AVR

Name	**Values**
AVR	$T_r = 0.005$, $k_{pr} = 10$, $k_{ir} = 25$, $k_{pm} = 2$, $k_{im} = 20$, $T_a = 0.02$, $T_g = 0.005$, $k_g = 0.18$, $v_{\mathrm{G}}^{\max} = 99$, $v^{\mathrm{ref}} = 1$

Except the AVR parameters, same values of all other parameters of the SMIB system given in Table 2.2 are used. For all PI models and the lag filter model (see Figure 5.14), the maximum and minimum values of the AW limiter are 2 and -0.8, respectively. The AVR parameters are given in Table 5.2.

As discussed in Section 5.2, the numerical integration of the IEEE AW PI controller can fail as a consequence of several factors. In the following, we consider two disturbances for which the solver gets stuck for validating the FT based AW PI controller. The Modelica-based simulation tool Dymola is used to solve all simulations for this case study. The deadband (DB) and time delay (TD) based PI controllers described in Section 4.3.2 are used for comparison. In all case studies the value of DB is 0.001. The time constant of the lag filter is $T = 0.001$ s for the FT-based AW PI model.

- **Contingency I:** A three phase fault occurring at 5 s and cleared after 100 ms is simulated in the SMIB system. Following the disturbance, both the PI controllers and the lag block of the AVR reaches their limits. Figure 5.15 shows the state-space representation $(x_{im}, \dot{x}_{im})$ of one the AW PI controller included in the AVR (see Figure 5.14). The FT-based AW PI controller provides a smooth response compared to the DB and TD implementations. Thus the main advantage of the FT model is that it removes the artificial chattering. To realize how this chattering is removed observe the sliding vector field in (5.33). During the

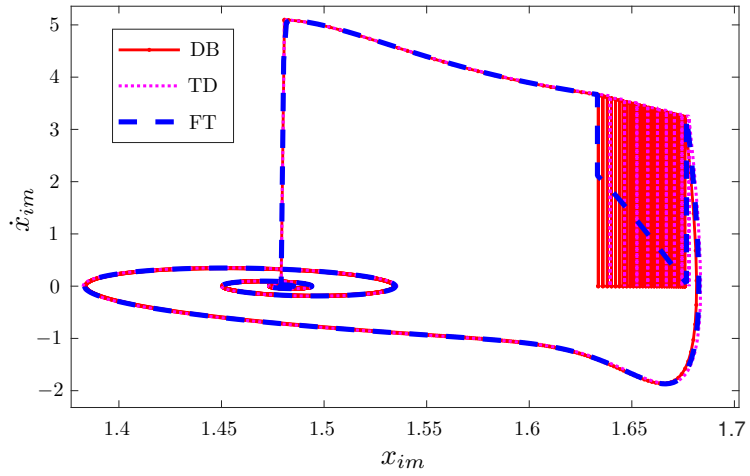

Figure 5.15: Time derivative of the integrator state variable ($\dot{x}_{im}$) with respect to the integrator state variable (x_{im}).

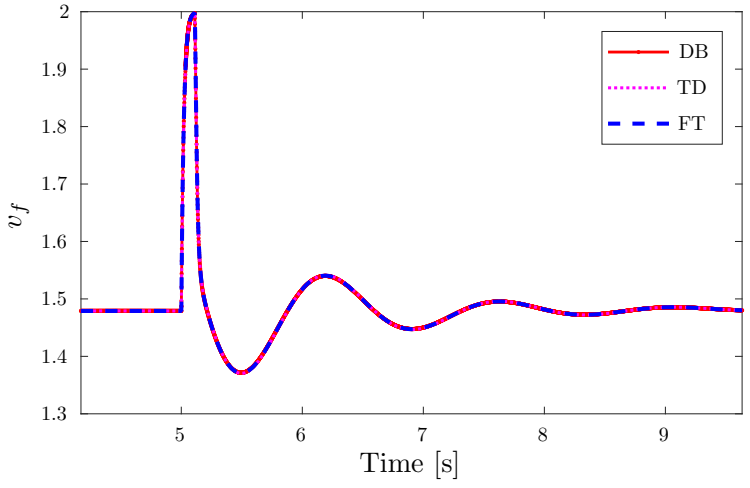

Figure 5.16: Trajectory of the output of the AVR.

sliding mode, the FT-based implementation allows increasing the integrator state variable consistently to the decrease of proportional channel of the controller. On the other hand, DB and TD models increase the integrator state variable by imposing some delay. This delay originates the chattering.

Compared to these techniques, the FT-based AW PI model requires less state events along the chattering region. Therefore an event location routine has to

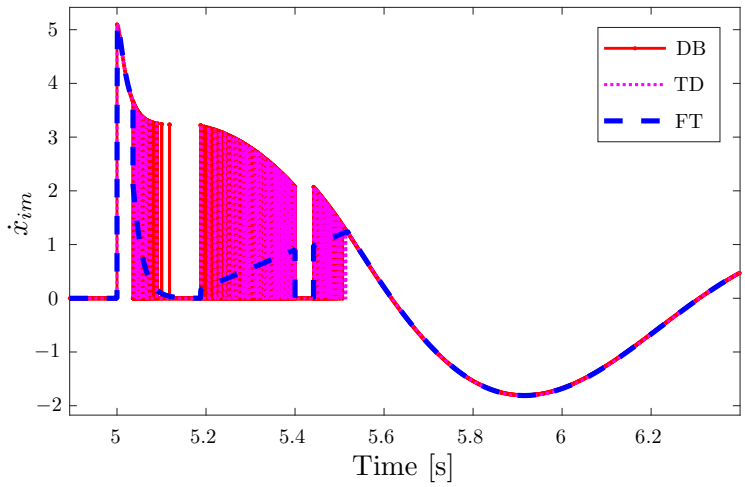

Figure 5.17: Response of the time derivative of integrator state variable ($\dot{x}_{im}$) with respect to time.

solve the roots of the zero-crossing equations for fewer discontinuous points and is thus less computationally demanding along the chattering region.

For completeness, Figure 5.16 illustrates the output of the AVR, i.e. the field voltage (v_f) and the response is identical for all the methods.

- **Contingency II:** The SMIB system is simulated by increasing the voltage reference set-point ($v^{\text{ref}} = 1.03$ pu) and the load ($p_{l0} = 0.8$ pu, $q_{l0} = 0.02$ pu) at $t = 5$ s. Figure 5.17 shows the time derivative of integrator state variable ($\dot{x}_{im}$) with respect to time. Following the disturbance, the integrator state variable x_{im} enters into the deadlock region for the DB and TD models. Then, x_{im} into the MAX state, comes back to the deadlock region and chatters again. While chattering, another step increase in the load ($p_{l0} = 0.82$ pu, $q_{l0} = 0.025$ pu) is applied at $t = 5.4$ s which drives x_{im} to the MAX state exactly at 5.4 s. Except for the chattering, the FT model shows same trajectory for x_{im} as the DB and TD models between the SLIDING and MAX states while the solution is at the SLIDING state for a step increase in the reference set-point. Thus the FT based

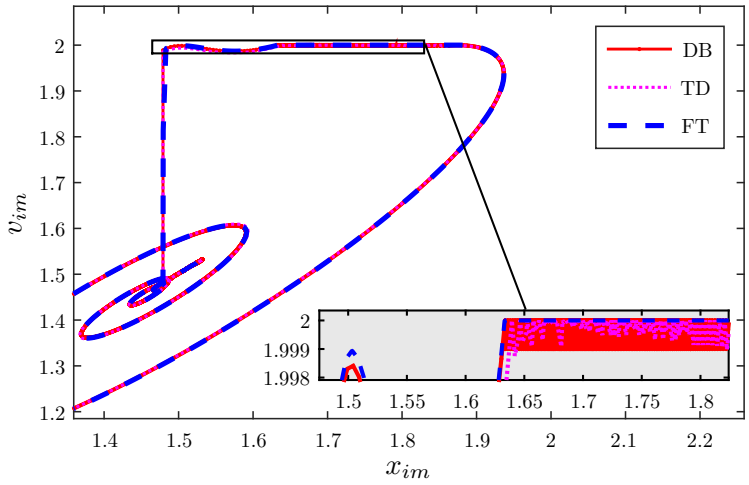

Figure 5.18: Response of the output (v_{im}) with respect to the integrator state variable (x_{im}).

method provides accurate dynamic response considering all kinds of disturbance. This proves that the proposed model is consistent with existing implementation and captures accurate hybrid system dynamics without any chattering.

Figure 5.18 shows the output (v_{im}) of the AW PI controller included in the AVR with respect to the integrator state variable (x_{im}). The trajectory obtained with the DB and TD models continues through switching during the deadlock period. It is already mentioned that the number of switches depends on the deadband width/delay magnitude as well as the time step of the simulation. On the other hand, the FT-based implementation is independent from the time step, as long as the time step is compatible with the numerical stability of the integration method and adequate for the DAE stiffness.

5.7.2 VSC-Based STATCOM

The WSCC 9-bus test system with a VSC-based STATCOM, connected at bus 8 is used described in Section 4.5 used for time domain simulation in DOME. A

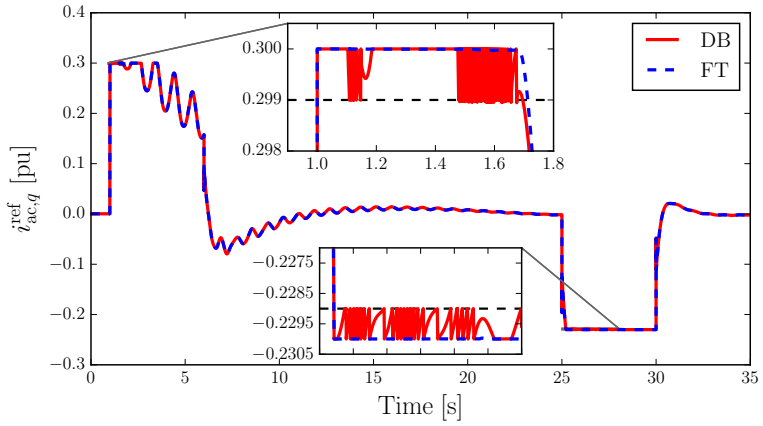

Figure 5.19: Response of the output of the AC voltage controller in the outer loop.

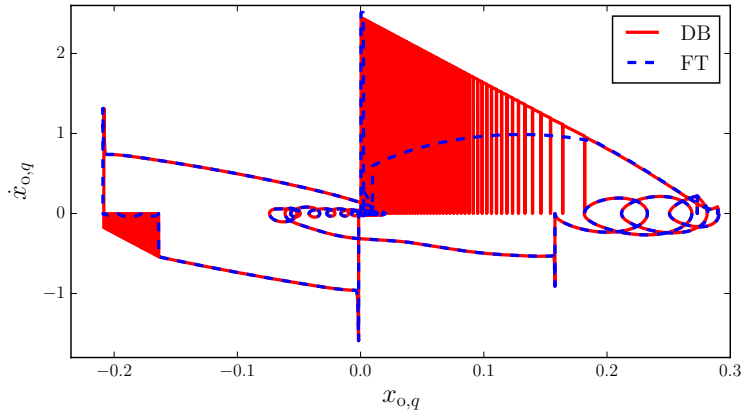

Figure 5.20: Time derivative of the integrator state variable with respect to the state variable of the AC voltage controller in the outer loop.

three phase fault occurring at $t = 1$ s is applied for 60 ms and cleared through disconnecting the line in between buses 6 and 9. The line is reconnected at $t = 6$ s. The dynamic response of the q-axis current reference ($i^{\text{ref}}_{\text{ac},q}$) is shown in Figure 5.19 for DB and FT models. The TD model is not compared in this case study as it shows similar results as the DB one.

Following the fault, the $i^{\text{ref}}_{\text{ac},q}$ reaches its maximum limit in the attempt to regulate

the voltage and comes back within the limit when the fault is cleared. Then the controller shows an oscillatory response to reach a steady state solution. From $t = 25$ to $t = 30$ s a step decrease in the reactive power load at bus 8 is applied. Due to this contingency the $i_{\mathrm{ac},q}^{\mathrm{ref}}$ moves to its minimum limit. The AW PI controller enters into a deadlock region in several occasions (zoomed in Figure 5.19) during the time frame of simulation. In the deadlock region the controller based on the DB model shows numerous chattering whereas the FT-based controller shows a smooth response. The trajectories of the time derivative of the integrator state variable of the AW PI controller of the AC voltage controller based on DB and FT models are shown in Figure 5.20, confirming the ability of the FT implementation to avoid chattering for both upper and lower limit region.

5.8 Conclusions

This Chapter studies the trajectory deadlock issue of the IEEE Standard 421.5-2016 AW PI controller model. To solve this deadlock problem Filippov theory is proposed. First this concept is proved using two illustrative examples. Then A general-purpose state transition diagram is proposed based on the FT to model and implement Filippov system models to remove trajectory deadlock and chattering. The conditions to automatically switch to different discontinuous vector fields are also duly derived. This case studies confirms the versatility of the proposed FT approach, which proves to be suitable for both event-driven (Dymola) and time-stepping (Dome) software tools. Other alternative solution techniques were also compared with the FT. Finally, the case studies show that the proposed design provide accurate dynamic response and is suitable for implementation in a power

system software tool.

6 Variable Limiters of VSCs

6.1 Introduction

The high-level controllers of VSCs include the most important control functions, e.g., active/reactive power control, AC/DC voltage control, fault ride-through functionality, current limitation. The response of these high-level controllers has a significant impact on power system dynamics [67,89]. If such controllers of the VSCs are PI and are coupled with a current limiter, several configurations are possible, illustrated in Figure 6.1. This Chapter mainly focuses on configurations [II] and [III] of Figure 6.1. For each of these two configurations, a windup or an anti-windup PI can be used with variable limits. Thus far, the interaction between the current limiter and the PIs with various variable limiting structure has not been studied. This Chapter fills this gap.

The working principle of the current limiting of VSCs depends on the priority of a quantity of interest. The choice of this priority depends on the VSC applications, for example: HVDC [22], FACTS [11], Type-3 and Type-4 Wind-Generator [13,45] and Energy Storage [35,36]. For instance, if the converter is connected to a heavily loaded area with possible voltage issues, the priority is given to the reactive power. This ensures reactive power support when the current limit is exceeded, and the remaining current is available for active power production. This priority-based method has been briefly discussed in Section 4.4.3. The model of the current limit block is

discussed in Section 6.2.1 for the configurations of upper level control considered in this Chapter.

Even though the mathematical model of the current limiter block is well-established, some open questions remain unanswered in the available literature. These are: (i) does any of the possible configurations (see Figure 6.1) have an impact on the numerical simulation?; (ii) how does the choice of the PI implementation impact the dynamic and numerical performance?; (iv) how does the limit values of current limit logic impact the overall system's dynamic response?; (iv) does the IEEE Std. AW PI model show numerical issues with variable limits? This Chapter addresses these questions using relevant case studies in Section 6.4.

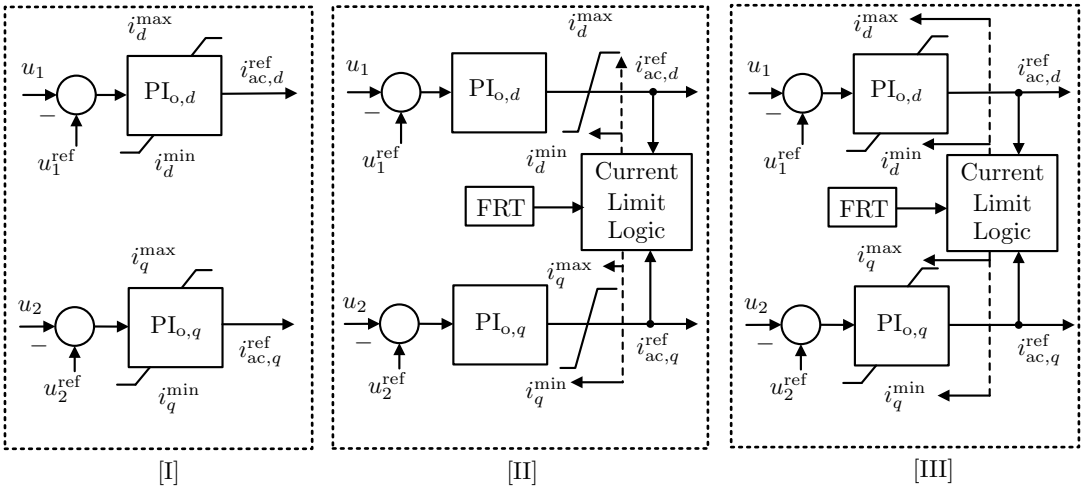

Figure 6.1: Outer control configurations: [I] constant limits; [II] variable limits with wind-up PIs and [III] variable limits with AW PIs.

The fourth question regarding the IEEE Std. AW model with variable limits, this Chapter shows that it has similar numerical issues similar to those discussed in Chapters 4-5. Therefore, the Filippov theory based AW model is extended to impose variable limits. Moreover, it has been discussed in previous Chapters that the deadband based AW PI model shows artificial chattering both in the output

and state variables. Observe that for the outer control configurations [II] and [III] in Figure 6.1, any chattering on the output will result in chattering in the maximum and minimum values of the other controller. In this Chapter, a modified DB based IEEE Std. AW is proposed to remove the chattering on the controller outputs.

The remainder of the Chapter is organized as follows. Section 6.2 discusses the current limiter and fault ride-through functionalities of VSCs. Section 6.3 presents the IEEE Std. PI model with variable limits and extends the FT based design discussed in the previous Chapter to impose variable limits. Section 6.3 also validates the IEEE Std. models through an illustrative example. Section 6.4 illustrates the dynamic behavior of VSCs through two case studies: (i) a VSC-HVDC link in the WSCC 9-bus network; (ii) the Nordic system with a VSC based STATCOM. Finally, Section 6.5 provides a brief discussion on simulation results and draws conclusions.

6.2 Current Limiters with Variable Limit

The current limit block limits the converter current references in the upper-level control of the VSCs is shown in Figure 6.1. The outputs of the current limit block determine the limits of the d- and q-axis PI controller (see configurations [II] and [III] in Figure 6.1) used in the outer level of VSCs. Fault ride-through (FRT) capabilities are also coupled into this block. This Section discusses the working principle of this block.

6.2.1 Current Limit Logic

Let us define the parameters of the current limit logic block: $i_{\max}$: maximum current capacity of the converter; i_d^{lm}: d-axis current limit and i_q^{lm}: q-axis current limit.

- **Active Power or DC voltage Priority:** If the priority is given to the active power or DC voltage, $i_{\text{ac},d}^{\text{ref}}$ is limited to the d-axis current limit whereas $i_{\text{ac},q}^{\text{ref}}$ is limited in such a way that the total current does not exceed the maximum current rating of the converters, as follows:

$$\begin{aligned} i_{\text{ac},d}^{\max} &= i_d^{\text{lm}} \ , \\ i_{\text{ac},d}^{\min} &= -i_{\text{ac},d}^{\max} \ , \\ i_{\text{ac},q}^{\max} &= \min(\sqrt{i_{\max}^2 - i_{\text{ac},d}^2}, i_q^{\text{lm}}) \ , \\ i_{\text{ac},q}^{\min} &= -i_{\text{ac},q}^{\max} \ . \end{aligned} \tag{6.1}$$

  where, $i_{\text{ac},d}^{\max}$, $i_{\text{ac},d}^{\min}$, $i_{\text{ac},q}^{\max}$ and $i_{\text{ac},q}^{\min}$ are the time varying limits of the PIs in the outer level control (see Figure 6.1). Note that, i_d^{lm} and i_q^{lm} can be set as equal or less than $i_{\max}$ [66]. In addition $i_{\text{ac},q}^{\min}$ can be different than the opposite sign of $i_{\text{ac},q}^{\max}$, which is not considered in this work.

- **Reactive Power or AC voltage Priority:** If the priority is given to the reactive power or AC voltage, $i_{\text{ac},q}^{\text{ref}}$ is limited by the q-axis current limit whereas $i_{\text{ac},d}^{\text{ref}}$ is limited in such a way that the total current does not exceed the maximum

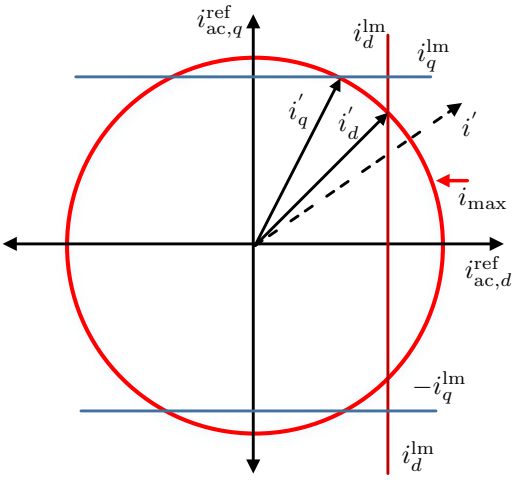

Figure 6.2: Geometrical representation of the current limit logic.

current rating of the converters, as follows:

$$
\begin{aligned}
i^{\text{max}}_{\text{ac},q} &= i^{\text{lm}}_{q} \ , \\
i^{\text{min}}_{\text{ac},q} &= -i^{\text{max}}_{\text{ac},q} \ , \\
i^{\text{max}}_{\text{ac},d} &= \min(\sqrt{i^{2}_{\text{max}} - i^{2}_{\text{ac},q}}, i^{\text{lm}}_{d}) \ , \\
i^{\text{min}}_{\text{ac},d} &= -i^{\text{max}}_{\text{ac},d} \ .
\end{aligned}
\tag{6.2}
$$

Similar to the active power priority, i^{lm}_{q} and i^{lm}_{d} can be set as equal or less than i_{max}. A graphical representation of the current limit logic is shown in Figure 6.2. In this figure, $i^{'}_{d}$ and $i^{'}_{q}$ are the currents with active and reactive power priority respectively; $i^{'}$ is the total current without any bound.

- **Fault Ride Through:** To comply with the grid code, VSC-based applications consider an FRT specification. Usually, FRT is activated if the ac voltage deviates from a pre-defined deadband/bound subjected to a disturbance. When FRT is activated, the controller switches its priority to reactive power for ac voltage

support [117]. In addition, during FRT, the q-axis controller can be replaced with a proportional control [66] to comply with the grid code. The FRT specification can define the gain of the proportional controller. In this work, if the ac voltage at the bus where the VSC is connected falls below 0.9 pu the FRT is activated, and priority is switched to reactive power support. And only if the voltage level returns within 0.92 pu the current limit logic switches off the FRT according to the grid code requirements.

6.3 PI Control with Variable Limits

The PI controller schemes presented in Section 4.2 (see Figure 4.2) depending on the applications can impose variable limits. The conditional AW limiter (PI2 in Figure 4.2) with an FT-based generalized design proposed in the previous Chapter considers only constant limits. However, if the limits become variable, the conditions to move from one state to another (for example, MAX to SLIDING, see Figure 5.9) need to observe the changes in the limits. In this Section, those conditions and the sliding vector field are deduced. In addition, a new DB-based implementation for IEEE Std. PI is proposed. All models are validated using an illustrative example.

6.3.1 FT based IEEE Std. AW PI Controller with Variable Limits

Let us consider the PI controller in Figure 6.3. This system is represented by (4.3) and

$$\begin{aligned} \dot{u} &= (v_1 - u)/T \ , \\ v_1 &= v - v^{\text{ref}} \ , \\ \dot{w}_{\max} &= (u_1 - w_{\max})/T_1 \ , \end{aligned} \tag{6.3}$$

where v_1 is the controlled signal, v^{ref} is the reference signal, u_1 is time varying input signal.

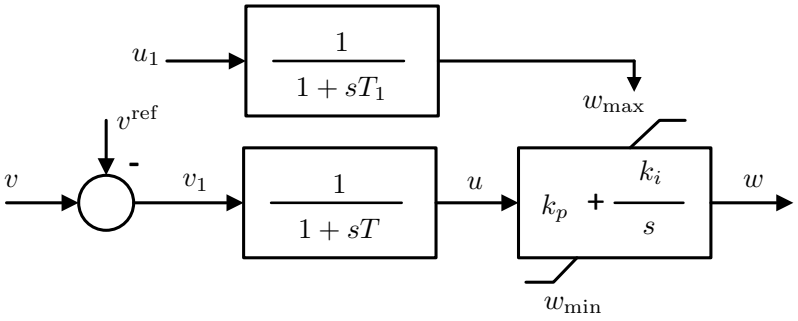

Figure 6.3: IEEE Std. anti-windup PI controller with variable limits.

The same procedure as that described in Section 6.3.1 (considering the upper limit only) is considered below to apply the FT, as follows:

$$\dot{\boldsymbol{x}} = \boldsymbol{f}(\boldsymbol{x}) = \begin{cases} \boldsymbol{f_1}(\boldsymbol{x}) & \text{if } h(\boldsymbol{x}) < 0 \ , \\ \boldsymbol{f_2}(\boldsymbol{x}) & \text{if } h(\boldsymbol{x}) > 0 \ , \end{cases}$$

with

$$\boldsymbol{f_1}(x) = \begin{pmatrix} (v_1 - u)/T \\ k_i u \\ (u_1 - w_{\max})/T_1 \end{pmatrix}, \qquad \boldsymbol{f_2}(\boldsymbol{x}) = \begin{pmatrix} (v_1 - u)/T \\ 0 \\ (u_1 - w_{\max})/T_1 \end{pmatrix},$$

and the surface Σ is defined by zero of $h(\boldsymbol{x}) = y - w_{\max} = k_p u + x - w_{\max}$ and $h_x(\boldsymbol{x}) = [\frac{\partial h(x)}{\partial u} \quad \frac{\partial h(x)}{\partial x} \quad \frac{\partial h(x)}{\partial w_{\max}}]^T = [k_p \quad 1 \quad -1]^T$; $n^T(\boldsymbol{x}) = [k_p \quad 1 \quad -1]$. Hence

$$\begin{aligned} r_1 &= (k_p \quad 1 \quad -1) \begin{pmatrix} (v_1 - u)/T \\ k_i u \\ (u_1 - w_{\max})/T_1 \end{pmatrix} = k_p\big((v_1 - u)/T\big) + k_i u - (u_1 - w_{\max})/T_1 \ , \\ r_2 &= (k_p \quad 1 \quad -1) \begin{pmatrix} (v_1 - u)/T \\ 0 \\ (u_1 - w_{\max})/T_1 \end{pmatrix} = k_p\big((v_1 - u)/T\big) - (u_1 - w_{\max})/T_1 \ . \end{aligned} \tag{6.4}$$

The sliding vector filed becomes:

$$\begin{aligned} \alpha(x) &= \frac{k_p((v_1 - u)/T) + k_i u - (u_1 - w_{\max})/T_1}{k_i u} \ , \\ \boldsymbol{f_F}(\boldsymbol{x}) &= \begin{pmatrix} (v_1 - u)/T \\ \\ -k_p((v_1 - u)/T) + (u_1 - w_{\max})/T_1 \end{pmatrix} . \end{aligned} \tag{6.5}$$

Therefore, for the computer implementation of the FT-based AW PI model with

variable limits the integrator differential equations, as follows:

$$\dot{x} = k_i u\, z_1 + \big(- k_p(v_1 - u)/T + (u_1 - w_{\max})/T_1 \big)\, z_2 \ .$$

The lower limit can be implemented following a similar procedure.

6.3.2 DB based IEEE Std. AW PI Controller with Variable Limits

The state transition diagram of the deadband-based implementation presented in Section 4.3.2 is the same when the limits are variable. As opposed to the previous implementation, in this case, a modification of the conditions to switch the right-hand side of the time derivative of the integrator state variable is proposed. This modification leads the chattering of the unbounded variable (y) during a deadlock situation, and the bounded variable (w) remains smooth. It is further explained using an illustrative example in the following and through the case studies in Section 6.4. The state transitions of the previous and the modified methods are shown in Figure 6.4.

6.3.3 Illustrative Example

The two PI controllers shown in Figure 6.5 with arbitrary inputs are considered as an illustrative example to validate the DB and FT based implementations of the IEEE Std. PI model. The current limiter controls the limits of both PI controllers. The priority is given to the d-axis current. The parameters are given in Table 6.1.

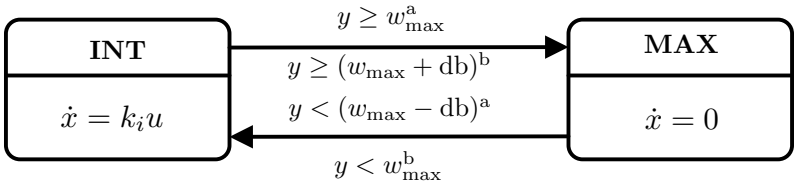

Figure 6.4: State transitions of the anti-windup PI controller for existing solutions: superscripts a and b indicate the deadband- techniques DB1 and DB2, respectively.

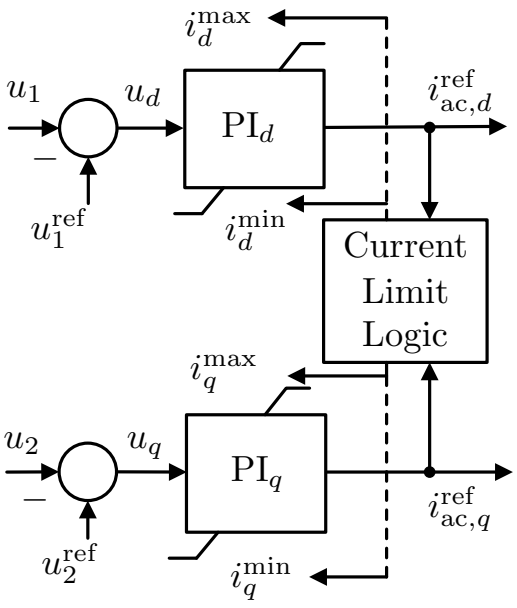

Figure 6.5: PI controllers with arbitrary inputs and current limiter.

This example is implemented in DOME and Modelica based tool Dymola. In both software, simulation is carried out using DB based (DB1 and DB2) and FT based implementations. The time-varying inputs to the PI controllers (PI_d and PI_q) are shown in Figure 6.6. For this input, the output of PI_d hits the limit several occasions, and as the priority is given to this controller, the maximum and minimum values of this controller do not change during the simulation. However, the limit values of PI_q are updated following the current limit logic (6.1) during the simulation. Those time-varying limits are shown are in Figures 6.7-6.9 for DB1, DB2 and Filippov based implementations respectively. For all these three implementations, only DB1

Table 6.1: Parameters of the illustrative example

Name	Values
PI_d	$k_p = 1,\ k_i = 10$
PI_q	$k_p = 1,\ k_i = 30$
Cur. Limiter	$i_{\max} = 1.02,\ i_d^{\mathrm{lm}} = 1.02$

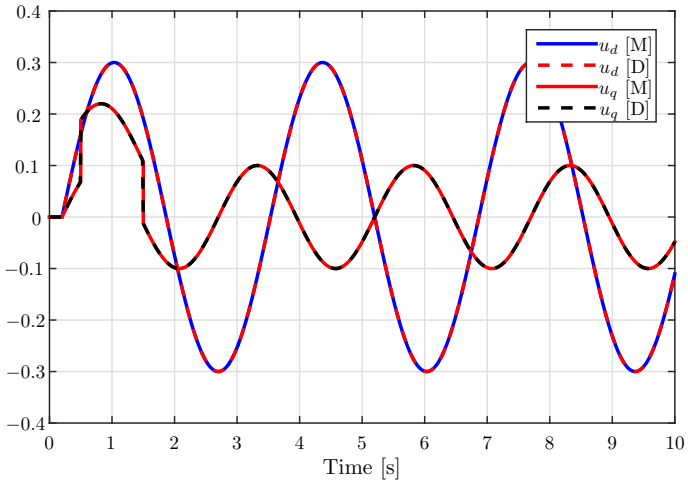

Figure 6.6: Inputs to the PI_d and PI_q in DOME ([D]) and Modelica ([M]).

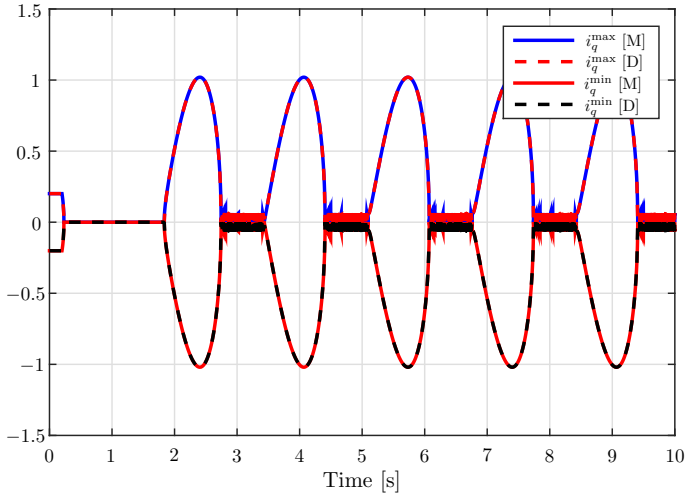

Figure 6.7: Maximum and minimum limits of PI_q controller in DOME ([D]) and Modelica ([M]) using DB1 based implementation.

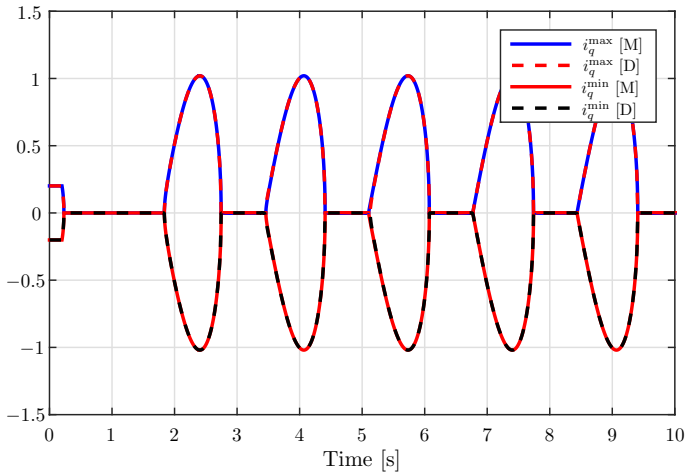

Figure 6.8: Maximum and minimum limits of PI_q controller in DOME ([D]) and Modelica ([M]) using DB2 based implementation.

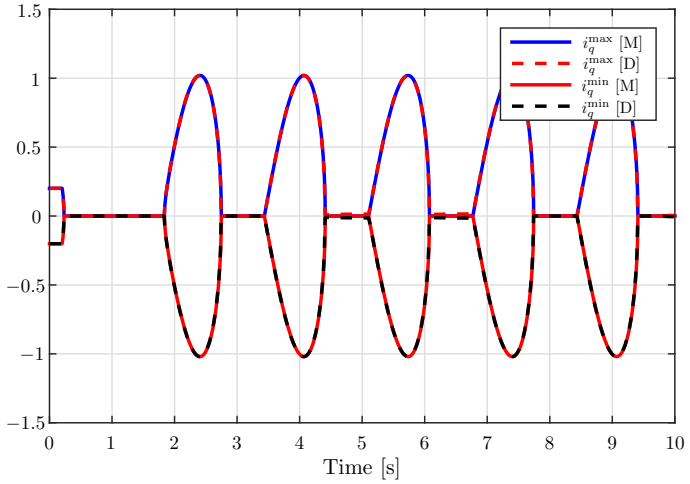

Figure 6.9: Maximum and minimum limits of PI_q controller in DOME ([D]) and Modelica ([M]) using Filippov based implementation.

based method shows chattering in the limit values. This is because of the chattering of the output of the PI_d controller during a deadlock region.

The response of the outputs of the PI_d and PI_q are shown in Figure 6.10. The outputs do not exceed the maximum limit (see Table 6.1) and follow the current limit logic. Moreover, they show similar responses, and only DB1 based method

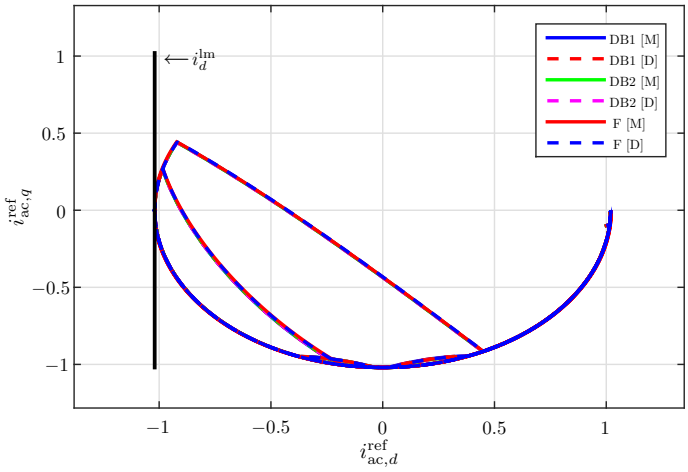

Figure 6.10: Response of the outputs of the PI_d and PI_q controllers in DOME ([D]) and Modelica ([M]) using DB1, DB2 and Filippov based implementation.

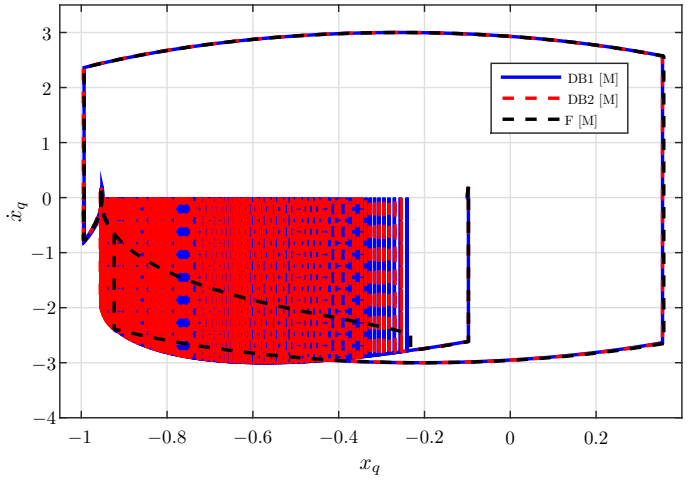

Figure 6.11: Time derivative of the integrator state variable with the state variable of the PI_q controller in Modelica ([M]) using DB1, DB2 and Filippov based implementation.

shows chattering on the output. DB2 and Filippov methods do not show chattering on the output. However, the DB2 method shows chattering on the state variable. This has been illustrated in Figures 6.11-6.12. Therefore, the Filippov based model overcomes possible numerical issues and provides an accurate dynamic response.

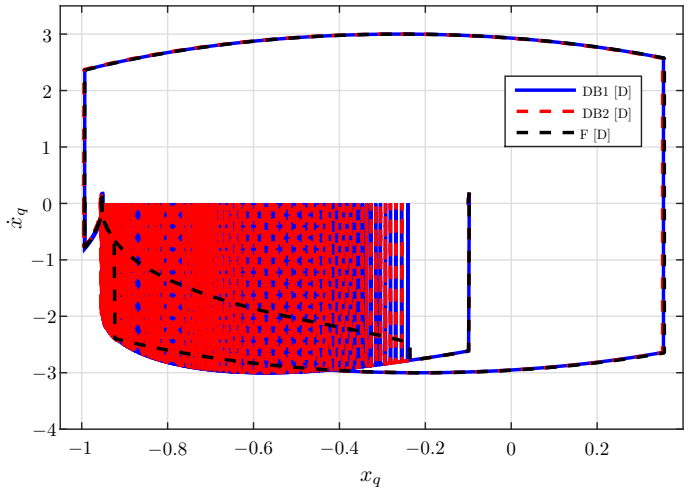

Figure 6.12: Time derivative of the integrator state variable with the state variable of the PI_q controller in DOME ([D]) using DB1, DB2 and Filippov based implementation.

6.4 Case Studies

This Section illustrates the impact of three different PI controller configurations utilized in VSC-based devices with current limit logic on the dynamic response of power systems. The three PI controller configurations are: windup (PI1 in Figure 4.2), anti-windup with back calculation (PI4 in Figure 4.2) and the IEEE Std. PI model (PI2 in Figure 4.2). For PI2, the deadband-based methods (DB1 and DB2) and the Filippov solution methods are considered. Two applications of VSC-based devices are discussed: (i) a point-to-point VSC-HVDC link (Section 6.4.1); and (ii) a STATCOM device (Section 6.4.2). The case study of VSC-HVDC link considers the WSCC 9-bus system, whereas the case study on the STATCOM considers the Nordic-32 system.

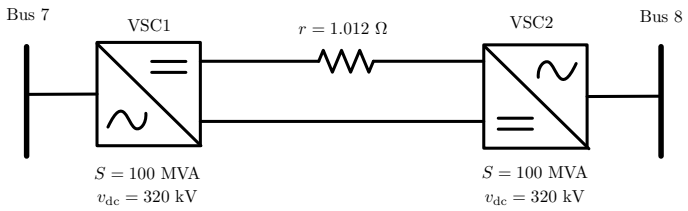

Figure 6.13: VSC-HVDC link between bus 7 and bus 8.

6.4.1 VSC-HVDC Link

The WSCC 9-bus system presented in Section 4.5 is used in this case study. The transmission line that connects buses 7 and 8 is replaced with a VSC-HVDC Link. The original operating condition is assumed, i.e. 76 MW active power is transferred through the HVDC lines. The converter at bus 7 (VSC1) transfers power from AC to DC side and the one at bus 8 (VSC2) vice versa. This is illustrated in Figure 6.13. VSC1 controls the DC voltage and AC voltage of bus 7 and VSC2 controls the active power and AC voltage of bus 8. The priority for the current limiters of VSC1 and VSC2 is DC voltage and active power, respectively, i.e., d-axis current. FRT is included in both VSCs. Two scenarios are studied with different current limit values, as shown in Table 6.2. For both scenarios, the contingency is a three-phase fault at bus 5 that occurs at 0.1 s and cleared after 150 ms by opening the line that connects the buses 4 and 5. The magnitude of the deadband is 0.001 for the deadband based PI implementations in the VSCs. Simulation results of both scenarios are discussed below.

- **Scenario I:**

Figure 6.14 shows the voltage response at bus 7 following the contingency. In this case, the PI2 model does not show any deadlock or chattering issues. The implementations based on the deadband and on the Filippov approach show a similar

Table 6.2: Parameters of current limit logic of VSCs

Parameters	Scenario I		Scenario II	
	VSC1	**VSC2**	**VSC1**	**VSC2**
Priority	v_{dc}	p	v_{dc}	p
i_d^{lm}	1.1 pu	1.1 pu	1.1 pu	1.1 pu
i_q^{lm}	1.1 pu	1.1 pu	0.5 pu	0.5 pu
i_{max}	1.1 pu	1.1 pu	1.1 pu	1.1 pu

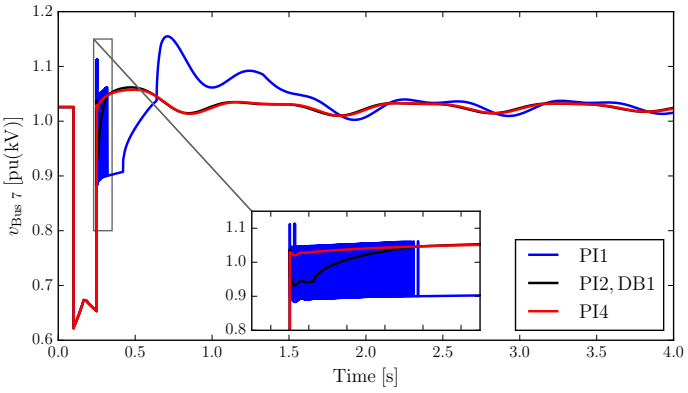

Figure 6.14: Scenario I: Response of the bus voltage ($v_{\mathrm{Bus\ 7}}$) considering PI1, PI2 (DB1) and PI4.

transient response. For this reason only results for the PI2 model with DB1-based implementation are shown. Anti-windup models show a very similar response with only minimal difference. However, the windup method (PI1) shows significantly different transient response with numerous chattering. For further explanation of this chattering Figures 6.15-6.16 show the variation of the maximum limits and reference current outputs of $\mathrm{PI}_{\mathrm{o},d}$ and $\mathrm{PI}_{\mathrm{o},q}$ (see Figure 6.1) of the outer level of VSC1.

Immediately after the fault occurs, the bus voltage falls under 0.9 pu and the FRT is activated. It causes the priority to switch to reactive power or q-axis current. As the d-axis current limit (i_d^{lm}) and the q-axis current limit (i_q^{lm}) are equal to the

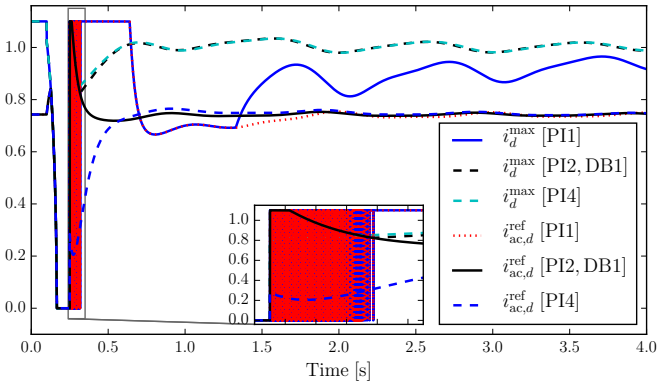

Figure 6.15: Scenario I: Response of the maximum limit and the output current reference of $\text{PI}_{\text{o},d}$ considering PI1, PI2 (DB1) and PI4 in VSC1.

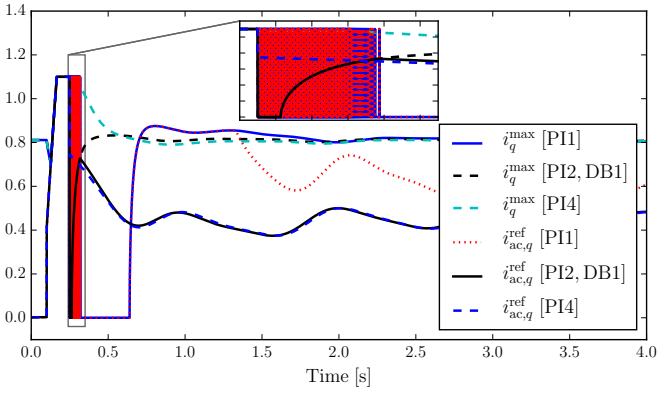

Figure 6.16: Scenario I: Response of the maximum limit and the output current reference of $\text{PI}_{\text{o},q}$ considering PI1, PI2 (DB1) and PI4 in VSC1.

maximum current capacity ($i_{\max}$) after the switching of priority the maximum limit of the $\text{PI}_{\text{o},d}$ falls to zero (see Figure 6.15). The current reference follows this variable limit. At the same moment, the limiter of the $\text{PI}_{\text{o},q}$ reaches the maximum current, as shown in Figure 6.16. This enables maximum reactive power support from the VSC1. Note that while all PI controllers are at their limits, the state variables of PI1, PI2 and PI4 do not stay at the same level. That is why they show significantly different results for some moment during the transient response. Using PI1, after

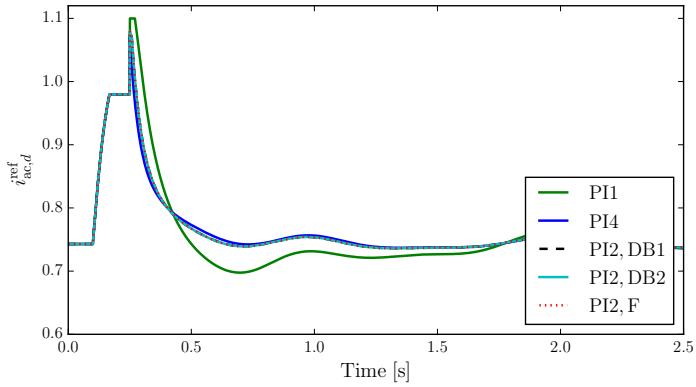

Figure 6.17: Scenario II: Response of the output current reference of $\text{PI}_{\text{o},d}$ considering PI1, PI2 (DB1, DB2 and F) and PI4 in VSC1.

clearing the fault once the bus voltage returns in the safe operating margin (> 0.92 pu) the priority switches back to the d-axis current. However, due to windup effect, the d-axis reference current moves to the maximum current (see Figure 6.15). This immediately results in the zero current reference for the q-axis controller and the reactive power support is ceased. This in turn lowers the voltage from 0.9 pu and the priority again switches backs to the q-axis current. This switching of priorities continues for a while and leads to chattering (see zoom in Figures 6.15-6.16). This chattering significantly impacts on the performance of the numerical simulation can give raise to deadlocks.

- **Scenario II:**

In this scenario, the i_q^{lm} is lower than the maximum current capacity in both VSCs. Following the contingency the reference currents of $\text{PI}_{\text{o},d}$ and $\text{PI}_{\text{o},q}$ in VSC1 are shown in Figures 6.17 and 6.18 respectively for all the considered PI models. These figures also include DB1, DB2 and Filippov methods for PI2. After the contingency, the priority is switched to the reactive power and the q-axis current

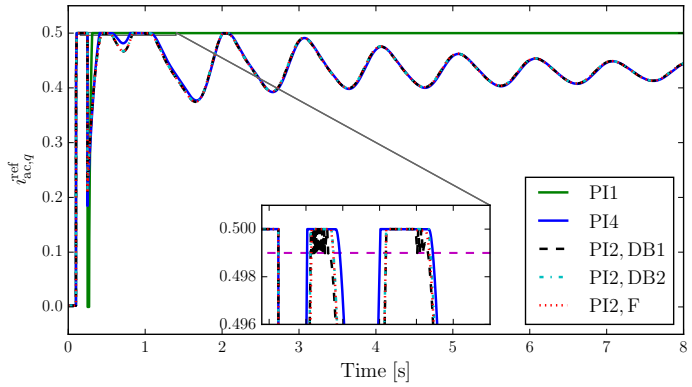

Figure 6.18: Scenario II: Response of maximum limit and output current reference of $\mathrm{PI}_{o,q}$ considering PI1, PI2 (DB1, DB2 and F) and PI4.

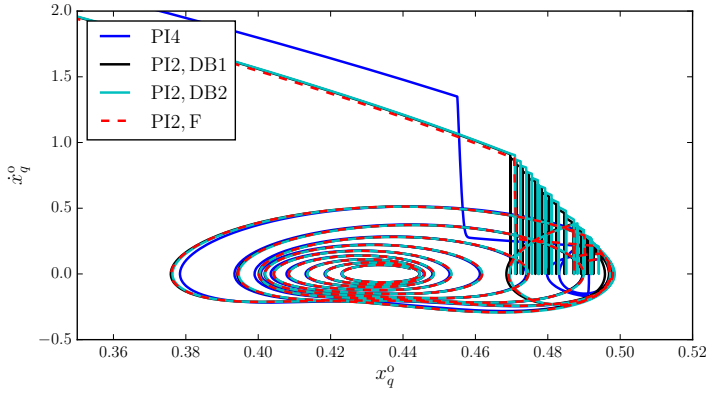

Figure 6.19: Scenario II: time derivative of the integrator state variable with respect to the state variable of $\mathrm{PI}_{o,q}$ in VSC1, considering PI4 and PI2 with DB1, DB2 and Filippov method.

reference reaches its limit (see Figure 6.18). While it stays at its limit, the rest of the current is available for d-axis current reference and this is why this current reference does not reach to zero. Comparing with Scenario I and II, it is evident that the current limits' choice plays a significant role in the dynamic response during a severe disturbance.

While using the PI2 model, numerical chattering is observed. Comparing DB1,

Table 6.3: Parameters of current limit logic of the STATCOM

Parameters	**Scenario I**	**Scenario II**
Priority	v_{ac}	v_{ac}
i_d^{lm}	0.05	0.05
i_q^{lm}	1.1	1.099
i_{max}	1.1	1.1

DB2 and Filippov based techniques, only DB1 based method results in chattering both in the output and the state variable (see zoom in Figure 6.18 and Figure 6.19). And the DB2 method does not show chattering on the output. Finally, Filippov-based approach does not lead any chattering illustrated in Figure 6.19.

6.4.2 Case Study II: STATCOM

This Section considers the Nordic system with a VSC-based STATCOM as discussed in Section 4.7. The d- and q-axis controllers of the outer level are set to control DC and AC voltage respectively. The STATCOM provides reactive power support, so the priority is set to q-axis current. Therefore, no switching of priority is needed. The contingency is a three-phase fault at bus 4044 occurring at $t = 1$ s and cleared by opening the line between bus 4044-4032 after 100 ms. The line is put back in service at $t = 6.1$ s. A deadband value 0.003 is used for DB1 and DB2 based PIs. Similar to the previous case study, two scenarios are studied and parameters of current limit logic are given in Table 6.3. Both scenarios are discussed below.

- **Scenario I:**

The trajectories of the q-axis current reference, maximum and minimum limits of the d-axis controller ($\text{PI}_{\text{o},d}$) i.e., the DC voltage controller and the DC voltage are

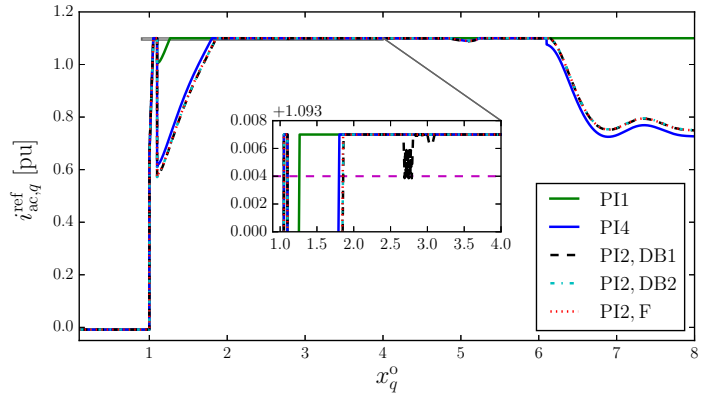

Figure 6.20: Scenario I: Response of the AC voltage controller, using model PI1, PI4 and PI2 with deadbands (DB1, DB2) and Filippov method (F).

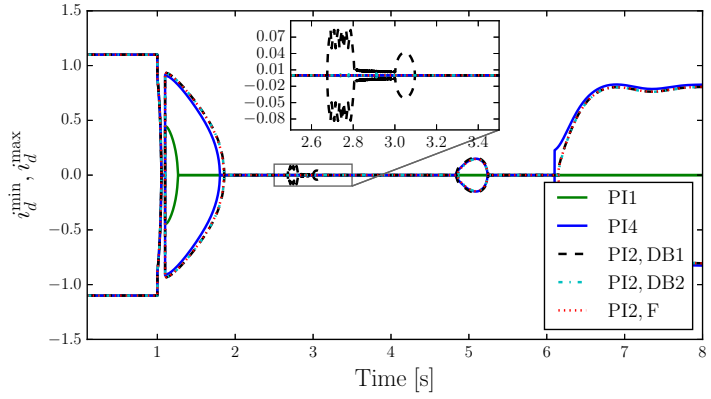

Figure 6.21: Scenario I: Response of the maximum and minimum limits of DC voltage controller, using model PI1, PI4 and PI2 with deadbands (DB1, DB2) and Filippov method (F).

shown in Figures 6.20, 6.21 and 6.22 respectively for the considered PIs. Following the contingency, the q-axis current reference reaches its maximum limit and the current limiter imposes zero on the limits of the d-axis controller (see Figure 6.21). Using the PI2 model, the q-axis current reference limit stays longer at its limit due to windup and during this time, the d-axis current reference is zero. It causes an increasing trend in the DC voltage response. Such a deviation of the v_{dc} from its pre-disturbance equilibrium results in the collapse of the system.

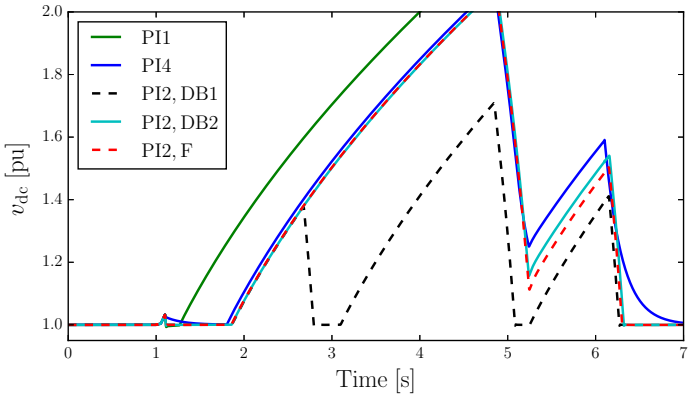

Figure 6.22: Scenario I: Response of the DC voltage, using model PI1, PI4 and PI2 with deadbands (DB1, DB2) and Filippov method (F).

For the AW methods, while $i_{ac,q}^{ref}$ stays at its limit, the PI2 model with DB1 and DB2 shows chattering, the PI4 and PI2 model with Filippov method show a smooth response. However, in this system chattering on the output ($i_{ac,q}^{ref}$) for the PI2 with DB1 causes a significant difference on the limits (see zoom in 6.21) of the d-axis controller compared to the other AW PIs. That is why a notable difference in the v_{dc} is observed with DB1. Scenario I shows that the same AW method depending on the implementations, can have a remarkable impact on the dynamic response. Finally, the advantage of Filippov-based method over DB1 and DB2 is shown in Figure 6.23.

- **Scenario II:**

This scenario considers a lower value for i_q^{lm} than the maximum current (see Table 6.3). The dynamic response of the q-axis current reference, maximum and minimum limits of the d-axis controller ($PI_{o,d}$) i.e., the DC voltage controller and the DC voltage are shown in Figures 6.24, 6.25 and 6.26 respectively for the considered PIs. In this scenario, the limits of the d-axis controller do not reach to zero and

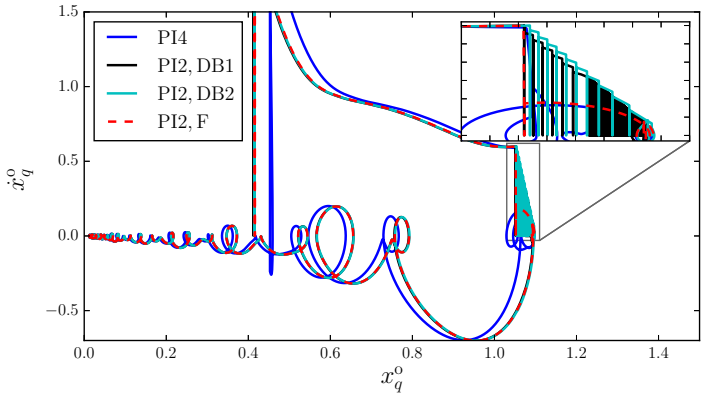

Figure 6.23: Scenario I: Time derivative of the integrator state variable with respect to the state variable of the AC voltage controller.

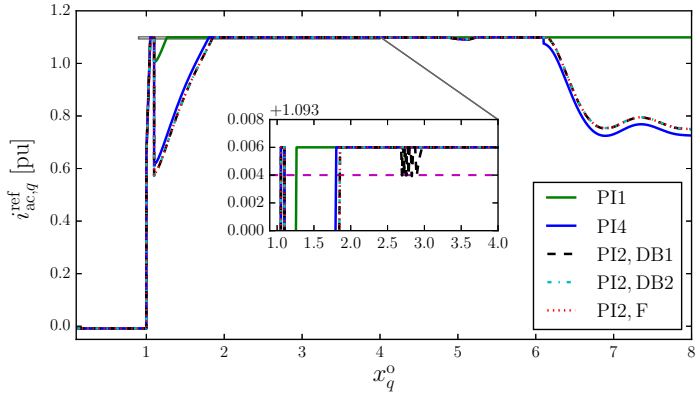

Figure 6.24: Scenario II: Response of the AC voltage controller, using model PI1, PI4 and PI2 with deadbands (DB1, DB2) and Filippov method (F).

that is why the v_{dc} response shows a drastically different response compare to the Scenario I. In addition, the delayed response of the PI1 models does not significantly impact the v_{dc} voltage trajectory (see Figure 6.26).

Comparing AW methods, PI4 and PI2 models show a little difference in the dynamic response. However, the PI2 model with DB1 chattering is observed in the output and thus in the limits. Filippov-based model results in a smoother response.

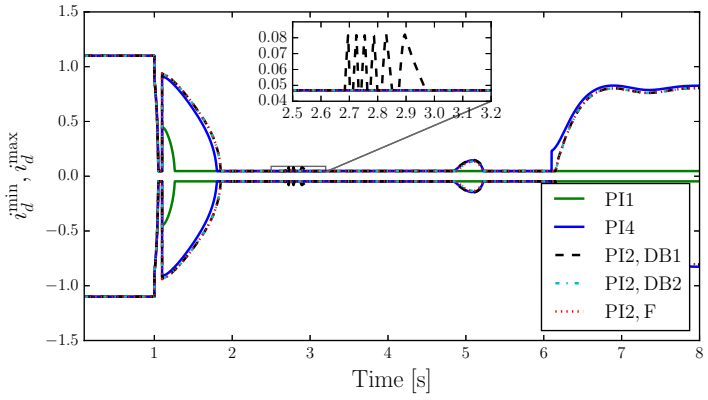

Figure 6.25: Scenario II: Response of the maximum and minimum limits of DC voltage controller, using model PI1, PI4 and PI2 with deadbands (DB1, DB2) and Filippov method (F).

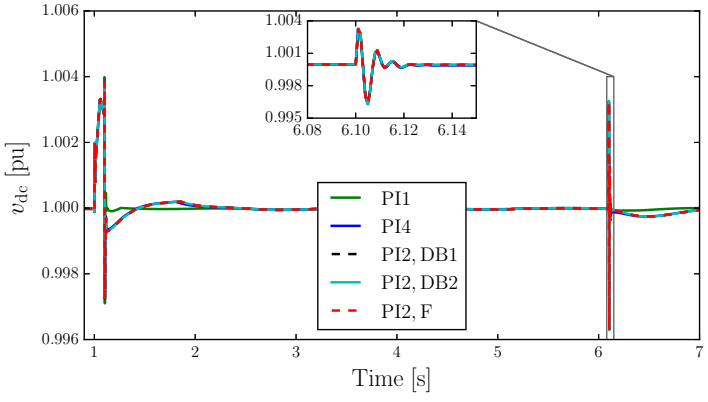

Figure 6.26: Scenario II: Response of the DC voltage, using model PI1, PI4 and PI2 with deadbands (DB1, DB2) and Filippov method (F).

6.5 Conclusions

This Chapter extends the IEEE Std. 421.5-2016 AW PI model, based on Filippov theory, to avoid the numerical issues intrinsic of these models and proposes a new deadband based implementation of the same AW configuration. Both models are validated, considering an illustrative example. Furthermore, this Chapter studies two different deployments of outer level configurations coupled with the current

limit block of VSCs. Those outer level schemes are studied considering three other PI implementations (windup, AW with back calculation and Std. techniques) with variable limits. For the Std. AW method deadband and Filippov based methods are discussed. It is shown that each configuration of upper level and limiting technique of PIs have a significant impact on numerical simulation and overall systems dynamic response through numerical simulations. Among the available implementation techniques for the IEEE Std. AW PI limiter, the proposed theoretical approach achieves the most accurate results.

7 Fractional Order PI Control Limiters

7.1 Introduction

In recent years, fractional calculus-based controllers have gained increasing attention in the power system community, mostly because of their robust performance for a wide range of operating conditions and parameter variations. Among other types of those controllers, the Fractional Order PI (FOPI) controller is an extension of the classical PI which stems from the theory of fractional calculus. Fractional calculus studies the differentiation and integration operations for non-integer (fractional) orders.

The potential of employing fractional calculus for the purpose of control was first shown in the definition of Bode's ideal transfer function [25], while the frequency domain properties of FO controllers were systematically exploited first in [84]. To date, the FO version of the PID (FOPID) [95], has been the most popular FO controller. The utilization of FO controllers in power systems has been recently proposed for different applications, including voltage [100,120], frequency [38,87,110] and damping [9, 29] control schemes. The implementation of these controllers is done by means of approximating the fractional dynamics with rational order transfer functions [115]. In this Chapter, fractional dynamics are approximated by the widely used Oustaloup's Recursive Approximation (ORA) method [85]. However, the effect of control saturation on the dynamic behavior of Fractional Order (FO) controllers

for power system applications has not been considered at all. This Chapter discusses modeling and simulation of windup and anti-windup limiters of the FO version of the classical PI controller (FOPI) for power systems.

Previous Chapters showed how control limits play a crucial role when large disturbances are of interest, as it happens, e.g. in dynamic security assessment. Regarding PI controllers, the integrator windup phenomenon is known to severely limit the control performance and classical AW methods on PI and their impact on dynamic systems response is addressed in previous Chapters. Similar techniques are also proposed for FOPIs [86, 88]. However, a systematic study of the impact and numerical issues of those classical methods on FOPIs for power system applications has not been given thus far. A discussion on the modeling of windup and AW limiters of FOPI controllers for power system applications is given in this Chapter. Then the impact of FOPI limiter models on power system dynamic response is shown considering a VSC-based STATCOM.

The remainder of the Chapter is organized as follows. Section 7.2 provides a background on the theory of fractional calculus for control applications. Section 7.3 presents the considered FOPI control models. The case study is discussed in Section Section 7.4, based on the IEEE 14-bus system. Conclusions are drawn in Section 7.5.

7.2 Theory of Fractional Order Control

Fractional calculus provides the extension of differentials and integrals for non-integer number orders. There exist different formulations of fractional calculus. The most important ones are arguably the Riemann–Liouville (R-L); the Grünwald

Letnikov (G-L); and the Caputo definition. Each definition may be more or less suitable depending on the application.

For the purpose of the design of fractional controllers, the Caputo definition is the most appropriate. Consider a function $\phi : [0, \infty) \to \mathbb{R}$. In its derivative form, Caputo definition for the fractional derivative ϕ of order $\gamma \in \mathbb{R}^+$ reads [79]:

$$\phi^{(\gamma)}(t) = \frac{1}{\Gamma(\mu - \gamma)} \int_0^t \frac{\phi^{(\mu)}(\tau)}{(t - \tau)^{\gamma - \mu + 1}} d\tau \ , \tag{7.1}$$

where γ, $\mu - 1 < \gamma < \mu$, $\mu \in \mathbb{N}$, denotes the fractional order; $\Gamma(\cdot)$ is the Gamma function; and $\phi^{(\gamma)}(t) = d^\gamma \phi / dt^\gamma$. Unlike the R-L and G-L definitions, the initial conditions of (7.1) are of integer order. This property is of great importance, since for physical variables, only integer order initial conditions are known.

7.2.1 Fractional Order PID Control Strategy

The most popular FO control strategy is the FOPID [94]. The FOPID controller is an extension of the classical PID, and is characterized by five parameters: three gains, namely proportional, integral, and derivative; and two fractional orders, namely integral and derivative.

Employing a FOPID extends the four control points of the PID strategy to the plane defined by the orders α and β [79]. This is illustrated in Figure 7.1.

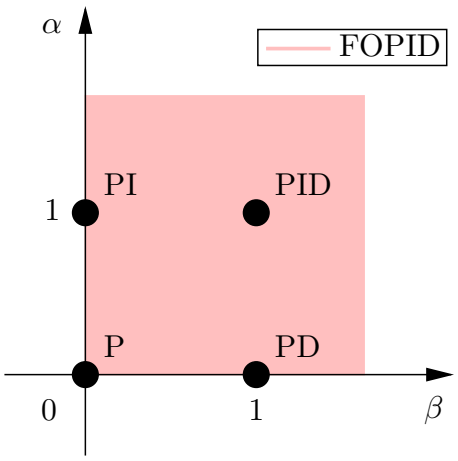

Figure 7.1: PID vs FOPID: From point to plane.

7.2.2 Approximation of Fractional Dynamics

Modeling of fractional dynamics is typically done by employing rational transfer functions that approximate the fractional derivatives and integrals. In this Chapter fractional dynamics are approximated by the commonly employed ORA technique. Let $[\omega_b, \omega_h]$ be the frequency range for which the approximation is designed and N the dynamic order of the approximation. Then, the ORA of s^γ is defined as follows [79]:

$$s^\gamma \approx \omega_h^\gamma \prod_{k=1}^{N} \frac{s+\omega_k'}{s+\omega_k} \ , \tag{7.2}$$

where

$$\begin{aligned} \omega_k' &= \omega_b \omega_v^{(2k-1-\gamma)/N} \ , \\ \omega_k &= \omega_b \omega_v^{(2k-1+\gamma)/N} \ , \\ \omega_v &= \sqrt{\omega_h/\omega_b} \ . \end{aligned} \tag{7.3}$$

The parameters in (7.3) are derived from a set of recursive equations [85]. The block diagram of the ORA is shown in Figure 7.2.

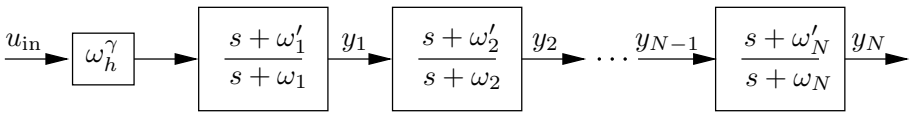

Figure 7.2: Oustaloup's Recursive Approximation (ORA).

The accuracy of (7.2) deteriorates if high fractional orders, i.e. $|\gamma| > 1$ are to be used. In this case, the implementation consists in the product of an integer order block and a fractional order block, as follows:

$$s^\gamma = s^n s^{\gamma-n}, \quad n \in \mathbb{Z}, \quad (\gamma - n) \in [0, 1] \ . \tag{7.4}$$

Figure 7.2 shows that each block of the ORA is a lead-lag filter. In time domain, the ORA dynamic model can be described by a set of differential-algebraic equations, as follows [18]:

$$\begin{aligned}
\chi_1' &= a_1\chi_1 + b_1\omega_h^\gamma u_{\text{in}} \ , \\
0 &= y_1 - \chi_1 - \omega_h^\gamma u_{\text{in}} \ , \\
\chi_2' &= a_2\chi_2 + b_2(\chi_1 + \omega_h^\gamma u_{\text{in}}) \ , \\
0 &= y_2 - \chi_2 - \chi_1 - \omega_h^\gamma u_{\text{in}} \ , \\
&\vdots \\
\chi_N' &= a_N\chi_N + b_N(\sum_{k=1}^{N-1} \chi_k + \omega_h^\gamma u_{\text{in}}) \ , \\
0 &= y_N - \sum_{k=1}^{N} \chi_k - \omega_h^\gamma u_{\text{in}} \ .
\end{aligned}$$

where $a_k = -\omega_k$, $b_k = \omega'_k - \omega_k$. Using matrix notation, one finally has:

$$\begin{aligned} \boldsymbol{\chi}' &= \boldsymbol{A}\boldsymbol{\chi} + \boldsymbol{B}u_{\text{in}} \ , \\ 0 &= y_N - \boldsymbol{C}\boldsymbol{\chi} - \omega_h^{\gamma} u_{\text{in}} \ , \end{aligned} \tag{7.5}$$

where $\boldsymbol{\chi} = [\chi_1 \ \ \chi_2 \cdots \ \chi_N]^T$; and

$$\boldsymbol{A} = \begin{bmatrix} a_1 & 0 & 0 & \cdots & 0 \\ b_2 & a_2 & 0 & \cdots & 0 \\ b_3 & b_3 & a_3 & \cdots & 0 \\ \vdots & \vdots & \vdots & \ddots & \vdots \\ b_N & b_N & \cdots & b_N & a_N \end{bmatrix} \ , \ \boldsymbol{B} = \begin{bmatrix} \omega_h^{\gamma} b_1 \\ \omega_h^{\gamma} b_2 \\ \omega_h^{\gamma} b_3 \\ \vdots \\ \omega_h^{\gamma} b_N \end{bmatrix} \ ,$$

$$\boldsymbol{C} = \begin{bmatrix} 1 & 1 & \cdots & 1 & 1 \end{bmatrix} \ .$$

$\boldsymbol{A}$, $\boldsymbol{B}$, $\boldsymbol{C}$, have dimensions $N \times N$, $N \times 1$ and $1 \times N$, respectively.

7.3 Fractional Order PI Schemes

This Section presents the FOPI schemes considered in this study. These include an unconstrained FOPI (FOPI0); a FOPI with windup limiter (FOPI1); a FOPI with a back calculation AW limiter (FOPI2); a FOPI with an automatic reset AW limiter (FOPI3); and a FOPI with a conditional AW model (FOPI4). The block diagrams of all five FOPI control schemes are shown in Figure 7.3.

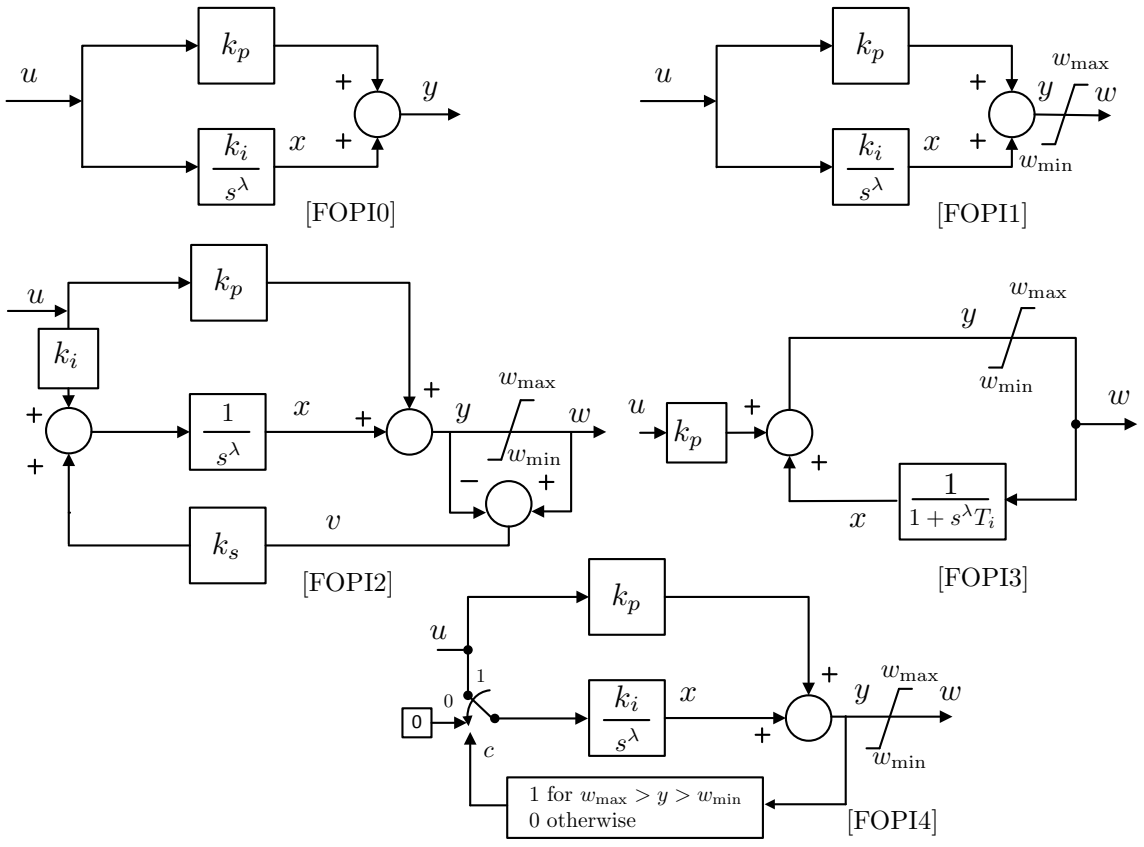

Figure 7.3: Examined FOPI controller models: (FOPI0) without limits; (FOPI1) with windup limiter; (FOPI2) with back calculation AW limiter; (FOPI3) with automatic reset AW limiter; (FOPI4) with conditional AW limiter.

It is relevant to note here is that there exist several other AW schemes that one may consider [16]. However, the considered models cover the most common configurations proposed for FOPI [86]. Observe that except for FOPI3 all other configurations are discussed in Chapter 4. That is why in following only FOPI3 is discussed.

- **Automatic reset (FOPI3):** This model considers a saturated input to the forward signal of the controller. Therefore, if the output exceeds its limit, a constrained input reduces the integral action which in turn prevents the windup.

The integral state variable is given:

$$x^{(\gamma)} = \frac{1}{T_i}(w - x) \ , \tag{7.6}$$

where $T_i = \dfrac{k_p}{k_i}$.

7.3.1 Numerical Issues of the Conditional AW model

The conditional AW technique is recommended by the IEEE Standard 421.5-2016 for power system dynamic studies [8]. Implementation difficulties as well as numerical issues that may occur during time domain simulations with inclusion of this model for the integer-order PI controller have been addressed in previous Chapters. However, the structure of an ORA-based FOPI controller is different from that of the integer-order PI, and thus, the two implementations do not show the same numerical issues. This Section discusses the numerical issue of the conditional AW model that occurs for ORA-based FOPI controllers.

Let us consider a time domain simulation with inclusion of a FOPI with conditional AW limiter. The FOPI input is arbitrary and no limit is binding until $t = t_1$, i.e. the controller is in its integrating region. At $t = t_1$, the control output reaches its maximum for a positive input value $u(t_1) > 0$. Then:

$$x(t_1) + k_p u(t_1) = w_{\max} \ . \tag{7.7}$$

For simplicity but without loss of generality, let us consider that the ORA order is

$N = 1$. Combining (7.5) and (7.7) yields:

$$\begin{aligned} w_{\max} &= \big(\boldsymbol{C}\chi_1(t_1) + \omega_h^{\gamma} u(t_1)\big) k_i + k_p u(t_1) \ , \\ \chi_1'(t_1) &= \boldsymbol{A}\chi_1(t_1) + \boldsymbol{B}u(t_1) \ . \end{aligned} \tag{7.8}$$

Let us consider the backward Euler integration method with step size h. Then, $\chi_1(t_1)$ is obtained as:

$$\begin{aligned} \chi_1(t_1) - \chi_1(t_1 - h) = h\chi_1'(t_1) &= h\big(\boldsymbol{A}\chi_1(t_1) + \boldsymbol{B}u(t_1)\big) \ , \\ \Rightarrow \chi_1(t_1) &= \frac{h\boldsymbol{B}u(t_1) + \chi_1(t_1 - h)}{1 - h\boldsymbol{A}} \ . \end{aligned} \tag{7.9}$$

The value of the output variable is $y(t_1) = w_{\max} > 0$, and thus $y(t_1)u(t_1) > 0$. Correspondingly, the control input switches to 0, according to conditional integration definition. Re-calculating $\chi_1(t_1)$ for the zero input $u(t_1) = 0$, one obtains:

$$\begin{aligned} \chi_1(t_1) - \chi_1(t_1 - h) = h\chi_1'(t_1) &= h\boldsymbol{A}\chi_1(t_1) \ , \\ \Rightarrow \chi_1(t_1) &= \frac{\chi_1(t_1 - h)}{1 - h\boldsymbol{A}} \ . \end{aligned} \tag{7.10}$$

Observe that $\chi_1(t_1 - h)$ is constant in (7.9) and (7.10), and that $\boldsymbol{A}, \boldsymbol{B}, h$ are positive. Hence the value of the integrator state variable decreases. This results in a decrease of the output below its maximum value so that (7.7) is not satisfied anymore. However, at the same time step, the controller starts integrating and the condition for switching back to maximum becomes true again. Finally, a chattering between the maximum and integrating region occurs at t_1 and the solver fails to converge. This chattering problem occurs even if a different implicit integration method is considered.

Note that the solver can be designed to continue the simulation by changing

the input only at the next time step. Nevertheless, this strategy also introduces numerical chattering until there is a sufficient decrease of the input and the solution reaches back to the integrating range.

7.4 Case Study

The case study considers a VSC-based STATCOM model and discusses the dynamic response of the examined FOPI control schemes. The converter and its inner control loop are shown in Figure 4.7. The outer control loop is shown in Figure 4.8 and configuration [I] is considered. All controllers in the outer and inner loops are FOPI controllers. The d and q components in the outer control loop are utilized to control the DC and AC voltages, respectively, while the inner loop controls the decoupled d and q currents.

7.4.1 Test System

The IEEE 14-bus system is considered to compare the FOPI models within the VSC control. This system comprises 14 buses, 5 synchronous generators, 11 loads, 12 transmission lines, 4 transformers and 1 shunt capacitor. All the generators are equipped with automatic voltage regulators, and the generators at buses 1 and 2 include turbine governors. The static and dynamic data of this system are given in [76].

A STATCOM is connected at bus 9 for AC voltage control. The data of the STATCOM are given in Table 7.1. Regarding the FOPIs ORA parameters, the frequency range is set to $[10^{-3}, 10^{2}]$ rad/s and the dynamic order is $N = 5$ for all

Table 7.1: STATCOM controller parameters

Name	**Values**
Converter	$r_{\text{ac}} = 0.001$ pu, $x_{\text{ac}} = 0.05$ pu
Current Limits	$i_{\text{ac},q}^{\text{lim}} = \pm 0.2$ pu, $i_{\text{ac},d}^{\text{lim}} = \pm 0.01$ pu
Outer Control	$k_p^{\text{o},q} = 1$, $k_p^{\text{o},d} = 20$, $k_i^{\text{o},q} = 37.5$, $k_i^{\text{o},d} = 45$,
	$\gamma^{\text{o},q} = 0.7$, $\gamma^{\text{o},d} = 0.7$, $v_{\text{ac}}^{\text{ref}} = 1.056$, $v_{\text{dc}}^{\text{ref}} = 1$
Inner Control	$k_p^{\text{i},q} = 0.16$, $k_p^{\text{i},d} = 0.16$, $k_i^{\text{i},q} = 0.2$, $k_i^{\text{i},d} = 0.2$,
	$\gamma^{\text{i},q} = 0.7$, $\gamma^{\text{i},d} = 0.7$

FOPIs. Interested readers are referred to [110] for a detail discussion on the selection of these parameters. Unless otherwise stated, the value $k_s = 50$ is used for the back calculation gain of FOPI2. All simulation results are obtained using DOME.

7.4.2 Contingency I

The performance of the STATCOM voltage regulation is evaluated by increasing the active and reactive power consumption at buses 3 and 9 by 20% at $t = 1$ s. The voltage response of bus 9 with and without the STATCOM is shown in Figure 7.4. The STATCOM provides a fast voltage control without any steady state error. Note that for this disturbance the limits are not binding for any controller in the outer and inner level. Therefore, all FOPIs (FOPI0-FOPI4) provide exactly the same dynamic response.

7.4.3 Contingency II

For the purpose of comparing the impact of all FOPIs on the system transient response, a severe contingency is considered here. The contingency is a three phase

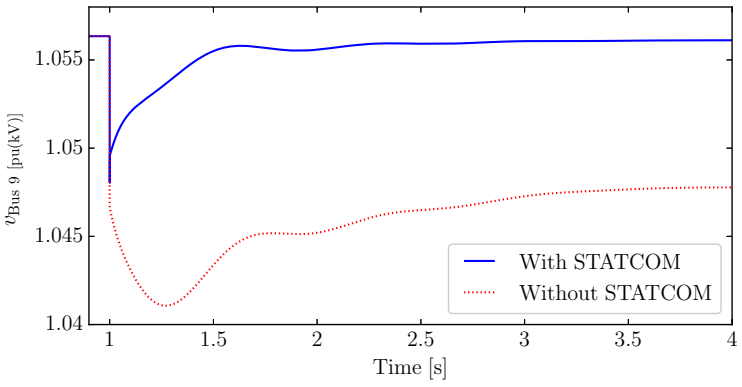

Figure 7.4: Response of the voltage at bus 9.

fault that occurs at bus 4 at $t = 1$ s. The fault is cleared after 100 ms through the tripping of the lines that connect buses 4-5 and 4-2. Both lines are back in service at $t = 4$ s. For this disturbance the limits of FOPI1-FOPI4 are activated in the AC voltage controller. Following the contingency, the response of the voltage at bus 9 for the controllers FOPI0-FOPI3 is shown in Figure 7.5. Observe that different FOPIs show significantly different transient response. Regarding FOPI4, the simulation with this model cannot be completed due to the numerical issues explained in Section 7.3.1. To further explain the differences in the voltage response, the fractional integrator state is shown in Figure 7.6 for FOPI0-FOPI3.

FOPI0 does not consider any limit and can provide the amount of reactive power that is needed to achieve the reference AC voltage setting. Therefore, the voltage sag during the fault is lower and after clearing the fault the voltage reaches to the pre-disturbance equilibrium. The unconstrained model, however, is not realistic for large disturbance analysis.

The models FOPI1-FOPI3 provide a similar response of the voltage until $t = 4$ s (see Figure 7.5), since the FOPIs output is always limited at the same value. In

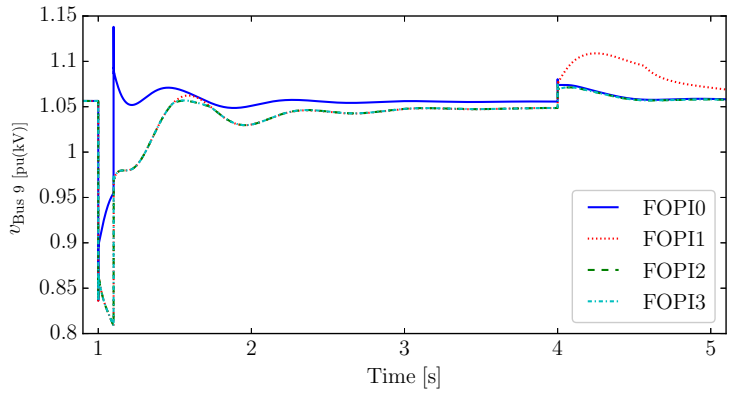

Figure 7.5: Response of the voltage at bus 9 considering FOPI0-FOPI3 for the distubance discussed in Section 7.4.3.

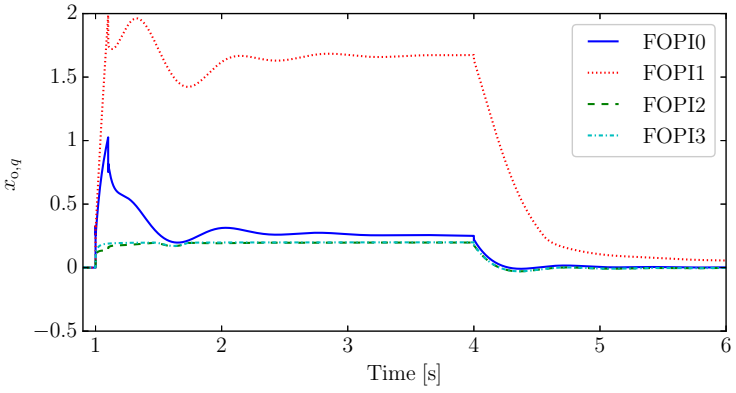

Figure 7.6: Response of the integrator state variable of AC voltage controller at outer level.

addition, for FOPI1-FOPI3, there exists a steady state error until $t = 4$ s and, hence, despite the similar voltage response during the first few seconds, FOPI1 does wind-up (see Figure 7.6). Therefore, this model shows a delayed response with a large overshoot when the system finally restores to the pre-disturbance condition at $t = 4$ s. On the other hand, the anti-windup techniques FOPI2-FOPI3 reduce the integrator's input when a limit is binding and thus do not allow the wind-up. This, in turn, provides an overall better transient response.

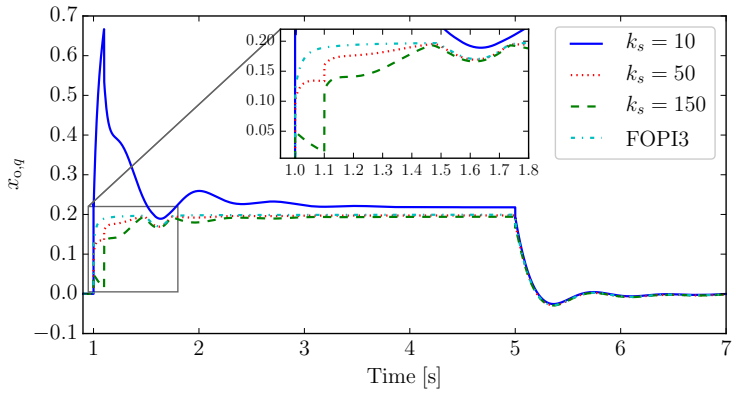

Figure 7.7: Response of the integrator state variable of AC voltage controller at outer level for: (i) FOPI2 with different k_s values; (ii) FOPI3.

7.4.4 Effect of Back Calculation Gain

The back calculation gain (k_s) in FOPI2 determines the speed and value at which the integrator state variable settles when a limit is binding. To show the impact of k_s, the 14-bus system is simulated by applying the same disturbance as in Section 7.4.3 for different values of k_s. In Figure 7.7, the trajectories of the FOPI2 integrator state variable as k_s varies are compared with the one of FOPI3. In order to obtain a faster wind-down of the integrator (see zoom in Figure 7.7), a relatively high value of k_s is required. On the other hand, FOPI3 always limits the integrator input at the saturation level and therefore does not provide any flexibility for a faster wind-down.

7.4.5 Contingency III

To show the dynamic response of FOPI4 when the solver continues through numerical chattering (see Section 7.3.1), the generator at bus 8 and the shunt device at bus 9 are disconnected at $t = 1$ s and re-connected at $t = 3$ s. Following the

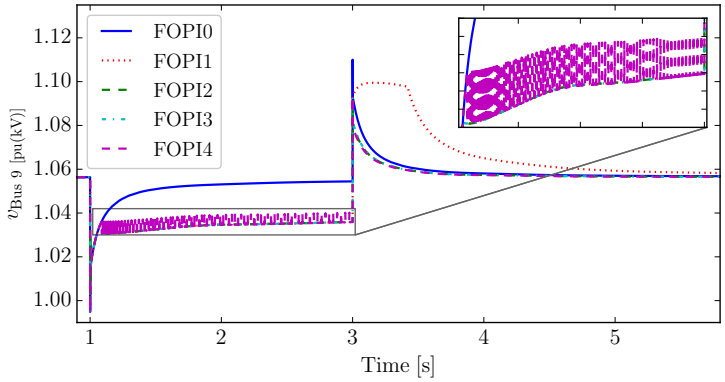

Figure 7.8: Response of the voltage at bus 9 considering FOPI0-FOPI3 for the distubance discussed in Section 7.4.5.

contingency the response of bus 9 voltage is shown in Figure 7.8 for all the FOPIs. For this disturbance the limits of the AC voltage controller binds in between $1-3$ s for FOPI1-FOPI4. Observe that, in the same time interval, using FOPI4 causes the voltage response to chatter (zoom in Figure 7.8) due to the numerical issues discussed in Section 7.3.1.

7.5 Conclusions

This Chapter presents the windup and anti-windup models of fractional-order PI controllers for a VSC-based STATCOM. The dynamic behaviors of these models are duly compared and discussed.

Simulation results indicate that, if a FOPI controller-based application is used in a power system software tool for dynamic analysis, the model should consider an appropriate AW method. Among the three most common AW methods, the back calculation (FOPI2) and the automatic reset method (FOPI3) are to be preferred compared to the conditional integrator method (FOPI4). Moreover, whenever the

FOPI2 is employed the back calculation gain has to be properly tuned for better dynamic response.

8 Conclusions and Future Works

8.1 Concluding Remarks

This thesis studies the electromechanical dynamics of power systems described by a set of DRHS DAEs. This set of DRHS DAEs is based on hybrid automata. In particular, ULTC and PI limiter type discontinuous models are discussed. The concluding remarks of this thesis are given below.

- Among several hybrid modeling frameworks, hybrid automata are the most effective implementations. Hybrid automata captures most types of continuous and discrete dynamics, which is the model used throughout this work.
- The dead-band and delay settings of ULTCs play a crucial role in the voltage restoration or collapse and number of tap operation.
- When considering stochastic processes, the time-domain analysis is necessary to account for ULTC tap variations as these cannot be rightly captured considering steady-state analysis.
- Implementation of the correct control logic of ULTCs requires special care to avoid unnecessary tap operation.
- Different implementations of PI control limiters result in significantly different transient responses of interconnected power systems. In large disturbance analysis, simulation results show that the anti-windup limiters are to be preferred, but

their implementation and design requires particular care, especially the IEEE Std. 421.5-2016 model, which shows numerical issues. A distinguish between modeling and solver issues of PI control limiters is given.

- Filippov theory is proposed to solve the deadlock problem of the IEEE Std. 421.5-2016 AW PI controller.
- This thesis proposes a generalized design of Filippov system models that identifies the conditions to automatically switch to different discontinuous vector fields.
- The case studies in Chapter 5 confirm the versatility of the proposed FT approach, which proves to be suitable for both event-driven (Dymola) and time-stepping (DOME) software tools.
- Dead-band and time delay based solution techniques are compared with the proposed Filippov based design. The proposed design provides the best and most accurate dynamic response of all the tested methods and is suitable for implementing in a power system software tool.
- The FT based AW PI model is extended to consider variable limits for VSC-based applications.
- A new dead-band based implementation of the Std. AW configuration is proposed to remove the chattering in the output.
- Different implementations (windup, AW with back-calculation and Std. techniques) with variable limits used in current limiters of VSCs are compared. Simulation results show that a combination of current limit along with the PIs in VSCs has a significant impact on numerical simulation and overall systems dynamic response. When the IEEE Std. 421.5-2016 model is considered the proposed FT based method provides the most accurate dynamic response.

- Finally, this thesis presents the windup and anti-windup models of fractional-order PI controllers. Simulation results indicate that, among the three most common AW methods, the back calculation and the automatic reset method are to be preferred compared to the conditional integrator method for fractional PI with AW limiters.

8.2 Future Work Directions

Possible future work directions of the work presented in this thesis are given below.

- The impact of PI controller limiters are studied in Chapter 4 considering two VSC-based applications, STATCOM and HVDC-link. This analysis can be further extended to study other applications for example, storage, wind generators, smart transformers and micro-grids.
- Filippov theory-based conditional anti-windup PI is rigorously studied and advantages of this method are shown by comparing the results with available solution techniques in Chapters 5 and 6. The comparison is performed based on a qualitative method. In future work, this comparison can be extended using a quantitative approach. The quantitative approach should provide a comparison from computational point of view for both event-driven and time-stepping based event handling methods.
- PI controllers are studied rigorously in this work as an example of a discontinuous model with discontinuity in state variable as well as in algebraic variable. Other types of application for example, lag, lead-lag models are relevant and can be

studied in future. This study can be further extended to consider variable limits on these models.

- The numerical issues of the conditional integration anti-windup method for FOPI controller with ORA approximation presented in Chapter 7 can be further investigated and a suitable solution can be proposed using Filippov theory.

- This thesis studies the numerical issues of discontinuous models, for example, the deadlock or chattering from a modeling point of view. It is also shown that these issues can be solved using a heuristic method (dead-band) or a theoretical approach (Filippov theory) by reimplementing the model. However, suppose similar issues are observed in a different model, for example, the conditional anti-windup on fractional-order PI controller discussed in chapter 7, one needs to go through the model again to propose a suitable solution. However, it can be possible to study the numerical issues from a solver point of view instead of a modeling point of view. In that case, the solver can be generalized in a way so that if the mathematical model has a specific issue, the solver will handle that accurately during the time-domain simulation. This future work direction is challenging due to the different nature of discontinuity in power systems models.

Bibliography

[1] Dymola: Dynamic Modeling Laboratory. [Online]. Available: `https://www.3ds.com/`.

[2] Generic Type-3 Wind Turbine Generator Model for Grid Studies. WECC Wind Generator Modeling Group, September, 2016.

[3] Great Britains' Transmission System Operator (National Grid). Live status, [Online]: `http://nationalgrid.stephenmorley.org/`.

[4] MATLAB. [Online]. Available: `https://www.mathworks.com/products/matlab.html`.

[5] OpenModelica. [Online]. Available: `https://www.openmodelica.org/`.

[6] Simscape Power Systems. [Online]. Available: `https://www.mathworks.com/products/simpower.html`.

[7] The Modelica Association. [Online]. Available: `https://modelica.org`.

[8] IEEE recommended practice for excitation system models for power system stability studies. *IEEE Std 421.5-2016 (Revision of IEEE Std 421.5-2005)*, pages 1–207, Aug 2016.

[9] Haseena Kuttomparambil Abdulkhader, Jeevamma Jacob, and Abraham T. Mathew. Robust type-2 fuzzy fractional order PID controller for dynamic stability enhancement of power system having res based microgrid penetration. *International Journal of Electrical Power & Energy Systems*, 110:357 – 371, 2019.

[10] Jyoti Agrawal, Kannan M Moudgalya, and Amiya K Pani. Sliding motion of discontinuous dynamical systems described by semi-implicit index one differential algebraic equations. *Chemical engineering science*, 61(14):4722–4731, 2006.

[11] Y. Amirnaser and Iravani Reza. *Voltage-sourced converters in power systems: modeling, control, and applications*. IEEE Press, 2012.

[12] G. K. Ari and Y. Baghzouz. Impact of high PV penetration on voltage regulation in electrical distribution systems. In *International Conference on Clean Electrical Power (ICCEP)*, pages 744–748, June 2011.

[13] Mohamed Asmine, Jacques Brochu, Jens Fortmann, Richard Gagnon, Yuriy Kazachkov, Charles-Eric Langlois, Christian Larose, Eduard Muljadi, Jason MacDowell, Pouyan Pourbeik, et al. Model validation for wind turbine generator models. *IEEE Transactions on power systems*, 26(3):1769–1782, 2010.

[14] K. J. Åström and Richard M Murray. *Feedback systems: an introduction for scientists and engineers*. Princeton university press, 2010.

[15] K. J. Åström and L. Rundqwist. Integrator windup and how to avoid it. In *1989 American Control Conference*, pages 1693–1698, June 1989.

[16] Karl J Åström and Tore Hägglund. *Advanced PID Control*. ISA - The Instrumentation, Systems and Automation Society, 2006.

[17] S. S. Baghsorkhi and I. A. Hiskens. Impact of wind power variability on subtransmission networks. In *IEEE PES General Meeting*, pages 1–7, July 2012.

[18] Jerzy Baranowski, Waldemar Bauer, Marta Zagórowska, Tomasz Dziwiński, and Paweł Piatek. Time-domain oustaloup approximation. In *2015 20th International Conference on Methods and Models in Automation and Robotics (MMAR)*, pages 116–120. IEEE, 2015.

[19] J. Beerten, S. Cole, and R. Belmans. Modeling of multi-terminal VSC HVDC systems with distributed DC voltage control. *IEEE Transactions on Power Systems*, 29(1):34–42, Jan 2014.

[20] K. R. W. Bell and A. N. D. Tleis. Test system requirements for modelling future power systems. In *IEEE PES General Meeting*, pages 1–8, July 2010.

[21] A. Bellen and M. Zennaro. *Numerical methods for delay differential equations*. Oxford Science Publications, Oxford, 2003.

[22] Bertil Berggren, Ritwik Majumder, and Nicklas Johansson. A generic vsc hvdc primary control structure suitable for stability studies. In *2013 EPRI HVDC & FACTS Conference*, pages 1–8, 2013.

[23] Martin Biák, Tomás Hanus, and Drahoslava Janovská. Some applications of filippovs dynamical systems. *Journal of Computational and Applied Mathematics*, 254:132–143, 2013.

[24] Martin Biák and Drahoslava Janovská. Differential algebraic equations of filippov type. *Application of Mathematics 2015*, pages 1–16, 2015.

[25] H. Bode. *Network Analysis and Feedback Amplifier Design*. Van Nostrand, 1945.

[26] M. S. Branicky, V. S. Borkar, and S. K. Mitter. A unified framework for hybrid control: model and optimal control theory. *IEEE Transactions on Automatic Control*, 43(1):31–45, Jan 1998.

[27] Milan S Calovic. Modeling and analysis of under-load tap-changing transformer control systems. *IEEE Transactions on Power Apparatus and Systems*, (7):1909–1915, 1984.

[28] François E Cellier and Ernesto Kofman. *Continuous system simulation*. Springer Science & Business Media, 2006.

[29] Lakhdar Chaib, Abdelghani Choucha, and Salem Arif. Optimal design and tuning of novel fractional order PID power system stabilizer using a new metaheuristic Bat algorithm. *Ain Shams Engineering Journal*, 8(2):113 – 125, 2017.

[30] Nilanjan Chaudhuri, Balarko Chaudhuri, Rajat Majumder, and Amirnaser Yazdani. *Multi-terminal direct-current grids: Modeling, analysis, and control*. John Wiley & Sons, 2014.

[31] S. Chiniforoosh, J. Jatskevich, A. Yazdani, V. Sood, V. Dinavahi, J. A. Martinez, and A. Ramirez. Definitions and applications of dynamic average models for analysis of power systems. *IEEE Transactions on Power Delivery*, 25(4):2655–2669, Oct 2010.

[32] A. C. H. Chow and B. P. Zeigler. Parallel devs: a parallel, hierarchical, modular modeling formalism. In *Proceedings of Winter Simulation Conference*, pages 716–722, 1994.

[33] Hantao Cui, Yichen Zhang, Federico Milano, and Fangxing Li. On the modeling and simulation of anti-windup proportional-integral controller. *arXiv preprint arXiv:2005.05430*, 2020.

[34] Lucian R. da Silva, Rodolfo C.C. Flesch, and Julio E. Normey-Rico. Analysis of anti-windup techniques in PID control of processes with measurement noise. *IFAC-PapersOnLine*, 51(4):948 – 953, 2018.

[35] Ujjwal Datta, Akhtar Kalam, and Juan Shi. Battery energy storage system to stabilize transient voltage and frequency and enhance power export capability. *IEEE Transactions on Power Systems*, 34(3):1845–1857, 2018.

[36] Ujjwal Datta, Akhtar Kalam, and Juan Shi. Battery energy storage system control for mitigating pv penetration impact on primary frequency control and state-of-charge recovery. *IEEE Transactions on Sustainable Energy*, 11(2):746–757, 2019.

[37] René David and Hassane Alla. Petri nets for modeling of dynamic systems: A survey. *Automatica*, 30(2):175–202, 1994.

[38] Sanjoy Debbarma, Lalit Chandra Saikia, and Nidul Sinha. Automatic generation control using two degree of freedom fractional order PID controller. *International Journal of Electrical Power & Energy Systems*, 58:120 – 129, 2014.

[39] T. Demiray. *Simulation of power system dynamics using dynamic phasor models*. PhD thesis, Dept. Inf. Technol. Elect. Eng., ETH Zurich, Zurich, 2008.

[40] L Dieci, C Elia, and L Lopez. On filippov solution of discontinuous DAEs of index 1.

[41] Luca Dieci and Luciano Lopez. A survey of numerical methods for IVPs of ODEs with discontinuous right-hand side. *Journal of Computational and Applied Mathematics*, 236(16):3967 – 3991, 2012.

[42] D. Dohnal. On-load tap-changers for power transformers. Technical report, Maschinenfabrik Reinhausen GmbH, Regensburg, Germany, September 2013.

[43] Vaibhav Donde and Ian A Hiskens. Analysis of tap-induced oscillations observed in an electrical distribution system. *IEEE Transactions on Power Systems*, 22(4):1881–1887, 2007.

[44] J. Egan, P. O'Rourke, R. Sellick, P. Tomlinson, B. Johnson, and S. Svensson. Overview of the 500 MW EirGrid East-West Interconnector, considering system design and execution-phase issues. In *Universities Power Engineering Conference (UPEC)*, pages 1–6, Sept 2013.

[45] Istvan Erlich, Jörg Kretschmann, Jens Fortmann, Stephan Mueller-Engelhardt, and Holger Wrede. Modeling of wind turbines based on doubly-fed induction generators for power system stability studies. *IEEE Transactions on power systems*, 22(3):909–919, 2007.

[46] Y. Susuki et al. A hybrid system approach to the analysis and design of power grid dynamic performance. *Proceedings of the IEEE*, 100(1):225–239, Jan 2012.

[47] Davide Fabozzi, Angela S Chieh, Patrick Panciatici, and Thierry Van Cutsem. On simplified handling of state events in time-domain simulation. *Proceedings of the 17th PSCC*, 2011.

[48] Davide Fabozzi, Stefan Weigel, Bernd Weise, and Fortunato Villella. Semi-implicit formulation of proportional-integral controller block with non-windup

limiter according to IEEE Standard 421.5-2016. In *Bulk Power Systems Dynamics and Control Symposium (IREP)*, pages 1–7, 2017.

[49] A. F. Filippov. *Differential Equations with Discontinuous Righthand Sides*. Kluwer Academic Publishers, 1988.

[50] G. K. Fourlas, K. J. Kyriakopoulos, and C. D. Vournas. Hybrid systems modeling for power systems. *IEEE Circuits and Systems Magazine*, 4(3):16–23, Third 2004.

[51] Arthur Charles Franklin and David Peter Franklin. *The J & P transformer book: a practical technology of the power transformer*. Elsevier, 2016.

[52] C Gardiner. Stochastic methods: a handbook for the natural and social sciences 4th ed.(2009).

[53] D. Giaouris, S. Banerjee, B. Zahawi, and V. Pickert. Stability analysis of the continuous-conduction-mode buck converter via Filippov's method. *IEEE Transactions on Circuits and Systems I: Regular Papers*, 55(4):1084–1096, May 2008.

[54] Adolf Hermann Glattfelder and Walter Schaufelberger. *Control systems with input and output constraints*. Springer Science & Business Media, 2012.

[55] Peter Harte, Elena Blokhina, Orla Feely, Daniele Fournier-Prunaret, and Dimitri Galayko. Electrostatic vibration energy harvesters with linear and nonlinear resonators. *International Journal of Bifurcation and Chaos*, 24(11):1430030, 2014.

[56] Nikos Hatziargyriou, Jovica Milanović, Claudia Rahmann, Venkataramana Ajjarapu, Claudio Cañizares, Istvan Erlich, David Hill, Ian Hiskens, Innocent Kamwa, Bikash Pal, et al. Stability definitions and characterization of dynamic behavior in systems with high penetration of power electronic interfaced technologies. 2020.

[57] I. A. Hiskens. Analysis tools for power systems-contending with nonlinearities. *Proceedings of the IEEE*, 83(11):1573–1587, Nov 1995.

[58] I. A. Hiskens. Power system modeling for inverse problems. *IEEE Transactions on Circuits and Systems I: Regular Papers*, 51(3):539–551, March 2004.

[59] I. A. Hiskens. Trajectory deadlock in power system models. In *IEEE International Symposium of Circuits and Systems (ISCAS)*, pages 2721–2724, May 2011.

[60] I. A. Hiskens. Dynamics of type-3 wind turbine generator models. *IEEE Transactions on Power Systems*, 27(1):465–474, Feb 2012.

[61] I. A. Hiskens and M. A. Pai. Hybrid systems view of power system modelling. In *2000 IEEE International Symposium on Circuits and Systems. Emerging Technologies for the 21st Century. Proceedings (IEEE Cat No.00CH36353)*, volume 2, pages 228–231 vol.2, 2000.

[62] I. A. Hiskens and M. A. Pai. Trajectory sensitivity analysis of hybrid systems. *IEEE Transactions on Circuits and Systems I: Fundamental Theory and Applications*, 47(2):204–220, Feb 2000.

[63] I. A. Hiskens and P. J. Sokolowski. Systematic modeling and symbolically assisted simulation of power systems. *IEEE Transactions on Power Systems*, 16(2):229–234, May 2001.

[64] IEEE PSDP Committee Power System Stability Subcommittee Test Systems for Voltage Stability and Security Assessment Task Force. Test systems for voltage stability analysis and security assessment. Technical report, Technical Report PES-TR19, 2015.

[65] M. Imhof and G. Andersson. Dynamic modeling of a VSC-HVDC converter. In *Universities Power Engineering Conference (UPEC)*, pages 1–6, Sept 2013.

[66] Thomas Kauffmann. *Modeling of wind parks for steady state short circuit studies.* PhD thesis, École Polytechnique de Montréal, 2018.

[67] Rick Wallace Kenyon, Matthew Bossart, Marija Marković, Kate Doubleday, Reiko Matsuda-Dunn, Stefania Mitova, Simon A Julien, Elaine T Hale, and Bri-Mathias Hodge. Stability and control of power systems with high penetrations of inverter-based resources: An accessible review of current knowledge and open questions. *Solar Energy*, 2020.

[68] Stefan Kowalewski, Mauro Garavello, Hervé Guéguen, Gerlind Herberich, Rom Langerak, Benedetto Piccoli, M Polderman, and Carsten Weise. Hybrid automata, 2009.

[69] Prabha Kundur. Power system stability and control. 1994.

[70] C. Long, A. T. Procopiou, L. F. Ochoa, G. Bryson, and D. Randles. Performance of OLTC-based control strategies for LV networks with photovoltaics. In *IEEE PES General Meeting*, pages 1–5, July 2015.

[71] Jan Lunze and Françoise Lamnabhi-Lagarrigue. *Handbook of hybrid systems control: theory, tools, applications.* Cambridge University Press, 2009.

[72] John Lygeros. Lecture notes on hybrid systems. In *Notes for an ENSIETA workshop*, 2004.

[73] Nancy Lynch, Roberto Segala, Frits Vaandrager, and Henri B Weinberg. Hybrid io automata. In *International Hybrid Systems Workshop*, pages 496–510. Springer, 1995.

[74] J. Mahseredjian, S. Dennetière, L. Dubé, B. Khodabakhchian, and L. Gérin-Lajoie. On a new approach for the simulation of transients in power systems. *Electric Power Systems Research*, 77(11):1514 – 1520, 2007.

[75] F. Milano. Semi-implicit formulation of differential-algebraic equations for transient stability analysis. *IEEE Transactions on Power Systems*, 31(6):4534–4543, Nov 2016.

[76] Federico Milano. *Power system modelling and scripting*. Springer Science & Business Media, 2010.

[77] Federico Milano. Hybrid control model of under load tap changers. *IEEE Transactions on Power Delivery*, 26(4):2837–2844, 2011.

[78] Federico Milano and Rafael Zárate-Miñano. A systematic method to model power systems as stochastic differential algebraic equations. *IEEE Transactions on Power Systems*, 28(4):4537–4544, 2013.

[79] Concepción A. Monje, YangQuan Chen, Blas M. Vinagre, Dingyü Xue, and Vicente Feliu. *Fractional-order Systems and Controls, Fundamentals and Applications*. Springer, 2010.

[80] T. Murata. Petri nets: Properties, analysis and applications. *Proceedings of the IEEE*, 77(4):541–580, Apr 1989.

[81] Conor Murphy and Andrew Keane. Local and remote estimations using fitted polynomials in distribution systems. *IEEE Transactions on Power Systems*, 32(4):3185–3194, 2017.

[82] Á. Ortega and F. Milano. Generalized model of VSC-based energy storage systems for transient stability analysis. *IEEE Transactions on Power Systems*, 31(5):3369–3380, Sept 2016.

[83] Á. Ortega and F. Milano. Modeling, simulation, and comparison of control techniques for energy storage systems. *IEEE Transactions on Power Systems*, 32(3):2445–2454, May 2017.

[84] A. Oustaloup. *La commande CRONE (commande robuste d'ordre non entier)*. Hermés, Paris, 1991.

[85] A. Oustaloup, F. Levron, B. Mathieu, and F. M. Nanot. Frequency-band complex noninteger differentiator: characterization and synthesis. *IEEE Transactions on Circuits and Systems I: Fundamental Theory and Applications*, 47(1):25–39, January 2000.

[86] Fabrizio Padula, Antonio Visioli, and Manuel Pagnoni. On the anti-windup schemes for fractional-order PID controllers. In *Proceedings of 2012 IEEE 17th International Conference on Emerging Technologies & Factory Automation (ETFA 2012)*, pages 1–4. IEEE, 2012.

[87] Indranil Pan and Saptarshi Das. Fractional-order load-frequency control of interconnected power systems using chaotic multi-objective optimization. *Applied Soft Computing*, 29:328 – 344, 2015.

[88] Sandeep Pandey, Prakash Dwivedi, and AS Junghare. A novel 2-DOF fractional-order PI$^{\lambda}$-D$^{\mu}$ controller with inherent anti-windup capability for a magnetic levitation system. *aeu-international journal of electronics and communications*, 79:158–171, 2017.

[89] Mario Paolone, Trevor Gaunt, Xavier Guillaud, Marco Liserre, Sakis Meliopoulos, Antonello Monti, Thierry Van Cutsem, Vijay Vittal, and Costas Vournas. Fundamentals of power systems modelling in the presence of converter-interfaced generation. *Electric Power Systems Research*, 189:106811, 2020.

[90] V. K. Paruchuri, A. Davari, and A. Feliachi. Hybrid modeling of power system using hybrid petri nets. In *Proceedings of the Thirty-Seventh Southeastern Symposium on System Theory, 2005. SSST '05.*, pages 221–224, March 2005.

[91] J. Peralta, H. Saad, S. Dennetière, J. Mahseredjian, and S. Nguefeu. Detailed and averaged models for a 401-level MMC-HVDC system. *IEEE Transactions on Power Delivery*, 27(3):1501–1508, July 2012.

[92] James L Peterson. Petri nets. *ACM Computing Surveys (CSUR)*, 9(3):223–252, 1977.

[93] Petri T. Piiroinen and Yuri A. Kuznetsov. An event-driven method to simulate Filippov systems with accurate computing of sliding motions. *ACM Trans. Math. Softw.*, 34(3):13:1–13:24, May 2008.

[94] I. Podlubny. *Fractional differential equations, volume 198: an introduction to fractional derivatives, fractional differential equations, to methods of their solution and some of their applications.* Academic Press, 1999.

[95] I. Podlubny. Fractional-order systems and $PI^{\lambda}D^{\mu}$-controllers. *IEEE Transactions Automatic Control*, 44(1):208–214, January 1999.

[96] D. Ranamuka, A. P. Agalgaonkar, and K. M. Muttaqi. Examining the interactions between DG units and voltage regulating devices for effective voltage control in distribution systems. *IEEE Transactions on Industry Applications*, 53(2):1485–1496, March 2017.

[97] Pranesh Rao, ML Crow, and Zhiping Yang. Statcom control for power system voltage control applications. *IEEE Transactions on power delivery*, 15(4):1311–1317, 2000.

[98] H. Saad, J. Mahseredjian, S. Dennetière, and S. Nguefeu. Interactions studies of HVDC-MMC link embedded in an AC grid. *Electric Power Systems Research*, 138:202 – 209, 2016.

[99] S. N. Salih, P. Chen, and O. Carlson. The effect of wind power integration on the frequency of tap changes of a substation transformer. *IEEE Transactions on Power Systems*, 28(4):4320–4327, Nov 2013.

[100] R. Shah, R. Preece, and M. Barnes. The impact of voltage regulation of multiinfeed VSC-HVDC on power system Stability. *IEEE Transactions on Energy Conversion*, 33(4):1614–1627, Dec 2018.

[101] Y. Susuki and T. Hikihara. Predicting voltage instability of power system via hybrid system reachability analysis. In *2007 American Control Conference*, pages 4166–4171, July 2007.

[102] Y. Susuki, T. J. Koo, H. Ebina, T. Yamazaki, T. Ochi, T. Uemura, and T. Hikihara. A hybrid system approach to the analysis and design of power grid dynamic performance. *Proceedings of the IEEE*, 100(1):225–239, Jan 2012.

[103] Y. Susuki, Y. Takatsuji, and T. Hikihara. Hybrid dynamical system as model for cascading outage in a power system. In *2008 40th North American Power Symposium*, pages 1–6, Sept 2008.

[104] Yu Takatsuji, Yoshihiko Susuki, and Takashi Hikihara. Hybrid controller for safe microgrid operation. *Nonlinear Theory and Its Applications, IEICE*, 2(3):347–362, 2011.

[105] S. Tarbouriech and M. Turner. Anti-windup design: an overview of some recent advances and open problems. *IET Control Theory Applications*, 3(1):1–19, January 2009.

[106] Lucio Tavernini. Differential automata and their discrete simulators. *Nonlinear Analysis: Theory, Methods & Applications*, 11(6):665–683, 1987.

[107] Lucio Tavernini. *Continuous-time modeling and simulation*, volume 2. CRC Press, 1996.

[108] M. Tharayil and A. Alleyne. A generalized PID error governing scheme for SMART/SBLI control. In *Proceedings of the 2002 American Control Conference*, volume 1, pages 346–351 vol.1, May 2002.

[109] Ange-Lionel Toba, Mamadou Seck, Matthew Amissah, and Sarah Bouazzaoui. An approach for devs based modeling of electrical power systems. In *2017 Winter Simulation Conference (WSC)*, pages 977–988. IEEE, 2017.

[110] G. Tzounas, I. Dassios, M. A. A. Murad, and F. Milano. Theory and implementation of fractional order controllers for power system applications. *IEEE Transactions on Power Systems*, pages 1–1, 2020.

[111] Fabian M Uriarte. *Multicore Simulation of Power System Transients*. Number 67. IET, 2013.

[112] Thierry Van Cutsem and Costas Vournas. *Voltage stability of electric power systems*. Springer Science & Business Media, 2007.

[113] A. A. van der Meer, M. Gibescu, M. A. M. M. van der Meijden, W. L. Kling, and J. A. Ferreira. Advanced hybrid transient stability and EMT simulation for VSC-HVDC systems. *IEEE Transactions on Power Delivery*, 30(3):1057–1066, June 2015.

[114] Arjan J Van Der Schaft and Johannes Maria Schumacher. *An introduction to hybrid dynamical systems*, volume 251. Springer London, 2000.

[115] B. M. Vinagre, I. Podlubny, and V. Feliu. Some approximations of fractional order operators used in control theory and applications. *Fractional calculus and applied analysis*, pages 231–248, January 2000.

[116] A. Visioli. Modified anti-windup scheme for PID controllers. *IEE Proceedings - Control Theory and Applications*, 150(1):49–54, Jan 2003.

[117] Bernd Weise. Impact of k-factor and active current reduction during fault-ride-through of generating units connected via voltage-sourced converters on power system stability. *IET Renewable Power Generation*, 9(1):25–36, 2015.

[118] Hans Witsenhausen. A class of hybrid-state continuous-time dynamic systems. *IEEE Transactions on Automatic Control*, 11(2):161–167, 1966.

[119] Q. Wu, D. H. Popovic, D. J. Hill, and M. Larsson. Tap changing dynamic models for power system voltage behaviour analysis. In *Power Systems Computation Conference (PSCC)*, 1999.

[120] Majid Zamani, Masoud Karimi-Ghartemani, Nasser Sadati, and Mostafa Parniani. Design of a fractional order PID controller for an AVR using particle swarm optimization. *Control Engineering Practice*, 17(12):1380 – 1387, 2009.

[121] Rafael Zárate-Miñano, Francesca Madia Mele, and Federico Milano. SDE-based wind speed models with Weibull distribution and exponential autocorrelation. In *IEEE PES General Meeting*, pages 1–5. IEEE, 2016.

[122] Bernard P Zeigler, Alexandre Muzy, and Ernesto Kofman. *Theory of modeling and simulation: discrete event & iterative system computational foundations*. Academic press, 2018.